UNIVERSITY OF CALIFORNIA
RIVERSIDE

From Pixels to Cosmology: An End-to-End Analysis of Galaxy Clusters and their Properties

A Dissertation submitted in partial satisfaction
of the requirements for the degree of

Doctor of Philosophy

in

Physics

by

Amanda Pagul

December 2022

Dissertation Committee:

Dr. Bahram Mobasher, Chairperson
Dr. George Becker
Dr. Gabriela Canalizo

The Dissertation of Amanda Pagul is approved:

Committee Chairperson

University of California, Riverside

Acknowledgments

Successfully completing a Ph.D. is a long and arduous process, a marathon. And it takes a village; it takes support which comes in various different forms–whether that be academic, emotional, spiritual, etc. I am eternally grateful for the support that I have received from my friends, my family, my colleagues–in other words, I am eternally grateful for the community around me.

I would first like to thank my advisor, Professor Bahram Mobasher. Before entering graduate school, I started out as an intern at UC Riverside and I am so thankful that Professor Mobasher took a chance on hiring me, starting my graduate journey. I am grateful for his wisdom in choosing a project, that although very challenging, would help me build an invaluable skillset and that would set me up for future success. I am grateful for the independence that he allowed me to have, to explore my own interests while he gently steered me in a direction that made this thesis more cohesive. I am grateful for his support and for standing up for me in moments when I did not feel comfortable standing up for myself. Thank you, Professor Mobasher.

I would also like to thank the committee members and the astronomy faculty and staff at UC Riverside. Thank you to George Becker for your emphasizing the value of having a fundamental theoretical background, and for all of your help with my qualifying exam and final thesis defense. Thank you to Professor Laura Sales, for being a great professor and always being somebody I felt I could talk to about everything from science, to outreach, to just "how's it going". I am excited to continue our diverse array of projects. Thank you to Professor Gabriela Canalizo, to teaching us both the fundamentals *and* the practical aspects

of perhaps the most fundamental part of being an astronomer, observational techniques. Beyond this, thank for being an advocate for us, the students, and for standing up against injustice. Thank you for all your advice and for your mentorship.

Special shoutout also to Benny, who made my mornings so much fun despite my long commute from Irvine; who always opened the office door for me when I inevitably forgot my key; and whose conversations always left me feeling refreshed.

Thank you to the DeepSkies collaboration. The friendships I've made there really got me through the graduate funk. I feel incredibly lucky to be part of this collaboration and to know such a thoughtful and caring group of people. Thank you for making the effort in making sure we all feel heard and for your philosophy of if people are treated well, the good work will come. It has been incredibly refreshing to be part of this awesome collaboration. Special shout-out to Brian, Aleksandra, and Ana.

Thank you to the former Yerkes Observatory, Geneva Lake Astrophysics and STEAM (GLAS), and the Stone Edge Observatory (SEO) teams for forever instilling in me to explore the wonders and curiosity of our universe. I always joke that growing up in New York City, the closest thing I've seen to a star is a helicopter, and Yerkes was really the place where my wonder and awe for astronomy developed. Thank you especially to Angela Olinto for pushing me to pursue astronomy/astrophysics; to Vivian Hoette for believing in me and entrusting me with various Yerkes projects that really kickstarted this journey; to Rich Kron for introducing me to astronomy research, for trusting me with the keys to the observatory, and for really balancing the astronomy experience with both fundamental *and* hands-on learning; and to Al Harper for all of the support, the fun and educational

observing nights, for instilling in me an appreciation for understanding the quirks of data at the most fundamental level. I look up to all of you and hope that one day I can be as great a scientist as you are.

Thank you to Katya, Adam, and Sarah for all of the work-study sessions, game nights, and always being there for me. Thank you to the folks at the University of Nigeria and NASDRA for your support, and for being great colleagues and friends. Thank you to Mac McQuown for providing the opportunity to work on the Stone Edge Observatory and for supporting our educational missions–it is an enormous privilege to work with SEO. A huge thank you to Kate Meredith for being one of the most genuine and unwavering people I know. I am continuously so impressed by the work that you do, your advocacy for your employees, colleagues, and friends, and for the amazing organization that you have built from the ground up. Most importantly, thank you for being a truly amazing friend to us, and for just being awesome.

The friendships that I had and the ones I made along the way kept me feeling fulfilled, even when things were tough. I'm so grateful for the friendships that I was fortunate to make at UC Riverside. Thank you to Najmeh and Marziye for your friendship and for all of the support, fun conversations, laughs, and good times that we've had. Thank you to my best friends from outside of UC Riverside, who would always have my back, cheer me up, and listen to me complain even when they had no idea what I was talking about. I'm so grateful for Paula, Farah, Lea, Jane, Haider, Maverick, and Wendy. I love you all.

Thank you to all my colleagues and friends who haven't explicitly been mentioned here, but who have shaped me and my graduate career into what it is today.

Thank you to my family, for all of their love and support, and for always being there for me. I am so grateful, especially, for my sister, Ginata Pagul. Thank you for being my best friend, for supporting me, for not getting *too* annoyed when I say Giinnaaaaatttaaaaaaaa and you know what's coming, and for somehow always finding the right things to say. I love you so much and I am so incredibly lucky that you are my sister.

And finally, there's not enough words in this world to express the gratitude and love I have for my husband, Javi Sánchez. Thank you thank you thank you for being my rock, for being my biggest supporter, for sticking by me through all of the hard times, and for making the great times even more beautiful and even more special. You have made this arduous process, this marathon, feel less hard. You have seen me at my lowest, but somehow always make the hardest moments feel easier. Thank you for always bringing joy and love into my life. Thank you for being my partner-in-crime, my pincitas, my sunshine, my bestest friend, my everything. I love you.

Publication acknowledgement:

The work in chapter 2 has been published in the Astrophysical Journal Supplements in 2021 (The Astrophysical Journal Supplement Series, Volume 256, Issue 2, id.27, 20 pp.).

To my family for all the sacrifices they've made and support they've given to make life better for us.

A mi familia por todos los sacrificios que han hecho y el apoyo que han brindado para mejorar nuestra vida.

Моей семье за поддержку и помощь которую они оказали, сделав нашу жизнь лучше.

ABSTRACT OF THE DISSERTATION

From Pixels to Cosmology: An End-to-End Analysis of Galaxy Clusters and their Properties

by

Amanda Pagul

Doctor of Philosophy, Graduate Program in Physics
University of California, Riverside, December 2022
Dr. Bahram Mobasher, Chairperson

This work is centered around two themes: (1) a focus on establishing a robust pipeline for deep HST image-to-catalog data reduction; and (2) using the generated catalog data to bridge themes in cosmology and astrophysics to understand and connect these two scales. I have developed a pipeline to efficiently create catalogs of deep and crowded, space-based data for the Hubble Frontier Fields and BUFFALO. These catalogs included source detection and extraction, intracluster light+bright cluster galaxy modeling, and multi-waveband homogenization.

Using these datasets, I have worked on two projects which aim to answer questions about large scale structure and galaxy formation and evolution. Within the BUFFALO collaboration, I am working on using the catalogs and our data products to understand how galaxies cluster in the very early universe (redshift > 5). Furthermore, my data products include models of the intracluster light (ICL) and I am using these to probe the underlying dark matter distribution in clusters and examine if we can use these observables to constrain dark matter modeling at these scales. By studying the correlations between ICL maps and

the best self-reported lens maps, we may be able to use the ICL maps as a prior to inform the construction of new, more reliable, lens maps.

Finally, I am also particularly interested in combining different data in interesting ways to understand the connection between properties at large and small scales, specifically as it relates to the relationship between light and dark matter. Combining multi-resolution ground- and space-based data with various techniques will become key to maximize the performance and synergies between current and upcoming surveys from JWST, Roman, Rubin, and Euclid.

Contents

List of Figures **xiii**

List of Tables **xviii**

1 Introduction **1**

2 Hubble Frontier Field Clusters and their Parallel Fields: Photometric and Photometric Redshift Catalogs **4**
2.1 The Data . . . 8
2.1.1 HST observations . . . 8
2.1.2 Ancillary data . . . 11
2.1.3 Modeling the point spread function in different bands . . . 14
2.1.4 Modeling the intra-cluster light . . . 16
2.1.5 Removal of the Bright Galaxies in Clusters . . . 21
2.2 Source extraction . . . 24
2.2.1 HST detections . . . 24
2.2.2 Photometry in lower resolution images . . . 26
2.3 Validation of the photometric catalog . . . 29
2.3.1 Quality and completeness via simulations . . . 29
2.3.2 Photometric uncertainties . . . 31
2.3.3 Comparison with previous work . . . 35
2.4 Photometric redshifts . . . 36
2.5 De-magnification . . . 40
2.6 Data Products . . . 41
2.7 Error correction . . . 42
2.8 Conclusions . . . 42

3 Photometric catalogs of the BUFFALO *HST* survey and overlapping Spitzer and K-band imaging **54**
3.1 Introduction . . . 55
3.2 The data . . . 57
3.2.1 *HST* observations . . . 58

3.2.2 Ancillary data . . . 59
3.3 Data processing . . . 60
3.3.1 Point Spread Function . . . 62
3.3.2 Modeling the intra-cluster light . . . 63
3.3.3 Modeling the brightest galaxies . . . 64
3.3.4 Source Extraction . . . 66
3.3.5 Photometry in Ancillary images . . . 67
3.4 Photometric validation . . . 68
3.5 Data products and results . . . 71
3.5.1 Photometric redshifts . . . 74
3.6 Comparison with the Hubble Frontier Fields . . . 76
3.7 Summary . . . 78

4 First measurement of the 2-point correlation function of galaxies at $z > 6$ in BUFFALO cluster Abell 370 80
4.1 Introduction . . . 80
4.2 Data and sample selection . . . 82
4.2.1 Photometry . . . 83
4.2.2 High-redshift sample selection . . . 84
4.3 Theory . . . 84
4.3.1 Deflection Corrections . . . 86
4.3.2 Magnification bias . . . 87
4.3.3 Covariance . . . 89
4.4 Galaxy correlation results . . . 90
4.4.1 Parallel field . . . 91
4.4.2 Cluster field . . . 92
4.4.3 Systematics . . . 93
4.5 Summary and Future Work . . . 93

5 Ongoing and Future Work 96
5.1 Intra-cluster light as a tracer of dark matter . . . 96
5.1.1 Introduction . . . 96
5.1.2 Comparing intra-cluster light maps with lensing κ maps . . . 97
5.1.3 Future work . . . 99
5.2 Combining space- and ground-based data with the Hubble Frontier Fields and the Dark Energy Survey . . . 100
5.2.1 Introduction . . . 100
5.2.2 Results . . . 101
5.2.3 Future Work . . . 102
5.3 Preparing for the James Webb Space Telescope . . . 103
5.3.1 Introduction . . . 103
5.3.2 Preliminary morphology tests . . . 103
5.3.3 Future work . . . 105

6 Conclusions 106

List of Figures

2.1 Workflow of the data processing as performed in the present work. 8

2.2 Throughput of the nine HST filters (*upper panel*) and ancillary Ks-band and IRAC bands (*lower panel*) used in this analysis. 12

2.3 Representative examples of PSF for the instruments used in this study, corresponding to a 0.06"/pixel scale normalized with the `ZScale` algorithm. From left to right, panels show F336W (WFC3), F606W (ACS), F125W (WFC3), K_s (VLT), IRAC Channel 1 (*Spitzer*). See Section 2.1.3 for more details . . 16

2.4 We illustrate the steps to generate the ICL map (as described in Section 2.1.4). Here the example is presented for the F160 band in Abell 2744. **Top Row:** *Left panel:* the "coverage map" showing the number of fit cutouts that overlap with each pixel. *Middle panel:* the resulting ICL map for the same band and cluster created by combining the fit background value of each cutout. Overlapping stamps are stacked using Eq. 3.1. *Right panel:* Final ICL map after smoothing the map in the Middle panel with a representative Gaussian kernel. More details about kernel creation as provided in section 2.1.4. **Bottom Row:** *Left panel:* Original Abell 2744 F160W science image. *Right panel:* F160W image after smoothed ICL (top row, right panel) subtraction. 18

2.5 Pixel values of the original background (blue histogram) and after ICL subtraction (orange histogram); the vertical dashed line marks the zero value. . 19

2.6 Growth curves for each HST-derived PSF normalized by the F160W growth curve before (top) and after (bottom) homogenization. 23

2.7 A summary of the various steps in bright cluster + ICL modelling (in this case for cluster Abell 2744). Upper panels show the original image (left) and the galaxy/ICL models (right). Lower panels show the residual image before and after median filtering (left- and right-hand panel respectively). The colorbar denotes the pixel intensity in counts/s. See Sections from 2.1.4 to 2.1.5 for more details. 44

2.8 Magnitude distributions for the objects detected using the cold (blue) and hot (orange) modes for the original image v. ICL+BCG subtracted image (top) and ICL+bcg subtracted image (bottom); matched (black) refers to total number of galaxies detected and kept in the catalog per magnitude bin. We see a significant increase in the number of detected galaxies in the cluster subtracted image, as well as a slight shift in mean magnitude toward fainter objects. 45
2.9 Comparison of magnitude distributions for the HFF cluster and their parallel fields. This clearly shows the excess in number of galaxies in clusters compared to the field. It also shows the field and cluster samples have similar depths. 46
2.10 Ratio between magnitude distributions in the parallel and cluster fields for all HFF clusters in the F160W band (top) and F814W band (bottom). The excess of field galaxies over clusters in fainter magnitude bins is likely caused by non-detection of faint sources in clusters due to diffuse light from more luminous objects. 46
2.11 (Left to right) Original IRAC Channel 1 image in Abell 2744 (*left panel*) compared to the residual map (*right panel*) after subtracting `T-PHOT` galaxy models (see Section 2.2.2). 47
2.12 Completeness as a function of magnitude for injected point-like sources between 24 and 30 mag in the six analyzed clusters (*top row*: Abell 2744, Abell 370, Abell S1063; *bottom row*: MACS1149, MACS0717, MACS0416). The positions of these objects were randomly assigned within the footprint (open circles – flavor 1, i.e., not blended) or randomly assigned in empty parts of the segmentation map (crosses – flavor 2). We introduce a small horizontal offset of the different markers and only include the error-bars for the flavor 2 case in order to improve readability. We also add horizontal solid line to mark 100% completeness, and two dashed lines at 80% and 60% completeness as visual help. Detections are made in IR-weighted images. 47
2.13 Photometric residuals between the simulated objects injected in the Abell 2744 cluster and the input fluxes, plotted as a function of magnitude for different bands. In each panel, blue small dots are the individual objects residuals, while the red dots represent the median in bins with 1.6 mag width. The shaded region encompasses the rescaled interquartile range, $0.7413(Q3-Q1)$ as a robust estimator of 1σ uncertainty [69]. The magnitude distribution of each injected sample is projected on the x axis on the top of the corresponding panel, while the photometric residual distribution is shown in the right-hand side of the y axis. 48
2.14 Photometric residuals in ancillary data ($K_{\rm s}$ band and *Spitzer*/IRAC channels). See the caption of Figure 2.13 for more details. We find a photometric bias between input and measured magnitude that we correct using the median value of the residual in each band. 49

2.15 Ratio between the flux uncertainty recovered via forward-modeling and the reported flux uncertainty by Source Extractor in three different bands: F160W (open circles), Ks (×), and IRAC Channel 1 (open triangles). For each band, a solid line shows the corresponding best-fit model, i.e. the power law $r_{\rm corr}(F) = aF^b$. The best-fit values found for a and b in the different bands can be found in Table 2.3.2. 49
2.16 Δmag = $\rm mag_{output} - mag_{input}$ for the F160W band as a function of the position of detected injected objects for the Abell 2744 cluster. There is no clear correlation between the residual and the position of the injected object in the field. Similar results are observed for the rest of the bands analyzed. 50
2.17 Comparison of our extracted photometry with that of the existing data produced by the ASTRODEEP and DEEPSPACE teams. Shown are the Δmag where data exists for cluster-only photometry in each band. The black dashed lines represent magnitude offsets of ± 0.05. The solid lines represent the running median and the shaded region represents the interquartile range of those measurements. 51
2.18 Assessing the quality of photometric redshifts estimated through SED fitting. *Upper panel:* $z_{\rm phot}$ vs. $z_{\rm spec}$ comparison. Red dots are 1,423 spectroscopic redshifts with $16 < F160W < 26$, the solid line shows the 1:1 relationship, and the dashed lines encloses the $z_{\rm phot} = z_{\rm spec} \pm 0.15(1 + z_{\rm spec})$ threshold used to identify outliers (i.e., catastrophic errors). NMAD scatter (σ) and outlier fraction (η) are reported on the top-left corner. *Lower panel:* $\Delta z \equiv z_{\rm phot} - z_{\rm spec}$ scatter (red dots are spectrosopic objects) with the median bias indicated by a solid line; dashed lines represent the threshold for catastrophic errors as in the upper panel. See Figure 2.19 for detailed performance in each individual cluster. 52
2.19 Comparison between $z_{\rm phot}$ and $z_{\rm spec}$ using the most reliable spectroscopic redshift (quality flag equal to 4). 53
2.20 Histogram of the photometric redshift distributions for individual clusters. The black dashed line corresponds to the redshift of the cluster. Objects selected have SED fits with a reduced $\chi^2 < 10$ 53

3.1 BUFFALO cluster footprints analyzed in this work. Color images created using `trilogy` [34], using F160W as the red channel, F105W as the green channel, and F814W as the blue channel. Note that due to the larger area coverage of F814W (ACS) compared to other bands (WFC3), certain areas of the footprint appear as blue. In the top left panel, we include the NIRSpec apertures for reference. 55
3.2 Representative examples of PSF for the instruments used in this study, corresponding to a 0.06"/pixel scale normalized with the ZScale algorithm. From left to right, panels show ACS-F814W (inner region), ACS-F814W (outer region), WFC3-F160W (inner region), WFC3-F160W (outer region). See Section 3.1 for more details 58

3.3 Steps in bright cluster + ICL modelling (in this case for cluster MACS 1149) for the F160W band. Upper panels show the original image (left) and the galaxy/ICL models (right). Lower panels show the residual image before and after median filtering (left- and right-hand panel respectively). The colorbar denotes the pixel intensity in counts/s. See Sections from 3.2 to 3.3 for more details 65
3.4 Magnitude comparison between "hot+cold" mode as described in P21, and the "super hot" mode used in this work. Note, the magnitude difference is primarily within 0.05 mags. 66
3.5 Magnitude distributions for sources in the BUFFALO catalogs across all clusters. We subdivide each of the catalogs, one per cluster and per parallel/infall field, into inner (in) and outer (out) regions, which correspond to different depth regimes. 67
3.6 Photometric validation of BUFFALO catalogs. Scatter plot of Δmag = $\mathrm{mag_{in}} - \mathrm{mag_{out}}$ as a function of the input magnitude for the different bands considered in this work. The solid line shows the rolling mean magnitude offset and the shaded area corresponds to the inter-quartile range. Additionally, each panel includes the input magnitude histogram (top horizontal histogram) as well as the Δmag histogram (right vertical histogram). 70
3.7 **Top panel:** Comparison of magnitude distribution in the F160W band between BUFFALO sources (solid lines) and HFF (broken lines) for both the cluster and parallel (par) fields in the deepest part of the images for MACS 1149. **Bottom panel:** Ratio between the histograms in the top panel for the cluster field (blue open circles) and parallel field (orange crosses). Other fields show similar behavior 72
3.8 Comparing the quality of photometric redshifts estimated through SED fitting of overlapping galaxies in the HFF and BUFFALO. Blue points correspond to BUFFALO measurements and orange points correspond to HFF measurements. Upper panel: zphot vs. zspec comparison. Blue and orange points are spectroscopic redshifts with 17 ¡ F 160W ¡ 27 selected in the BUFFALO sample, the solid line shows the 1:1 relationship, and the dashed lines encloses the zphot = zspec$\pm$0.15(1+zspec) threshold used to identify outliers (i.e., catastrophic errors). NMAD scatter (σ) and outlier fraction (η) are reported on the top-left corner. Lower panel: Δz $\equiv$ zphot $-$ zspec scatter (red dots are spectroscopic objects) with the median bias indicated by a solid line; dashed lines represent the threshold for catastrophic errors as in the upper panel. 73

3.9 Assessing the quality of photometric redshifts estimated through SED fitting. Upper panel: zphot vs. zspec comparison. Blue points are spectroscopic redshifts with 17 < F 160W < 27, the solid line shows the 1:1 relationship, and the dashed lines encloses the zphot = zspec±0.15(1+zspec) threshold used to identify outliers (i.e., catastrophic errors). NMAD scatter (σ) and outlier fraction (η) are reported on the top-left corner. Lower panel: $\Delta z \equiv$ zphot − zspec scatter (red dots are spectroscopic objects) with the median bias indicated by a solid line; dashed lines represent the threshold for catastrophic errors as in the upper panel. 77
3.10 Redshift histograms for each cluster field. Dotted line corresponds to the redshift of the cluster. Sources were chosen with mag$AB_{F160W} < 28.5$ and χ^2/ndof < 5. 78

4.1 Photometric redshift distribution of BUFFALO high-redshift candidate galaxies in Abell 370. 84
4.2 Covariance matrix of the cluster field. 90
4.3 Results of correlation function for galaxies z>6 for all fields combined (left), the cluster field (middle), and the parallel field (right). We show the measurements for each of the deflection maps, and without any deflection (orig, blue points). The parallel field is only covered by the CATS map, so all the other maps match with the original measurements. 91
4.4 Measurement and best-fit model for the parallel field, using the CATS maps deflections. 92
4.5 The black-filled circle corresponds to the galaxy bias value measured in this work. The other shapes correspond to the previous works, as labeled in the legend, that measured galaxy bias at varying redshifts. 94

5.1 Caption 98
5.2 MHD measurements as a function of aperture for the ICL and κ maps in the Abell 370 cluster. The ICL and κ map comparisons are denoted with circles, where the color corresponds to each individual κ map. The MHD comparing the κ maps to eachother are denoted with a $\times$. 99
5.3 Left: Original DES Abell 370 image in g-band, Right: Residual after model subtraction, showing that only part of the Intra cluster light and the background fluctuations are left after the model subtraction. 103
5.4 Difference in S'ersic index between the closest HST and JWST overlapping bands where the bluer band is subtracted from the redder band. Orange points correspond to $n_{\mathrm{F200W}} - \mathrm{F160W}$. Blue points correspond to $n_{\mathrm{F105W}} - n_{\mathrm{F090W}}$. 104

List of Tables

2.1 Frontier Field cluster and parallel field positions, along with clusters' mean redshift ($z_{\rm clu}$), virial mass ($M_{\rm vir}$), and X-ray luminosity (L_X) [95] 9
2.2 The Point Spread Function and effective wavelengths for different photometric bands used for the HFF. 10
2.3 Existing multi-wavelength HFF coverage from follow-up programs, as used in the present work. The 5-σ point-source depth was estimated by integrating the noise in a Gaussian PSF aperture with the values of FWHM given in Table 2. 13
2.3 Existing multi-wavelength HFF coverage from follow-up programs, as used in the present work. The 5-σ point-source depth was estimated by integrating the noise in a Gaussian PSF aperture with the values of FWHM given in Table 2. 14
2.4 Flux uncertainty correction factors obtained for the different bands used in this work. 34
2.5 Multiplicative factors applied to each band in the photo-z calibration step. The offsets found in the HST bands are consistent with the median magnitude residual values found in Figure 2.13, showing the robustness of our forward-modelling procedure. 39
2.6 This table contains the correction factors that we apply to Spitzer RMS images for each cluster. The procedure to obtain these correction factors is described in Section 2.2.2. The different columns refer to different IRAC Channels. 42

3.1 The Point Spread Function radius and effective wavelengths for different photometric bands used for the BUFFALO fields. 60
3.2 Best-fit coefficients used to perform the uncertainty correction as a function of flux. 71
3.3 Multiplicative factors applied to each band in the photo-z calibration step. . 75

Chapter 1

Introduction

Galaxy clusters are the bridge between cosmology and astrophysics. They address fundamental questions from the smallest (kpc-size) to the largest (cosmic web-size) scales. Given the importance of clusters in studying the evolution of galaxies and large scale structures, a significant amount of telescope time (from ground and space) has been allocated to observations of clusters. This includes dedicated programs that specifically target rich clusters: the Hubble Frontier Fields (HFF) and Beyond the Ultra Deep Frontier Fields Legacy Observations (BUFFALO). Observations of galaxy clusters are used to address widely varied research topics including: structure formation, gravitational lensing, time delay cosmology, galaxy dynamics and dark matter, dark energy, environmental effects, intracluster medium and high redshift (z) universe (through the gravitational lensing effect). The HFF [95] clusters and their ancillary parallel fields, are a large multi-waveband and extremely deep survey of six clusters performed by the (Hubble Frontier Fields) HST Advanced Camera for Surveys (ACS) in optical bands and Wide-Field Camera-3 (WFC3) in near-infrared

wavelengths (140 orbits) with deep coverage by VLT/MOSFIRE Ks-band and Spitzer mid-infrared wavelengths. BUFFALO [137] is based on the HFF and expands the area by ∼3-4 times per cluster as well as the depth in the cluster core, enabling a better understanding of the galaxy population and matter distribution in these extreme environments.

Galaxy clusters are particularly interesting because they allow us to see the universe from a uniquely privileged perspective due to gravitational lensing. Massive clusters work as natural lenses by distorting and bending the light emitted by background galaxies, magnifying them by up to 100 times, pushing the depth of our observations beyond the technical limits of the Hubble Space Telescope (HST). Given the complicated and crowded nature of these extreme environments, some of the challenges involved in studying galaxy clusters reside in the difficulty of extracting accurate photometry (how much flux, or light, does a galaxy emit?) and morphology (what is the shape of the galaxy we are studying?) in these crowded fields by avoiding overlapping, or "blending", of galaxies and pushing data to the deepest flux levels possible. In addition, potential photometric and selection biases are introduced due to the so-called intracluster light, an amorphous cloud of light emitted by stars and gas that is gravitationally bound to the cluster. To use clusters to address open scientific questions, we need multi-waveband photometric data to deep flux levels and with high spatial resolution for multiple clusters at different redshifts as well as spectroscopic data.

The two themes presented in this work include establishing a robust pipeline for deep HST image-to-catalog data reduction; and using the generated catalog data to bridge themes in cosmology and astrophysics to understand and connect these two scales. I present

the pipeline that I have developed for efficiently creating catalogs of deep and crowded, space-based data for the Hubble Frontier Fields (Chapter 2) and BUFFALO (Chapter 3). These catalogs are made available to the broader scientific community and include galaxy fluxes and properties across different wavelengths and resolutions. They also include models of the point spread functions, intracluster light, bright cluster galaxy modeling.

I have used these datasets as the galaxy sample for two projects that aim to help answer questions on the large-scale structure at large redshifts and on galaxy formation and evolution. Specifically, using the BUFFALO data, I am working on using the catalogs and our data products to understand how galaxies cluster in the very early universe (redshift $>$ 5) (Chapter 4). I also the models of the intracluster light (ICL) I have created to probe the underlying dark matter distribution in clusters and examine if we can use these observables to constrain dark matter modeling at these scales (Chapter 5). The results from this study will help answer whether or not we may be able to use the ICL maps as a prior to inform the construction of new, more reliable, lens maps. It will also help us understand the baryonic process that give rise to the ICL, and the systematics that need to be taken into account when using this as a tracer of dark matter.

The techniques developed in this work are immediately applicable to combining different data in interesting ways to understand the connection between properties at large and small scales, specifically as it relates to the relationship between light and dark matter. Combining multi-resolution ground- and space-based data with various techniques will become key to maximize the performance and synergies between current and upcoming surveys from James Webb Space Telescope (JWST), Roman, Rubin, and Euclid.

Chapter 2

Hubble Frontier Field Clusters and their Parallel Fields: Photometric and Photometric Redshift Catalogs

To develop a comprehensive picture of the primordial building blocks of the universe, identification and study of properties of the youngest galaxies (< 1 Gyr) soon after the Big Bang is essential. Given their enormous distance, these systems are best detected at near-infrared wavelengths. However, because of high sky background at these wavelengths, such observations need to be done from space- i.e. using the *Hubble* Space Telescope (HST) or *James Webb* Space Telescope (JWST). This also requires multi-waveband observations spanning a range of wavelengths from optical and near-infrared. Furthermore, study of galaxies at these redshifts is often biased as we mainly sample the intrinsically brighter populations.

To accomplish the above, very deep multi-waveband observations over a large area are needed to detect statistically representative samples of very high redshift galaxies. This is currently beyond the reach of the largest available telescopes. To achieve such depths, one could leverage the natural phenomenon of gravitational lensing by targeting rich clusters of galaxies. This magnifies fluxes from high redshift sources located behind massive galaxy clusters, helping to probe deeper into the universe. This will be highly beneficial for even after the largest space telescopes (i.e. JWST), with their unprecedented sensitivity, are commissioned. It has been demonstrated that JWST will be able to shed light on the mechanisms that re-ionized the intergalactic medium at $6 < z < 10$ only by exploiting the cluster lensing phenomenon, to observe galaxies with $M < 10^9$.

The *Hubble* Frontier Field program [HFF, 95] is a survey, designed with these objectives in mind. With an allocation of 630 HST orbits, it performed deep observations of six very massive clusters and their parallel fields in optical and near-IR bands, with Advanced Camera for Surveys (ACS) and Wide Field Camera 3 (WFC3), respectively. In addition, each field has been extensively observed in the mid-IR regime (between 3 and $5\,\mu$m) with the Infrared Array Camera (IRAC) on board the *Spitzer* Space Telescope.

The six clusters span the redshift range $0.3 < z < 0.55$ and their magnification power allows detection of galaxies up to $z \sim 9$, i.e. at the re-ionization epoch [see 15, 109]. HFF followed the successful tradition of deep, pencil-beam HST observations as in *Hubble* Deep Field [142], *Hubble* Ultra-Deep Field [HUDF, 18] and CANDELS [83], as well as programs covering wider areas like the Cosmic Evolution Survey [COSMOS, 133] and Galaxy Evolution from Morphology and SED [GEMS, 125]. With respect to galaxy cluster

observations, the Cluster Lensing And Supernovae survey with *Hubble* [CLASH, 121] paved the way for the HFF.

The HFF clusters will be the reference fields for the exploration of the distant universe. At present, additional HST coverage is provided by the "Beyond Ultra-deep Frontier Fields and Legacy Observations" which aims at covering the outskirts of the HFF clusters over the same wavebands and to the same depth, as well as increasing the depth in the centers of the clusters. Most notably, sources in the HFF clusters will also be JWST targets, with some of them already selected by both Guarateed Time Observation teams and an Early Release Science Program[1]. Eventually, the knowledge acquired from the HFF shall be applied to analyze data from an unprecedented number of galaxy clusters that *Euclid* and *Roman* space telescopes will discover by surveying thousands of square degrees of the sky .

Apart from providing access to the high redshift Universe, the HFF will also allow the study of properties of dark matter and the role of 'environment' in the evolution of galaxies at $z < 1$. It will also provide a standard sample of cluster galaxies, to be compared with nearby systems. The HFF parallel fields provide similar data to the same depth, that would minimize selection effects and biases in any environmental study of galaxy populations. The cornerstone of all these studies is a multi-waveband photometric catalog, containing self-consistent photometry for every detected source. Producing such a catalog is particularly challenging, given the depth of the imaging data, analysis of images in the crowded fields, the wide wavelength baseline (which imply substantial changes in the point

[1]Treu et al., program 1324 "Through the Looking GLASS: A JWST Exploration of Galaxy Formation and Evolution from Cosmic Dawn to Present Day".

spread function) required, and contamination from the intra-cluster light (ICL). The task has already been fulfilled by two distinct teams which released their respective HFF catalogs to the astronomical community. Given the challenges mentioned above in identifying individual sources, in performing accurate photometric measurements for the HFF galaxies, and in simultaneously dealing with a multiple parameter space, it is important to apply completely independent techniques to generate catalogs for the same clusters. This allows a better understanding of the final data products, selection effects and the caveats in the data and the data processing pipelines. In particular, the different data reduction steps could introduce systematic effects in the final results, which need to be studied. Such problems and inaccuracies in source identification and photometry will also be reflected into selection of different populations of galaxies. For example, comparing two independent estimates of photometric redshifts can be instrumental to selecting the most robust galaxy candidates at $z > 8$ [102]. The existing catalogs produced from the above mentioned studies contain serious discrepancies in the photometry of the same galaxies. An independent analysis will help us study the origins of these differences.

In this study, we generate new galaxy catalogs for the six HFF clusters and their parallel fields. The results include photometric catalogs, photometric redshifts, Intra-Cluster Light (ICL) maps, and surface brightness models to remove the brightest galaxies from our images in order to detect fainter galaxies to deeper levels. The parallel fields provide ancillary deep-field data and will also serve as control samples. The main differences between the strategy here and the previous methods is that, we provide models of the intra-cluster light maps, as well as perform forward modelling of photometry to characterize

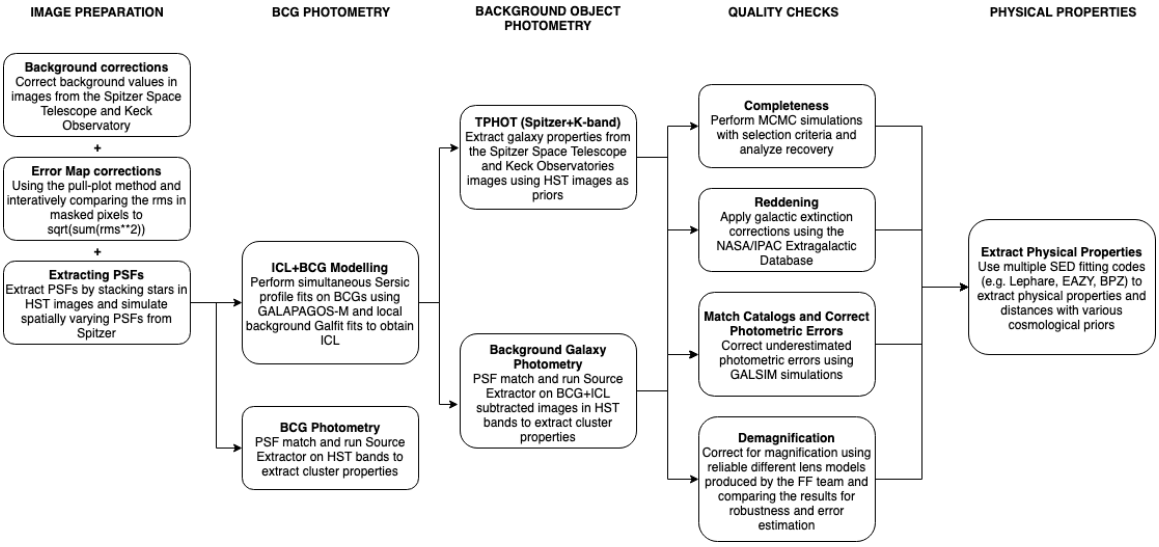

Figure 2.1: Workflow of the data processing as performed in the present work.

biases and uncertainties in flux measurements. Moreover, the pipelines developed for this study will be applied to the new BUFFALO data (Pagul et al., in prep.) to extend the HFF catalogs to wider areas, providing self-consistent data for the HFF and BUFFALO galaxies.

Throughout this work we assume standard cosmology with $\Omega_M = 0.23$, $\Omega_\Lambda = 0.76$ and $H_0 = 73$ Km/sec/Mpc. Magnitudes are in the AB system.

2.1 The Data

2.1.1 HST observations

The HFF observations are the deepest of galaxy clusters to date, and second only to the HUDF when also considering the blank fields. This results from a total of 840 orbits, performed through coordinated HST parallel observations in the following filters: F435W, F606W, F814W in ACS, and F105W, F125W, F140W, F160W in WFC3. These seven

Table 2.1. Frontier Field cluster and parallel field positions, along with clusters' mean redshift ($z_{\rm clu}$), virial mass ($M_{\rm vir}$), and X-ray luminosity (L_X) [95]

Field	Cluster Center (J2000)	Parallel Center (J2000)	$z_{\rm clu}$	M_{vir}
A370	02:39:52.9, -01:34:36.5	02:40:13.4, -01:37:32.8	0.375	1×10^{15}
MJ0717.5+3745	07:17:34.0, +37:44:49.0	07:17:17.0 +37:49:47.3	0.545	$\sim 2 - 3 \times 10^{15}$
MJ0416.1-2403	04:16:08.9, -24:04:28.7	04:16:33.1, -24:06:48.7	0.396	1.2×10^{15}
AS1063	22:48:44.4, -44:31:48.5	22:49:17.7, -44:32:43.8	0.348	1.4×10^{15}
A2744	00:14:21.2, -30:23:50.1	00:13:53.6, -30:22:54.3	0.308	1.8×10^{15}
MJ1149.5+2223	11:49:36.3, +22:23:58.1	11:49:40.5, +22:18:02.3	0.543	2.5×10^{15}

bands reached a depth of $m_{AB} \sim 29$ mag for point sources within a 0.4" diameter aperture [95]. Through a different program, UV observations in the F275W and F336W filters of two HFF clusters, Abell 2744 and MACS J0717, were carried out with details presented in [6].

The gravitational potential of the clusters' halo, besides binding together the galaxies in the system, produces a lensing magnification that could detect background objects to an *intrinsic* brightness of 30–33 mag, i.e. 10–100 times fainter than previous surveys. Details of the HFF survey design are provided in [95]. In Table 2.1 we report the main characteristics of the six clusters, with a summary of the observations in Table 2.1.1. The filter throughput for the ACS and WFC3 instruments are shown in Figure 2.2 (upper panel). We use mosaics that have been reduced by the Frontier Fields team [2], with a pixel scale of

[2]https://archive.stsci.edu/prepds/frontier/

Table 2.2. The Point Spread Function and effective wavelengths for different photometric bands used for the HFF.

Band	$FWHM$	λ_{pivot} (Å)
F275W	0.075”	2707
F336W	0.109”	3355
F435W	0.109”	4329
F606W	0.112”	5922
F814W	0.111”	8045
F105W	0.175”	10551
F125W	0.176”	12486
F140W	0.172”	13923
F160W	0.173”	15369
Ks	0.364”	21524
I1	1.29”	35634
I2	1.42”	45110
I3	1.50”	57593
I4	1.84”	79595

Note. — Representative PSF FWHM values for the photometric bands in this study. These values were calculated for the Abell 2744 cluster. Bands F275W and F336W are only available for Abell 2744 and MACS J0717. IRAC Channels 3 and 4 are only available for Abell 2744, Abell 370, Abell S1063, and MACS J0717.

0.06"/pix. These images have been reduced using the HST science data products pipeline [83]. Data from other HST programs using the same filters have also been included by the HFF team, with all the exposures aligned relative to each other using `Tweakreg`. Other steps in the reduction process include: correction of standard imaging artifacts; bad pixel and cosmic ray rejection; geometric distortion correction and image stacking using `AstroDrizzle` [56]. Throughout this work we will focus on the analysis and detection of these previously reduced and calibrated data.

2.1.2 Ancillary data

A number of independent observations of the HFF have generated complementary data to that available from the HST. The *Spitzer* Space Telescope dedicated more than 1,000 hours of Director's Discretionary time to obtain IRAC 3.6 μm (channel 1) and 4.6 μm (channel 2) imaging down to the depths of 26.5 and 26.0 mag., in cluster and parallel fields respectively. These observations are crucial for photometric redshift measurement, for identifying low-redshift interlopers, and are beneficial in constraining galaxy properties since they provide a good proxy for galaxy stellar mass. In addition, there are legacy IRAC observations at 5.8 μm (channel 3) and 8.0 μm (channel 4) which are also included in our analysis[3]. To produce the Frontier Fields mosaics, the following *Spitzer* Program IDs were used:

- Abell 2744: 83, 90275
- MACS J0416.1-2403: 80168, 90258

[3] retrieved from the Spitzer Hertiage Archive https://sha.ipac.caltech.edu/applications/Spitzer/SHA/

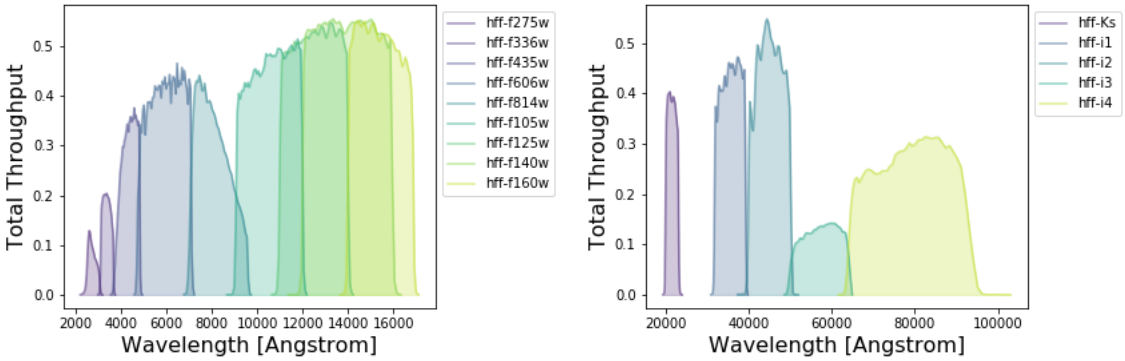

Figure 2.2: Throughput of the nine HST filters (*upper panel*) and ancillary Ks-band and IRAC bands (*lower panel*) used in this analysis.

- MACS J0717.4+3745: 40652, 60034, 90009, 90259
- MACS J1149.4+2223: 60034, 90009, 90260
- Abell S1063 (RXC J2248.7-4431): 83, 10170, 60034
- Abell 370: 137, 10171, 60034

Another follow-up program is the K_s-band Imaging of the Frontier Fields [KIFF 26], carried out with the High Acuity Wide Field K-band Imager (HAWK-I) at the Very Large Telescope (VLT). This reached a depth of 26.0 mag (5σ, point-like sources) for Abell 2744, MACS-0416, Abell S1063, and Abell 370 clusters in the southern hemisphere. The K-band imaging campaign of the HFF also used the Multi-Object Spectrometer for Infrared Exploration (MOSFIRE) at Keck to observe MACS-0717 and MACS-1149 in the northern hemisphere to a 5σ depth of 25.5 and 25.1 mag respectively.

Table 2.3 provides a summary of the available ancillary data, with their filter transmission curves shown in Figure 2.2 (right panel).

Table 2.3. Existing multi-wavelength HFF coverage from follow-up programs, as used in the present work. The 5-σ point-source depth was estimated by integrating the noise in a Gaussian PSF aperture with the values of FWHM given in Table 2.

Field	Observatory	Wavelengths	Depth
Abell 370	VLT/HAWK-I	$2.2\mu m$	~ 26.18
	Spitzer IRAC 1,2	$3.6\mu m$, $4.5\mu m$	~ 25.19, 25.09
	Spitzer IRAC 3,4 (cluster-only)	$5.8\mu m$, $8.0\mu m$	~ 23.94, 23.39
MACS J0717.5+3745	Keck/MOSFIRE	$2.2\mu m$	~ 25.31
	Spitzer IRAC 1,2,3,4	$3.5\mu m$, $4.5\ \mu m$	~ 25.04, 25.17
	Spitzer IRAC 3,4	$5.8\mu m$, $8.0\mu m$	~ 23.94, 23.39
MACS J0416.1-2403	VLT/HAWK-I	$2.2\mu m$	~ 26.25
	Spitzer	$3.5\mu m$, $4.5\ \mu m$	~ 25.31, 25.44
Abell S1063	VLT/HAWK-I	$2.2\mu m$	~ 26.31
	Spitzer IRAC 1,2	$3.6\mu m$, $4.5\mu m$	~ 25.04, 25.04
	Spitzer IRAC 3,4 (cluster-only)	$5.8\mu m$, $8.0\mu m$	~ 22.96, 22.64
Abell 2744	VLT/HAWK-I	$2.2\mu m$	~ 26.28
	Spitzer IRAC 1,2	$3.6\mu m$, $4.5\mu m$	~ 25.32, 25.08

Table 2.3 (cont'd)

Field	Observatory	Wavelengths	Depth
	Spitzer IRAC 3,4 (cluster-only)	$5.8\mu m$, $8.0\mu m$	$\sim$ 22.78, 22.45
MACS J1149.5+2223	Keck/MOSFIRE	$2.2\mu m$	$\sim$ 25.41
	Spitzer	$3.5\mu m$, 4.5 μm	$\sim$ 25.24, 25.01

2.1.3 Modeling the point spread function in different bands

Accurate knowledge of the point spread function (PSF) as a function of wavelength and optical system is crucial to perform consistent photometry within a 'panchromatic' baseline. Knowledge of the PSF for HFF galaxies is needed to reconstruct their intrinsic morphology as well as mapping the ICL (Section 2.1.4). To perform consistent multi-waveband photometry, taking into account band-to-band variations, we need to convolve images to the same PSF. This task, known as "PSF matching", is performed via kernel convolution. Images in multi-wavelength surveys are often affected by different diffraction levels, which make it difficult to obtain homogeneous measurements e.g. of aperture photometry. Figure 2.3 illustrates the broad range of PSF sizes by showing postage stamps extracted from a few HFF images from $\sim$ 0.3 to 3.6μm. Besides the optical performance of the instrument itself, the final PSF model also depends on the specific observing strategy of the survey (depth, dithering, etc.) and in the case of ground-based facilities also on the seeing conditions (in the case of Figure 2.3, VLT/HAWK-I).

For HST data (divided between cluster vs. parallel fields), PSFs were estimated

by stacking unsaturated stars. We use `IRAF` to visually inspect stellar light curves and determine whether an object is saturated. Then we stack unsaturated stars using the `IDL` routine `Star Finder` [43]. The resulting PSF models used in PSF-matching are 2.34×2.34 postage stamps in the HST and Ks bands, and 28.56 for *Spitzer*. These sizes are chosen in order to enclose diffraction spikes (as one can see in Figure 2.3).

Our procedure works well for the HST images and the $K_{\rm s}$ band as the variation of the PSF across the image is small. However, stacking unsaturated stars does not produce a robust result in the mid-IR *Spitzer* channels. This is due to large variations of the PSF as a function of the position on the image as well as the asymmetry of its shape. This makes IRAC PSFs depend on the orientation of the camera. Moreover, IRAC Channels 1 and 2 pixels undersample the response of a point source. Thus, instead of `Star Finder`, we use a synthetic pixel response functions (PRF) that combines the information on the PSF, the detector sampling, and the intrapixel sensitivity variation in response to a point-like source. A PRF model for a given position on the IRAC mosaic is generated by the code `PRFMap` (A. Faisst, private communication) by taking into account the single-epoch frames contributing to that mosaic. To do so, `PRFMap` stacks individual PRF models with the same orientation of the frames, resulting in a realistic, spatially-dependent PSF model (an example for IRAC channel 1 is shown in Figure 2.3).

We use `GalSim` in order to calculate the FWHM for each PSF/PRF listed in Table 2.1.1. More specifically, we use the `calculateFWHM` function, which computes the maximum intensity of the PSF, I_0, the centroid of the PSF intensity, the first pixel from the centroid at which the intensity is $I < I_0/2$ and the last pixel at which the intensity

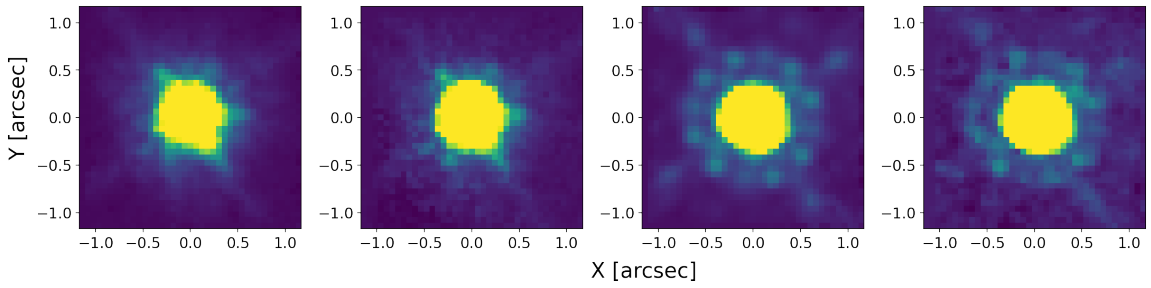

Figure 2.3: Representative examples of PSF for the instruments used in this study, corresponding to a 0.06"/pixel scale normalized with the `ZScale` algorithm. From left to right, panels show F336W (WFC3), F606W (ACS), F125W (WFC3), K_s (VLT), IRAC Channel 1 (*Spitzer*). See Section 2.1.3 for more details

is $I > I_0/2$, and then linearly interpolates between these two to estimate the value of the FWHM. For the Spitzer bands, we input into this function an averaged stack of all the normalized PRFs modelled in the field for a more conservative estimate.

2.1.4 Modeling the intra-cluster light

Given the richness of HFF clusters, those fields are particularly crowded with a significant probability of having cluster members aligned along the same line of sight of more distant background galaxies. The analysis of background systems is also impaired by the ICL, i.e. the residual emission from stars that are generally not bound to any cluster galaxy [112, 113, 128]. Blending between ICL and bright cluster galaxies is also a source of uncertainty. In an effort to alleviate these effects we attempt to model ICL and cluster members using GALFIT [118] and GALAPAGOS-2 [14, 60] respectively, following a similar procedure as in [113]. Because the severity of the ICL-galaxy blending decreases towards the bluer wavelengths, we perform these fits for all but the bluest HST bands used here (i.e., $F275W$ and $F336W$).

In this Section we focus on ICL modeling, while in Section 2.1.5 we will describe the procedure to fit the brightest cluster members. Subtracting their flux from the images will allow us to detect some of the faintest objects that otherwise would remain hidden by their over-shining neighbors (see discussion in Section 2.2).

To model the ICL we follow the methodology presented in [113]. We first run `Source Extractor` [20, hereafter `SE`] on each image/band to get a first-pass estimate of the morphological parameters of detected galaxies, and their segmentation map. In this way we can create a mask removing the detected pixels of sources fainter than 26 mag, as the fitting procedure (described below) is less reliable below that threshold. Then we produce a 18×18 arcsecond (300×300 pixel) patch for every remaining source, with the patch centered at the coordinate identified by `SE` as the centroid of the galaxy. By means of `GALFIT`, we simultaneously fit single Sérsic profiles to all the objects included in that patch. For patches whose `GALFIT` fits failed in the first instance, we randomly move the cutout center, creating five additional 18×18 arcsecond patches on which we run the same algorithm.

It should be noted that the number of patches across the field depends on the projected density of sources. This is illustrated in Figure 2.4 (left panel) by showing a representative "coverage map" for Abell 2744. In case a given pixel with coordinates (x, y) is only included in one cutout, the ICL emission ($F_{\rm ICL}$) is defined as the local background measurement found by `GALFIT` (namely, the `sky value` parameter). If there are overlapping cutouts in (x, y), we use the inverse χ^2-weighted mean of their background measurements:

$$F_{\rm ICL}(x,y) = \frac{\Sigma_i s_i(x,y)/\chi_i^2(x,y)}{\Sigma_i 1/\chi_i^2(x,y)} \ , \tag{2.1}$$

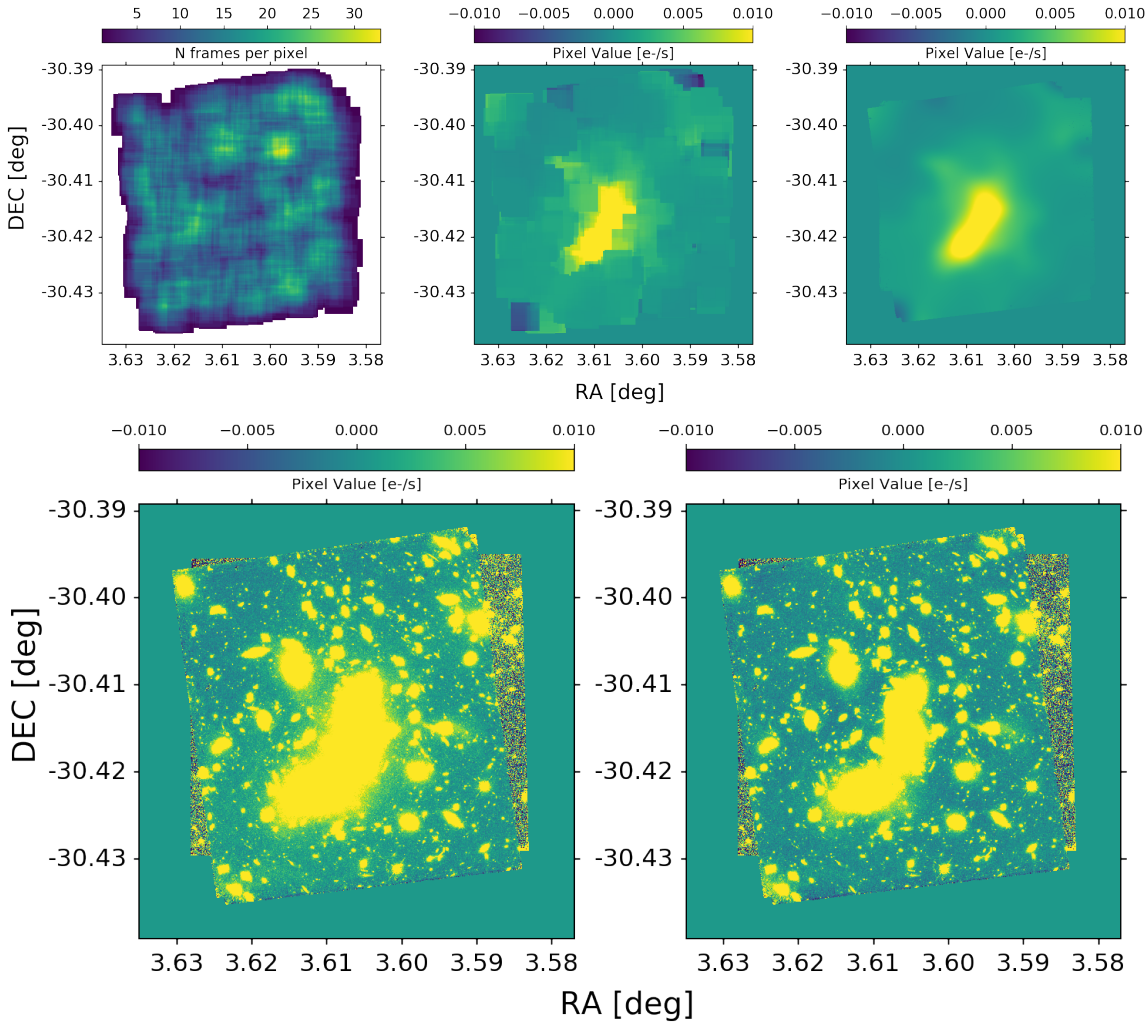

Figure 2.4: We illustrate the steps to generate the ICL map (as described in Section 2.1.4). Here the example is presented for the F160 band in Abell 2744. **Top Row:** *Left panel:* the "coverage map" showing the number of fit cutouts that overlap with each pixel. *Middle panel:* the resulting ICL map for the same band and cluster created by combining the fit background value of each cutout. Overlapping stamps are stacked using Eq. 3.1. *Right panel:* Final ICL map after smoothing the map in the Middle panel with a representative Gaussian kernel. More details about kernel creation as provided in section 2.1.4. **Bottom Row:** *Left panel:* Original Abell 2744 F160W science image. *Right panel:* F160W image after smoothed ICL (top row, right panel) subtraction.

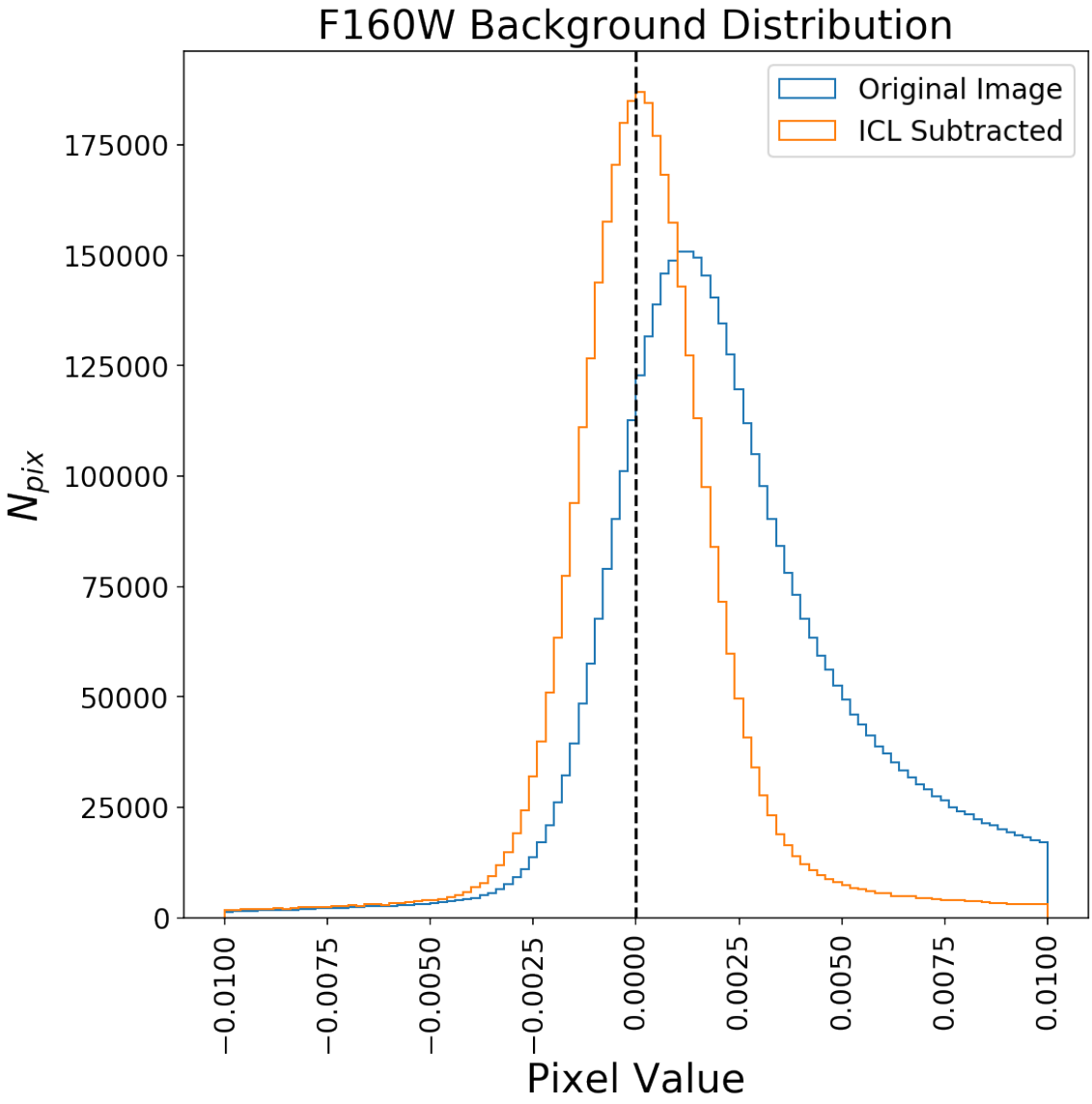

Figure 2.5: Pixel values of the original background (blue histogram) and after ICL subtraction (orange histogram); the vertical dashed line marks the zero value.

where s_i and χ^2_i are the `sky fit` and χ^2 values from `GALFIT` for the i-th cutout. The overall ICL map, in the case of Abell 2744, is shown in Figure 2.4 (middle panel).

The merged ICL map, represented by $F_{ICL}(x, y)$, may still contain some sharp features due to the finite nature of the cutouts used to build it. In order to avoid these features we introduce an additional step to the method presented in [113] by smoothing the merged ICL map with a Gaussian kernel. The size of this kernel is chosen by analyzing the (radially averaged) power spectrum of the coverage map (see the left panel of Figure 2.4) defined as $P(k) = \sum_{x,y} I_{r(x,y)} e^{-ikr}$, where r is the radial distance from the center of the image, $r = \sqrt{(x - x_0)^2 + (y - y_0)^2}$; x, y are the coordinates of each pixel, $I_{r(x,y)}$ is the value of the coverage map at the pixel x, y at a distance r from the center, and x_0, y_0 are the coordinates of the center of the image. We find this scale to be at $k \simeq 0.08$, i.e. about 72 pixels, or 4.32 arcseconds. In the right panel of Figure 2.4 we can see that this strategy successfully mitigates the impact of sharp features in the merged ICL map. As a sanity check, we generate a histogram of the sky background by masking sources using the corresponding segmentation map. We then compare this between the original image and the ICL subtracted image. We find that the resulting histogram of background pixels is both more symmetric, narrower, and centered at zero in the ICL subtracted image (Figure 2.5).

The resulting map, shown in Figure 2.4 for the Abell 2744 cluster, not only serves as a representative model of the ICL, but also as a background correction for the entire HFF mosaic. Figure 2.4 also shows the difference between the original map (middle image) and the one after kernel filtering (right-most image): The sharp flux gradients caused by

finite box numbers and sizes is mitigated.

To model the ICL in the K_s and *Spitzer* images we use a local background routine built into the `T-PHOT` software [106], which calculates a background template for each object and merges them into a single image. As done in the optical and other near-infrared bands, we smooth the image with a representative kernel and subtract the result from the HFF mosaic. The smoothed ICL mosaics will be released as two-dimensional arrays in the same units (ADU/s) as the HFF mosaics.

2.1.5 Removal of the Bright Galaxies in Clusters

After correcting the cluster images for ICL and sky background, we model the brightest galaxy members of each cluster (i.e. galaxies with $\mathrm{MAGAUTO_{F160W}} < 19$). These objects are selected via a first-pass `SExtractor` run in the F160W band. The aim is to remove them and their diffuse light so that one could push the observations deeper. We use the publicly available code `GALAPAGOS-M`[4] [14, 60], which is a software that automates source detection and bulge-disk Sérsic modeling, and takes advantage of multi-wavelength information in its parameter fits.

The advantage of using `GALAPAGOS-M` is in its ability to perform single and multi-component (bulge/disk decomposition) fits and to input galaxies using information from multiple bands *simultaneously*. In order to robustly measure color gradients in large galaxies, we restrict the degrees of freedom in the `GALAPAGOS-M` fits by imposing a wavelength dependency (with a quadratic function) for the half-light radius and Sérsic index. Compared to fitting morphology independently in each band, this approach is more stable and

[4] https://github.com/MegaMorph/galapagos

tightens the constraints of the morphological parameters measured for each galaxy [see 60]. However, a multi-component model is susceptible to overfitting the images; therefore, we use the residual flux fraction [RFF, as in 65] to assess the number of components that most effectively models the light profile of bright cluster members; such residual flux is obtained by subtracting the model from the input image. The residual flux fraction is a measure of signal excess in the residual image, not due to background fluctuations, and is defined as

$$\mathrm{RFF} = \frac{\sum |I_{x,y} - I^{\mathrm{model}}_{x,y}| - 0.8 \times \sum \sigma_{\mathrm{BKG},x,y}}{\sum I_{x,y}} \ , \tag{2.2}$$

where $I_{x,y}$ and $I^{model}_{x,y}$ are respectively the observed and model fluxes for a given pixel with coordinates (x, y), while $\sigma_{\mathrm{BKG,x,y}}$ is the background RMS in the same location. We sum over the pixels associated to a given galaxy. The 0.8 factor is included to ensure that the mean RFF of an image is null when it is exclusively affected by Gaussian noise with constant variance. For a given object to fit, we favor either a single- or two-component model depending on which of them results in the smallest RFF. Generally, studies of galaxy morphology require the RFF relative difference between two models, i.e. $(\mathrm{RFF}_1 - \mathrm{RFF}_2)/\mathrm{RFF}_1$, to be larger than 1.0–1.6 [e.g., 65]. This is a conservative threshold for the selection of the multi-component fit (RFF_2) to prevent over-fitting. Here, we are more concerned about effectively removing the flux of a given galaxy (to get a smaller residual) rather than providing a realistic description of its morphology. For this reason we select the multi-component solution when $\mathrm{RFF}_2 < \mathrm{RFF}_1$.

After the modelling process and subtracting both ICL and bright cluster members, we apply a median filter to the cleaned image. This is a well-known smoothing technique

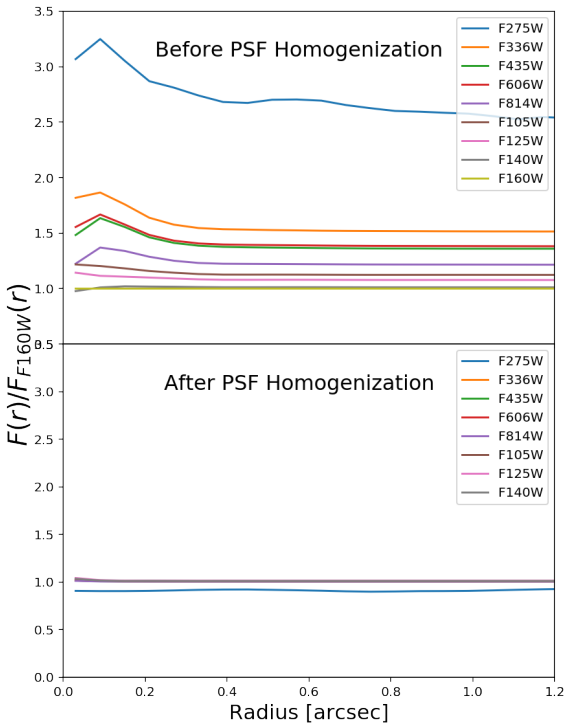

Figure 2.6: Growth curves for each HST-derived PSF normalized by the F160W growth curve before (top) and after (bottom) homogenization.

that replaces the value of a given pixel by the median of its neighboring pixels [see 106]. We use a filter with a box size of 1 deg per side. We apply this filtering only to pixels with a flux within 1σ of the background level in order to reduce the effects of over-subtraction in the residual. The resulting improvement can be seen in the bottom-right panel of Figure 2.7. Note that this process does not affect the outskirts of the cluster.

2.2 Source extraction

2.2.1 HST detections

After performing the modelling described in the previous section, we homogenize the various HST bands by matching their respective PSFs. Images in a panchromatic data set, especially if they sample a wide wavelength range like extra-galactic surveys, are usually affected by different PSF shapes (see Figure 2.3). This means that the fraction of the flux that falls inside an aperture, as well as the resulting noise, varies as a function of bandwidth and pivotal wavelength.

PSF matching is a convolution procedure to solve these problems by reshaping multi-wavelength images into a common reference system having certain resolution and diffraction properties [i.e., the same "target" PSF, see 139, 5]. It has become a standard technique to measure consistent fluxes over a range of wavelengths [e.g., 53] and from different instruments under varied observing conditions [e.g., 89] to effectively characterize the spectral energy distribution (SED) of the observed galaxies.

Specifically, we use the PSF models derived in Section 2.1.3. In our case, the target PSF is the one in the F160W band as it is the reddest HST band. To convert the other HST images we use a convolution kernel obtained by taking (in Fourier space) the ratio between their original and target PSFs.Note that in some cases, the target PSF is marginally smaller than the original. Despite this, we are able to relate target and original PSF since we do not require the convolution kernel to be positive-definite. We show the growth curves for the PSFs extracted from the HST data, normalized by the growth curve of the F160W PSF before and after homogenization, in Figure 2.6. We note that after PSF homogenization,

the normalized growth curves are, on average, agree within 2% for all bands except F275W, which agrees at the 8% level. PSF matching is not applied to ground-based images nor *Spitzer*: their resolution is appreciably lower than the HST bands and in that case the photometric extraction is performed with a different method (see Section 2.2.2).

We then proceed to perform source photometry for each HST image using `SE`. The strong clustering of the objects in the HFF images pose the additional problem of detection completeness because the objects that are close pairs along the line of sight are not always successfully deblended by the software. To improve the extraction process, we create a co-added IR image from the weighted mean, using their inverse variance as weights, of four WFC3 bands (namely F105W, F125W, F140W, and F160W). Such a stacking enhances the signal-to-noise ratio of faint sources, being effectively deeper than any individual band. We use the stack of infrared images as a detection image, running `SE` in dual mode.

Moreover, given the variety of scientific goals, it is important to precisely measure both the bright galaxies in the foreground and the fainter galaxies in clusters. However, source extraction with `SE` is a trade-off between rigorous source deblending of galaxies close to each other on the angular plane, and spurious shredding of structure from a single galaxy. For this reason, previous works [30, 57, 52, and references thereon] proposed a "dual mode", or High Dynamic Range (HDR), approach with a cold mode and a hot mode `SE` run, where the cold mode detects and performs photometry on the objects contained within visually reliable Kron radii and the hot mode more aggressively deblends and performs photometry on the smallest and faintest objects. Given the aggressive deblending of the hot mode, it can break up larger objects into individual pieces, which we discard when considering the

cold catalog. We modify the HDR approach described in [52] and discard galaxies from the hot mode that fall within a 0.2 × Kron radius [85] of a cold mode detected object. We show the resulting magnitude distributions of this process in Figure 2.8.

To alleviate the possibility of fake source detection around the residuals, we utilize the Kron radius of the modeled object and discard objects which fall within it. Furthermore, we remove sources corresponding to diffraction spikes and those susceptible to edge effects on the perimeter of the images. This procedure is performed on both the cluster and parallel fields.

We present the magnitude histograms in the F814W band for each cluster and their parallel fields (Figure 2.9). It shows the overabundance of bright galaxies in the clusters when compared to the parallel fields. We note that even after ICL+bright galaxy subtraction, the presence of such bright objects diminishes our ability to detect faint objects. We also show the ratio of number counts between the cluster and parallel fields in the F814W and F160W bands (Figure 2.10). The observed trend here is consistent across all clusters, demonstrating the importance of having parallel fields with comparable depths.

2.2.2 Photometry in lower resolution images

In addition to HST, we also rely on imaging observations from Keck, VLT, and *Spitzer*. Those facilities have lower angular resolutions than the HST instruments, increasing the blending between sources. In order to maximize the information extracted from each image, we use the prior-based code `T-PHOT` [106]. This code uses the high-resolution HST images and their corresponding `SE` catalogs as priors to perform dual-mode photometric extraction in the lower-resolution images. This allows measurement of blended sources that

are not directly detectable in K_s or IRAC bands. On the other hand the method misses the so-called "HST dark" sources, i.e. galaxies so faint in optical and near-IR that are not identified in the prior image, even though they are sufficiently bright to be visible in the low-resolution image. HST dark sources may constitute a hidden population of galaxies providing a non-negligible contribution e.g. to the cosmic star formation rate density budget [see 141]. However, the identification of HST dark sources is subsequent to the creation of an HST-based catalog and shall be addressed in future work.

Concerning the *Spitzer* images, before running `T-PHOT` we perform a series of corrections related to the weight maps (defined as the inverse variance per pixel, i.e. $1/\sigma^2$) using the pull diagnostic [58], described as follows. Assuming the distribution is Gaussian, in principle, the ratio between the variable and its standard deviation should produce a Gaussian with a standard deviation (σ) equal to one. In the limit of large statistics (owing to the Central Limit Theorem), we can approximate the signal on the background pixels to follow a Gaussian distribution. For this purpose, we compute the distribution of the ratio between the background level and its standard deviation, $\sigma_{\rm bkg}$. Such a distribution is expected to have a standard deviation $\sigma_{\rm pull} \approx 1$ if $\sigma_{\rm bkg}$ is properly estimated. A value of $\sigma_{\rm pull} < 1$ means that the uncertainties are likely underestimated, and $\sigma_{\rm pull} \gg 1$ means that the uncertainties are likely overestimated. In order to have conservative values for the error maps, we multiply these by $\sigma_{\rm pull}$ when the latter is greater than one. For Spitzer channels 1, 2, 3, and 4 we only correct the error maps in the largest contiguous region where the cluster and parallel fields are located. We check that this is a good approximation since the resulting corrected background distributions show a single peak. The corrected errors,

$\sigma_{\rm pull}$, are discussed in section 2.7.

As the high resolution prior, we use the science image in the F160W band and the segmentation map created from the weighted IR stack. Previous studies [37, 52] found that `SE` tends to underestimate the isophotal area of objects in a single-band detection image; such a systematic effect is inversely proportional to the flux. A solution to this issue [52, 105] is to dilate the segmentation areas of individual sources. We verify how prominent this effect is by comparing one of the HFF clusters (Abell 370) to the deeper BUFFALO survey, given that the isophotal area increases with increasing signal-to-noise. We choose to compare the HFF IR stack, given its depth, to the BUFFALO F160W band. We find that when using the IR stack the isophotal area of each source is slightly larger, with minimal dependence on the area. The difference is small enough that we found it unnecessary to dilate the segmentation map before feeding it into `T-PHOT`.

We run `T-PHOT` for the Ks- and IRAC bands. Because the IRAC PSF varies across the field of view, we take advantage of `T-PHOT` "multikernel" option, which allows for the inclusion of a separate kernel for each object. These kernels are generated from the grid of PRFs produced by `PRFMap`, as described in Section 2.1.3. We emphasize that the output provided by `T-PHOT` (namely, the parameter `FitQty`) is an estimate of the *total* flux emitted by the given source.

2.3 Validation of the photometric catalog

2.3.1 Quality and completeness via simulations

To measure the completeness, we add randomly distributed simulated objects in the observed image and then try to recover them. The number of the simulated objects should be high enough to cover the full field of view and avoid statistical fluctuations, while their surface density should be low enough not to further increase the already large fraction of overlapping sources in the images. This way, we still check the performance of the deblender without introducing an unrealistic number of new blends.

In order to measure completeness we injected 100 point-like sources in the original images, with magnitudes randomly assigned from a uniform distribution between $23 < mag_{AB} < 31$. The magnitudes of these objects were selected to be the same in all bands, which allows us to compute the IR-weighted magnitude straightforwardly. This was done to simplify interpretation of the results. The processing of these images, was performed using the same steps presented in previous sections. We generated two sets of simulations (hereafter called 'flavors'):

- one set where we assign the position of the injected objects randomly within the image. We will refer to these simulations as flavor 1;
- a set where we assign the centroid position of the injected objects randomly within the empty parts of the image, i.e., where the segmentation map has no detected pixels. We will refer to these simulations as flavor 2.

The reason behind the generation of two sets of simulations is that in the first

flavor the fraction of blended objects is overestimated, since we are randomly placing new sources in a field that is already overcrowded. This leads to a pessimistic characterization of our pipeline's performance. However, using the second flavor, we explicitly avoid overlap with other sources. In the latter case the quality assessment will be over-optimistic.

Ten independent realizations were generated for each of these flavors, The injected sources were independently generated for each cluster as 15 arcsec-side noise-free square cutouts. We then formed a collage of the same size of the original image, and added this collage to the original image of each cluster. Therefore, only the original noise in the HFF mosaics is affecting the present test. This is a good approximation for faint sources, where the background dominates over the shot noise due to the source itself.

After the injection of simulated sources, these images are analysed by the same software used for the real catalog (see previous Sections). We compare the output to the list of input (simulated) sources, and their intrinsic vs. recovered properties. We considered a source successfully recovered if there is an entry in the output catalogs whose centroid is within 0.6 arcseconds (10 pixels) from the input location, and the offset between intrinsic and extracted magnitude is <0.5 mag. These thresholds have been chosen to minimize the number of by-chance matches between simulated and real sources, allowing at the same time for some difference between the input and output values.

Results from this test are summarized in Figure 2.12. For flavor 2 simulations, we find that completeness is above 60% for magnitudes brighter than 29, and above 80% for most of the clusters up to magnitude ~ 28. This confirms the estimated depth of our images and catalogs. When we do not avoid overlap between the objects (i.e., using flavor

1 simulations) the overall completeness decreases noticeably with respect to the simulation where we avoid blending. Thus, we expect the actual completeness of our catalog to be somewhere in between the pessimistic scenario portrayed by our flavor 1 simulations and the optimistic case of our flavor 2 simulations.

2.3.2 Photometric uncertainties

Given the complexity of the process to detect objects and measure their flux in different bands, an analytic derivation of their associated uncertainties (in flux, position, and other derived quantities) becomes almost intractable. Forward-modeling will enable us to characterize such uncertainties. To this purpose, we inject another set of simulated objects into the original HFF mosaics. This time the simulated sources are realistic galaxy models from the GREAT3 challenge [110], created by means of `GalSim` [126]. `GalSim` is a modular, open-source code to render any type of astronomical images. We opted for the GREAT3 library because it includes models with realistic morphology, obtained by fitting deep COSMOS images with multiple Sérsic profiles [see 99, 98]. Given that the galaxies from the GREAT3 challenge available in the `GalSim` catalog only have information for the F140W band, we identify these galaxies in the [89] catalog using their ID values to obtain the magnitudes in the other bands used in our study. In this way we have realistic colors for our injected galaxies across the entire photometric baseline, with the assumption that their morphology does not vary significantly from band to band. We also ensure that the centroid positions are the same across different bands. We convolve each galaxy profile with the corresponding PSF. The 15 $\times$ 15 square arcsec cutout containing the injected

objects (and no additional noise) are then added to the original image. We then repeat the photometric extraction process in a similar fashion to what have been done with our data. In particular, we inject 80 objects randomly placed in each image and generate 12 different realizations (images) of those objects in all the HFF bands.

Additionally, we also process the cutouts that only contain the injected objects using the same pipeline; we use the outcomes as "ground truth" to be compared to the catalog resulting from the injection-recovery procedure. To match the two samples we use the same strategy as in Section 2.3.1. The photometric residuals for each match are then measured. The results are shown in Figures 2.13 and 2.14, indicating an unbiased estimate of input magnitudes across different HST bands included in this study ($\langle \mathrm{mag}_{meas} - \mathrm{mag}_{input} \rangle <$ 0.1 mag), even after ICL subtraction. However, for the IRAC and K bands we find that the recovered objects appear, on average, dimmer than the input. Since the dependence in flux is mild, we decided to include a constant offset to correct for these residuals. In particular, we shift the recovered magnitudes by the median of the residuals found in Figure 2.14. These offsets are $\Delta\mathrm{mag} = (0.04, 0.189, 0.195)$ for Ks, IRAC channel 1, and 2, respectively, and are subtracted from the measured magnitude. We explored different possibilities for the origin of this correction including: size of segments in the segmentation map, and the smoothing radius of the ICL profile. However, after modifying these we could not find any significant changes in the initial offsets that we measured. Given their mild dependence on the flux, and the fact that the effect seems to be milder in Ks, where the PSF is closer to that in the HST bands, we concluded that the observed offsets may be a consequence of numerical instabilities at the time of using the PSF kernel that relates the low and high-

resolution images. We notice that the injected sources cover different magnitude ranges for different bands, due to the fact that we are injecting galaxies with realistic SEDs from COSMOS. Additionally, we see a different behavior when we compare different bands. In particular, the uncertainties for the recovered fluxes in the F160W band seem to be smaller than in most of the other bands. The reason behind these differences is the larger depth of the images in F160W compared to the other bands. It is particularly interesting to notice larger uncertainties derived for F275W compared to the other HST bands. This is a combination of two factors: first, the SNR for F275W is the lowest of all HST bands; second, this is also the bluest band, where we expect the largest morphological differences with respect to our segmentation map.

We only perform the simulations for the cluster fields. The reason is that we expect these fields to outperform the parallel fields as the later are not affected by the ICL and are less crowded. As a consequence, our measurements for the clusters will set an upper limit for the photometric biases and uncertainties in the parallel fields. As shown in Figure 2.16, the photometric bias appears to be uncorrelated with position when comparing cluster core offsets with those in the outer regions. Since the source extraction steps in both cluster fields, and parallel fields are the same, the validation tests of the photometric measurements in the cluster fields are also applicable on the parallel fields.

Our forward modeling approach allows us to estimate the accuracy of the flux errors as reported by `SE`. Using the injected galaxies we compute the forward-modeling estimation of the uncertainty in the flux, which we call $\delta F_{\rm FM}$, as the RMS of the difference between the measured flux for the injected sources and the input flux, $\delta F_{\rm FM} = \sqrt{\langle (F_{\rm meas} - F_{\rm input})^2 \rangle}$,

Table 2.4. Flux uncertainty correction factors obtained for the different bands used in this work.

Band	a	b
F275W	11.00	0.32
F336W	3.67	0.11
F435W	3.32	0.23
F606W	3.23	0.27
F814W	7.29	0.24
F105W	10.46	0.21
F125W	7.54	0.08
F140W	8.88	0.37
F160W	5.17	0.45
Ks	1.58	0.29
I1	42.31	0.78
I2	46.94	0.71
I3	3.38	0.74
I4	1.09	1.18

where $F_{\rm meas}$ is the measured flux and $F_{\rm input}$ is the injected flux. This estimation is performed in linearly spaced magnitude bins (with a binwidth of 1.6 mag). We then compare $\delta F_{\rm FM}$ to the mean uncertainties reported by `SE` in each of the bins, i.e. $\langle \delta F_{\rm SE} \rangle$. This is done by studying the ratio $r_{\rm corr} = \frac{\delta F_{FM}}{\delta F_{SE}}$ as a function of flux. We fit the resulting ratio to an exponential model $r_{\rm corr} = AF^b$ and use this fit to correct the reported uncertainties for each detected object. The ratio and resulting fit are shown in Figure 2.15 for F160W, $K_{\rm s}$ and IRAC channel 1. The best-fit values for a and b can be found in Table 2.3.2. By binning the data we lose information about the effects of blending and correlations between flux uncertainties for individual galaxies, but get a more robust estimation of the overall uncertainty of the ensemble.

2.3.3 Comparison with previous work

There are other independent studies of the Frontier Fields. Given the complexities of extracting photometry in these deep and crowded fields, it poses a great challenge to determine photometric properties of the objects detected with the desired accuracy. Therefore, we believe there is merit in both exploring the limits of our photometric pipeline and comparing with previous results. Figure 2.17 shows how our photometry compares with that of the previous teams, ASTRODEEP ([105], [33], [40], [24]) and DeepSpace ([135]) for intersecting bands. For the HST bands, we note that there is general agreement in the photometry between the three methods within 0.05 magnitudes up to $m_{AB} \sim 23$ mag. Beyond this magnitude, our photometry agrees best with the ASTRODEEP team, which could be the result of our reduction procedure being more similar to theirs. Furthermore, we see that the three datasets are statistically compatible up to magnitude ~ 25.5 in most bands. However, in the fainter end, there are statistically significant differences between the DeepSpace and ASTRODEEP datasets, and the data presented in this work. These differences are probably due to the difference in modelling, as the measure of fluxes/magnitudes depends on the concrete choices for apertures, etc. However, we check that the colors are consistent among these datasets for the HST and Ks bands, which can be inferred by the consistent behavior found in most bands. Thus, for applications where colors are most important (e.g., photometric redshifts) any of these datasets should give similar results (as evidenced by our photometric redshifts).

2.4 Photometric redshifts

Having the self-consistent SEDs for individual galaxies in each of the HFF clusters and their associated parallel fields, we now measure the photometric redshifts using `LePhare` [7, 66]. The code fits galaxy templates to the observed SEDs to derive a redshift likelihood function ($\mathcal{L}$) for each source. Photometric redshift estimates ($z_{\rm phot}$) are then defined as the median of $\mathcal{L}(z)$. The template library adopted here is the same used in [89] since it was shown that it works efficiently across a wide redshift range (up to $z \sim 6$). The library is built by spiral and elliptical galaxy models from [120] along with other ones derived from the stellar population synthesis model of [29]. The latter is used to reproduce both young quiescent and starburst galaxies. For each model we produce different templates by changing their dust attenuation between $0 < E(B-V) \leq 0.5$ and assuming either [122] or [31] extinction laws depending on the galaxy type (see 89 for more details). When [31] is chosen, we produce three alternate versions by adding different parametrization of the 2,175 Åbump [see 68]. Absorption by the intervening inter-galactic medium is also implemented as prescribed in [96]. We also add the main nebular emission lines in rest-frame optical to the templates corresponding to the star-forming SEDs, modelling line fluxes and their ratios as in [127].

Before running `LePhare`, a modification is required to the HST bands: the fraction of the flux lost by `SE` isophotal measurements (FLUX_ISO) must be taken into account. FLUX_ISO provide more accurate colors than FLUX_AUTO, which is another `SE` photometric measurement specifically designed to recover total flux by means of an adaptive aperture [cf. 85]; therefore the former are prefreed for $z_{\rm phot}$ computation. However, our

ancillary photometry is extracted with `T-PHOT`, which does not provide an equivalent to FLUX_ISO. Therefore, we include in our baseline $K_{\rm s}$ and IRAC total fluxes while HST bands fluxes are rescaled by a factor

$$f_{\rm tot} = \frac{\sum_i w_i (\text{FLUX\_AUTO}/\text{FLUX\_ISO})_i}{\sum_i w_i}, \tag{2.3}$$

i.e. the weighted mean of the AUTO-to-ISO flux ratio summed over the observed HST bands. Weights are defined as $w = \sqrt{\sigma^2_{\rm AUTO} + \sigma^2_{\rm ISO}}$.

In order to empirically correct for systematic effects we perform a calibration that relies on the spectroscopic redshifts ($z_{\rm spec}$) available in each field. The sample includes spectroscopic data from several programmes retrieved from the NASA/IPAC Extragalactic Database[5] The spectroscopic campaigns contributing to the majority of the data set are described in [114, 45, 124, 12, 140, 131, 88, 97]. We also include more recent observations carried out by [87] in Abell 370, which were not included in previous photometric redshift analysis in the literature. The calibration procedure is as follows. First, we run `LePhare` on the HFF galaxies with known spectroscopic redshifts after fixing their redshifts to their spectroscopic $z_{\rm spec}$ value. We only consider galaxies with a reliable spectroscopic redshift, i.e. with a "quality flag" >3.[6] We do not apply any magnitude cut. Once obtained the best-fit solution from `LePhare` (i.e., the fitting model resulting in the smallest χ^2) we measure in each photometric band the difference between the observed flux and the prediction by

[5]The NASA/IPAC Extragalactic Database (NED) is funded by the National Aeronautics and Space Administration and operated by the California Institute of Technology (http://ned.ipac.caltech.edu).

[6]It is common practice that the persons responsible for the $z_{\rm spec}$ measurements assign a quality flag, ranging from 1 to 4, following the scheme proposed for the first time in [92], where a flag equal to 4 corresponds to the highest confidence level

the best-fit template. To find the systematic offset (in a given band) we compute the average difference in the spectroscopic sample. Since results are similar in the six fields, we eventually consider only the offsets measured for the Abell 370 cluster because it has the largest number of spectroscopic sources (320 of them reliable spectroscopic redshifts). These offsets, when applied to the photometric baseline, will compensate for a possible bias in the template library and/or for calibration issues in data reduction. In the HST bands the corrections are between 2 and 5%, except for the F425W filter which is 8%; a similar value is found for $K_{\rm s}$ while in the IRAC channels 1 and 2 the correction is a factor 1.11. We note that similar offsets (namely, 0.1 mag in both IRAC channels 1 and 2) have been found by `LePhare` also in another extragalactic survey [103]. All offsets are quoted in Table 3.5.1, with the exception of IRAC channels 3 and 4 since the systematics here would be mainly driven by the absence of dust re-emission in the templates [see 103]. To take such a limitation into account we increased the error bars in these two channels by adding 0.5 mag in quadrature, under-weighing in practice their contribution to the fit.

We fit the SED of 1,423 spectroscopic galaxies with $16 < F160W < 26$ across the six clusters to assess $z_{\rm phot}$ quality. The calibration offsets (Table 3.5.1) are taken into account. Similar to the previous work [e.g., 28], the scatter is defined as the normalized median absolute deviation [NMAD 64], i.e.

$$\sigma_{\rm NMAD} = 1.48 \times {\rm median}\left(\frac{|\Delta z - {\rm median}(\Delta z)|}{1+z_{\rm spec}}\right), \tag{2.4}$$

with $\Delta z \equiv z_{\rm phot} - z_{\rm spec}$. The incidence of catastrophic errors η is defined as the fraction of

Table 2.5. Multiplicative factors applied to each band in the photo-z calibration step. The offsets found in the HST bands are consistent with the median magnitude residual values found in Figure 2.13, showing the robustness of our forward-modelling procedure.

Band	Multiplicative Factor
F275W	1.04
F336W	1.02
F435W	1.07
F606W	0.99
F814W	0.96
F105W	0.98
F125W	1.01
F140W	1.02
F160W	1.01
Ks	1.00
I1	1.11
I2	1.11

redshift outliers having $|\Delta z| > 0.15(1+z_{\rm spec})$. For pathological PDF(z) where the median is not a good approximation of the main peak of the PDF, we used the redshift corresponding to the minimum χ^2 solution (as in [36]). For the entire sample $\sigma = 0.067$ and $\eta = 10.3\%$ (Figure 2.18, upper panel). After excluding the outliers we also recompute the mean of Δz to asses the so-called redshift bias [e.g., 100], which is 0.012 in our case. We repeat the same procedure for the parallel fields, in which a total of only 62 spectroscopic redshifts are available. In that case we estimate $\sigma = 0.044$ with no outliers. Individual cluster field redshift comparisons are shown in Figure 2.19. In this figure, the comparison is made using the highest quality spectroscopic redshifts. Figure 2.20 also shows the photometric redshift distribution for objects in each cluster SED fits with a reduced $\chi^2 < 10$.

2.5 De-magnification

Leveraging the fact that these HFF clusters exhibit some of the strongest lensing currently observed, we calculate and include lens model magnification factors for all relevant objects in our final catalog (i.e. for those objects with redshifts larger than the clusters' mean redshifts). We use the lens models provided by Bradač [63, and references therein], Caminha [32], CATS [72, and references therein], DIEGO [42, and references therein], GLAFIC [78, and references therein], Keeton [101, and references therein], Merten & Zitrin [108, and references therein], Sharon [75, 74], and Williams [73, and references therein] lens modeling teams. We use a script (D. Coe, private comm.) that functions in a similar way to the Interactive Model Magnification Web Tool[7] by utilizing the available mass (kappa, κ) and shear (gamma, γ) maps to directly calculate the magnification factors, and provide the value of the magnification factor, μ, for each lens model in separate columns included in the photometry catalog. Concretely, we compute μ as follows:

$$\mu = \frac{1}{(1-\kappa)^2 - \gamma^2}. \tag{2.5}$$

For more information about how these lens models are constructed, we refer the reader to the HFF Lens Modeling webpage[8].

[7] https://archive.stsci.edu/prepds/frontier/lensmodels/#magcalc
[8] https://archive.stsci.edu/prepds/frontier/lensmodels/

2.6 Data Products

The final data catalog resulting from this work is accompanied by: (i) the PSF models; (ii) the ICL maps and the bright galaxy models; (iii) median filtered science images with the ICL and galaxy models subtracted; and (iv) photometry, redshift, and magnification catalogs. A brief description of the produces is given below:

i. The PSF models for the HST and Ks bands are released as 2.34x2.34 square arcsecond (39x39 square pixel) fits file arrays. The total flux density of the arrays representing the PSF model is set to unity. IRAC PRFs used in this work are available upon request since they vary across the focal plane.

ii. The ICL maps and the bright galaxy models are fits arrays of the same resolution and dimensions as the science images. They also use the same units as the science images, that is, ADU/s.

iii. The ICL+bright galaxy subtracted median filtered images are also fits arrays of the same resolution and dimensions as the science images, in ADU/s units. These are the files on which detection was applied.

iv. The photometric and redshift catalogs are ascii files for each cluster. We also include the photometric offsets used in the photometric redshift calculation in a README file in case the user would like to apply these offsets to the given photometries. Galactic extinction has been applied when calculating photometric redshifts using the $E(B-V)$ values derived from the dust maps presented at [130]. However, the photometric catalogs do not have galactic extinction applied.

Table 2.6. This table contains the correction factors that we apply to Spitzer RMS images for each cluster. The procedure to obtain these correction factors is described in Section 2.2.2. The different columns refer to different IRAC Channels.

Cluster	$I1$	$I2$	$I3$	$I4$
Abell 370	3.12	2.68	1.03	1.02
MACS J0717.5+3745	2.98	2.74	0.90	0.83
MACS J0416.1-2403	3.04	2.88	0.91	0.86
Abell S1063	2.96	2.73	-	-
Abell 2744	5.83	4.44	0.88	0.85
MACS J1149.5+2223	2.82	2.56	-	-

2.7 Error correction

In this section we show correction factors applied at various stages in the pipeline. The values for the error map correction from pull-plots calculated in Section 2.2.2 are shown in Table 2.7.

2.8 Conclusions

In this work we present and publicly release catalogs of the six Frontier Field clusters and their parallel fields. This includes a total of $>$ 33,500 objects across a wide wavelength range, 0.275 - 8 μm. We release maps of the intra-cluster light and bright galaxy models. We have outlined the complexity involved in performing this analysis in a crowded field with bright cluster members and intra-cluster light that could bias the measurements. We have successfully removed the contamination from these sources to further reduce the image into a "blank field" on which we can detect the faintest objects in the field without biasing the flux measurements of objects on the perimeter of the field of view. We perform

an error analysis using `GALSIM` by injecting COSMOS-like galaxies to both estimate the errors and to analyse the validity of our pipeline. We note there is no evident photometric bias close to the cluster core as compared to the outskirts.

We estimate the photometric redshifts for objects in all six clusters and their parallel fields as measured by `LePhare`. When compared to the available spectroscopic redshifts for the HFF clusters, this gives a combined outlier fraction of 10.3% and a redshift bias of 0.012 after excluding the outliers.

We find some differences in our photometry measurements with those from the literature and note the importance of cross-checks between datasets in such crowded and complex environments. We demonstrate the utility of performing source injection, where knowledge of ground truth is accessible to calibrate measurements and characterize biases and uncertainties.

We have scripted a pipeline to analyze each of the Frontier Fields in an efficient, streamlined, and reproducible manner. We plan to apply a similar version of the pipeline to the next generation survey of the Frontier Fields, namely the BUFFALO survey [137] which expands these same fields in area by a factor of 3-4 and pushes the 5-σ depth $\sim$ 1 magnitude fainter.

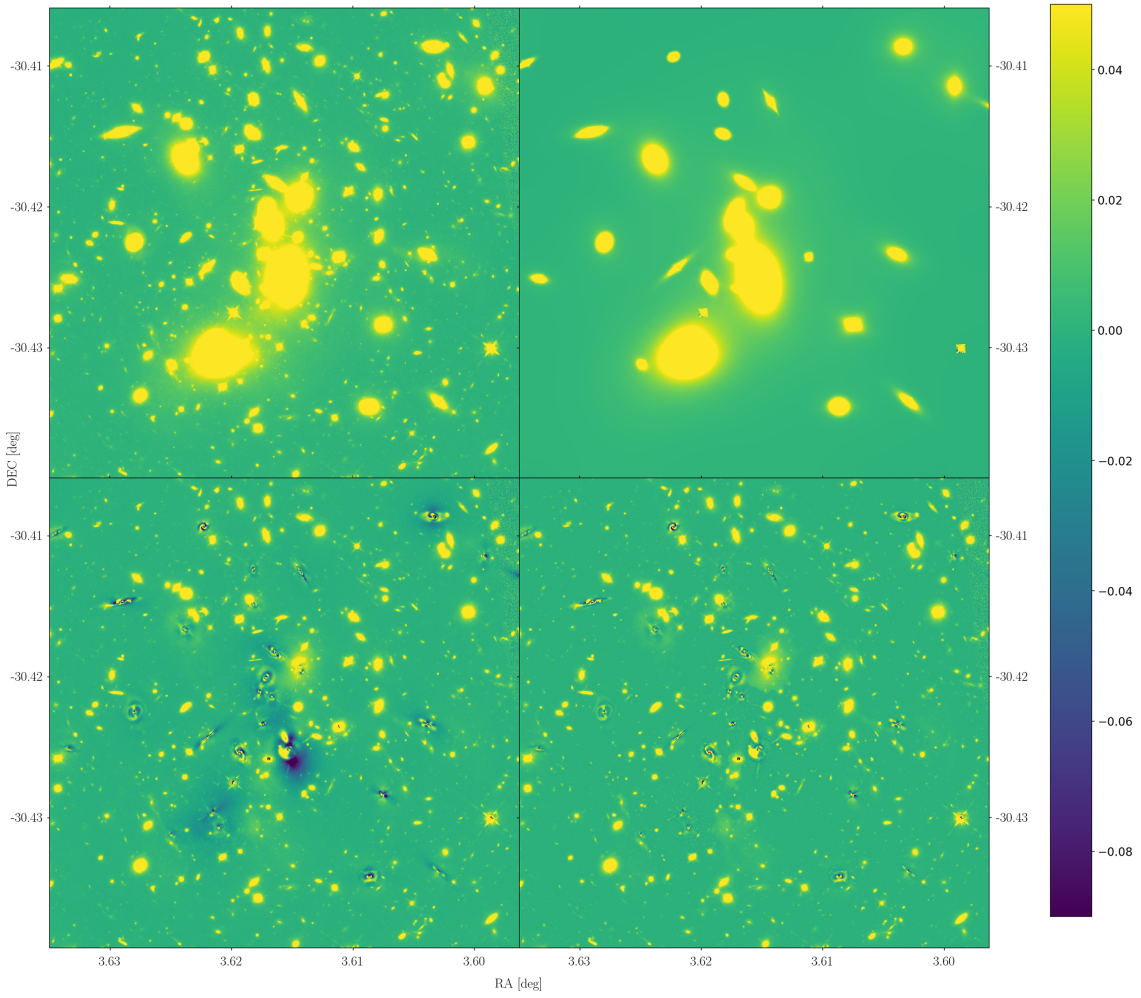

Figure 2.7: A summary of the various steps in bright cluster + ICL modelling (in this case for cluster Abell 2744). Upper panels show the original image (left) and the galaxy/ICL models (right). Lower panels show the residual image before and after median filtering (left- and right-hand panel respectively). The colorbar denotes the pixel intensity in counts/s. See Sections from 2.1.4 to 2.1.5 for more details.

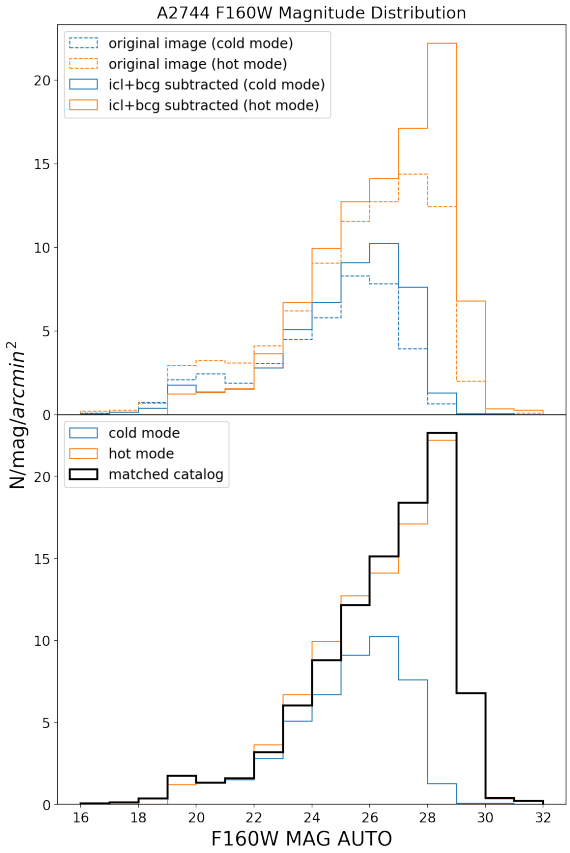

Figure 2.8: Magnitude distributions for the objects detected using the cold (blue) and hot (orange) modes for the original image v. ICL+BCG subtracted image (top) and ICL+bcg subtracted image (bottom); matched (black) refers to total number of galaxies detected and kept in the catalog per magnitude bin. We see a significant increase in the number of detected galaxies in the cluster subtracted image, as well as a slight shift in mean magnitude toward fainter objects.

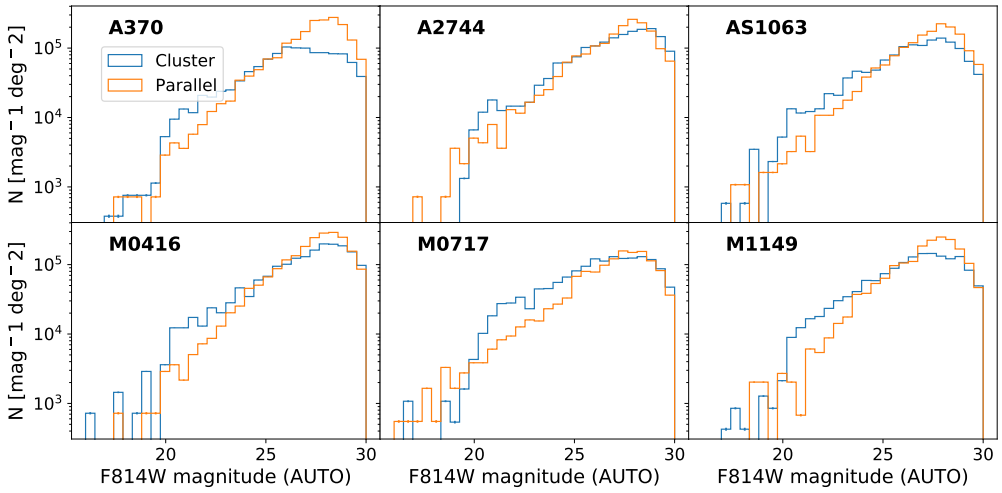

Figure 2.9: Comparison of magnitude distributions for the HFF cluster and their parallel fields. This clearly shows the excess in number of galaxies in clusters compared to the field. It also shows the field and cluster samples have similar depths.

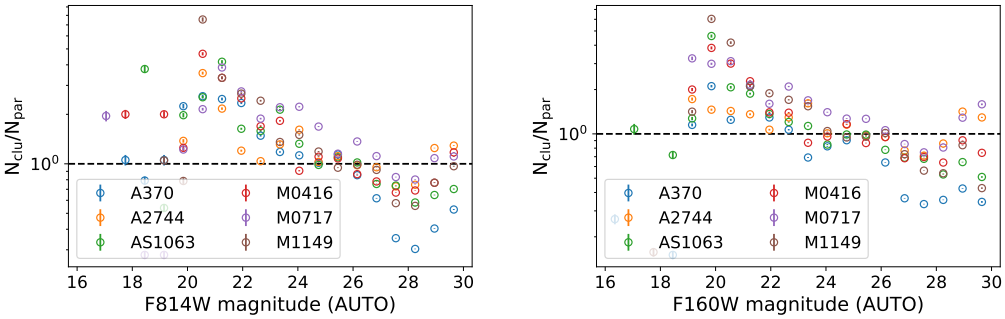

Figure 2.10: Ratio between magnitude distributions in the parallel and cluster fields for all HFF clusters in the F160W band (top) and F814W band (bottom). The excess of field galaxies over clusters in fainter magnitude bins is likely caused by non-detection of faint sources in clusters due to diffuse light from more luminous objects.

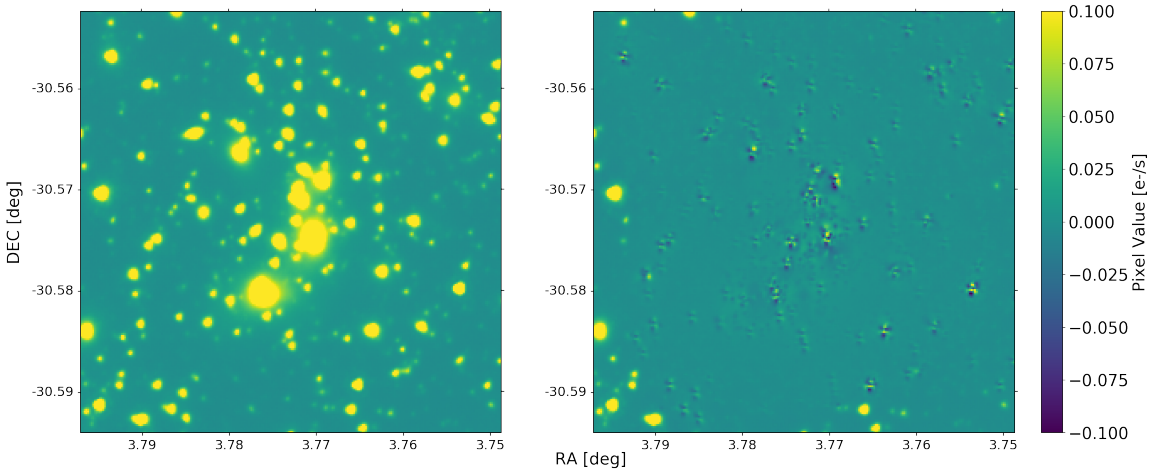

Figure 2.11: (Left to right) Original IRAC Channel 1 image in Abell 2744 (*left panel*) compared to the residual map (*right panel*) after subtracting `T-PHOT` galaxy models (see Section 2.2.2).

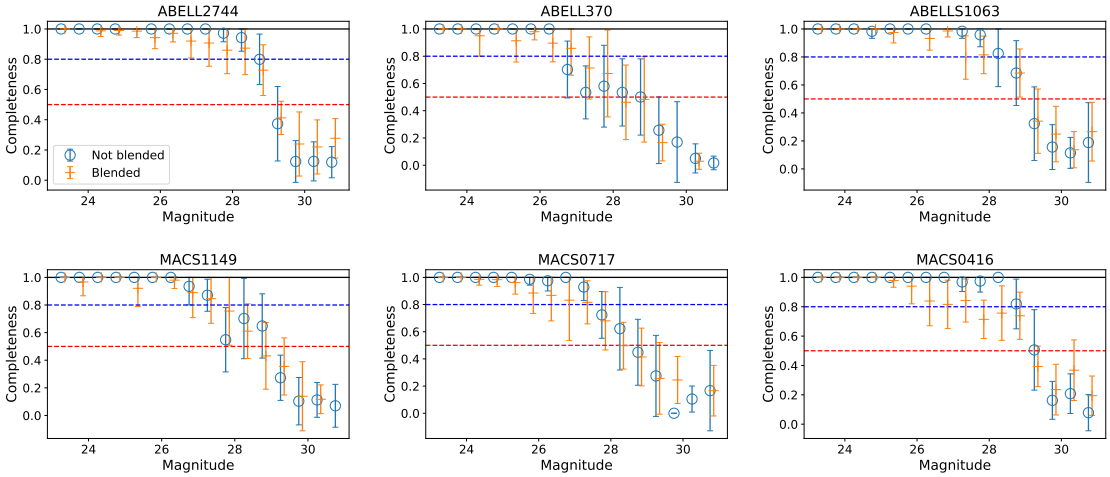

Figure 2.12: Completeness as a function of magnitude for injected point-like sources between 24 and 30 mag in the six analyzed clusters (*top row*: Abell 2744, Abell 370, Abell S1063; *bottom row*: MACS1149, MACS0717, MACS0416). The positions of these objects were randomly assigned within the footprint (open circles – flavor 1, i.e., not blended) or randomly assigned in empty parts of the segmentation map (crosses – flavor 2). We introduce a small horizontal offset of the different markers and only include the error-bars for the flavor 2 case in order to improve readability. We also add horizontal solid line to mark 100% completeness, and two dashed lines at 80% and 60% completeness as visual help. Detections are made in IR-weighted images.

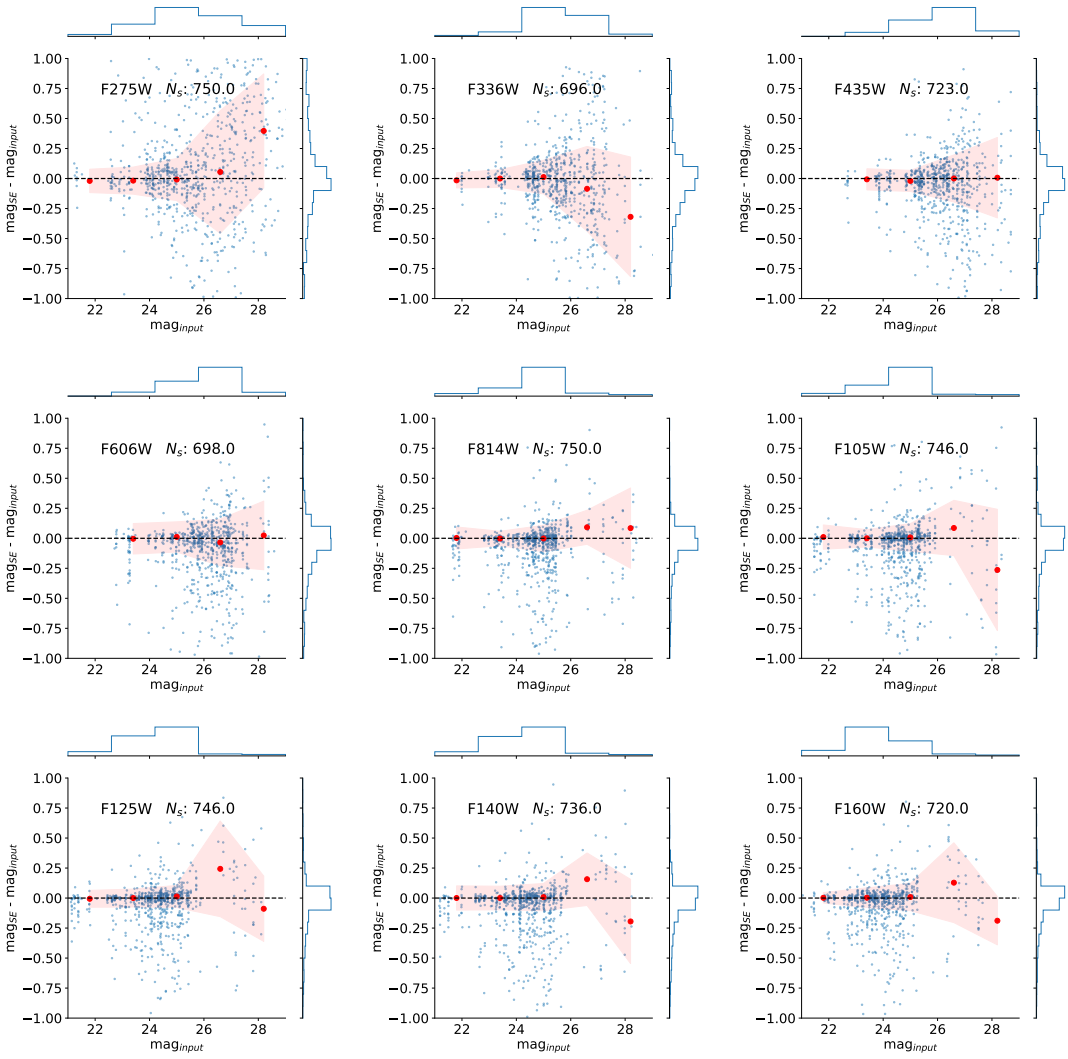

Figure 2.13: Photometric residuals between the simulated objects injected in the Abell 2744 cluster and the input fluxes, plotted as a function of magnitude for different bands. In each panel, blue small dots are the individual objects residuals, while the red dots represent the median in bins with 1.6 mag width. The shaded region encompasses the rescaled interquartile range, $0.7413(Q3 - Q1)$ as a robust estimator of 1σ uncertainty [69]. The magnitude distribution of each injected sample is projected on the x axis on the top of the corresponding panel, while the photometric residual distribution is shown in the right-hand side of the y axis.

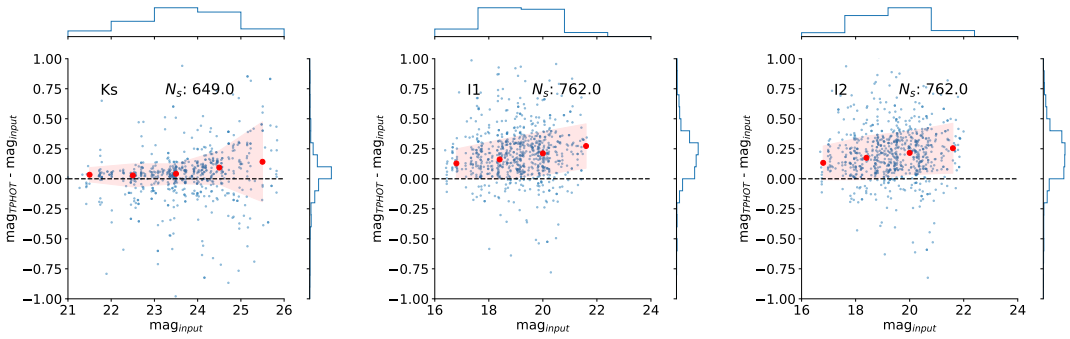

Figure 2.14: Photometric residuals in ancillary data (K_s band and *Spitzer*/IRAC channels). See the caption of Figure 2.13 for more details. We find a photometric bias between input and measured magnitude that we correct using the median value of the residual in each band.

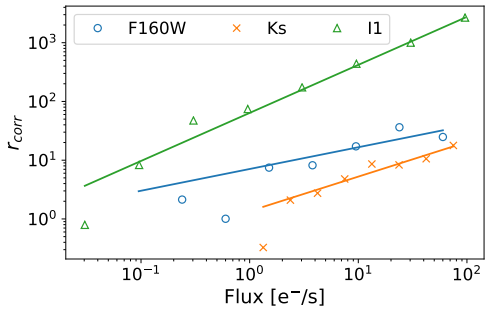

Figure 2.15: Ratio between the flux uncertainty recovered via forward-modeling and the reported flux uncertainty by Source Extractor in three different bands: F160W (open circles), Ks (×), and IRAC Channel 1 (open triangles). For each band, a solid line shows the corresponding best-fit model, i.e. the power law $r_{\rm corr}(F) = aF^b$. The best-fit values found for a and b in the different bands can be found in Table 2.3.2.

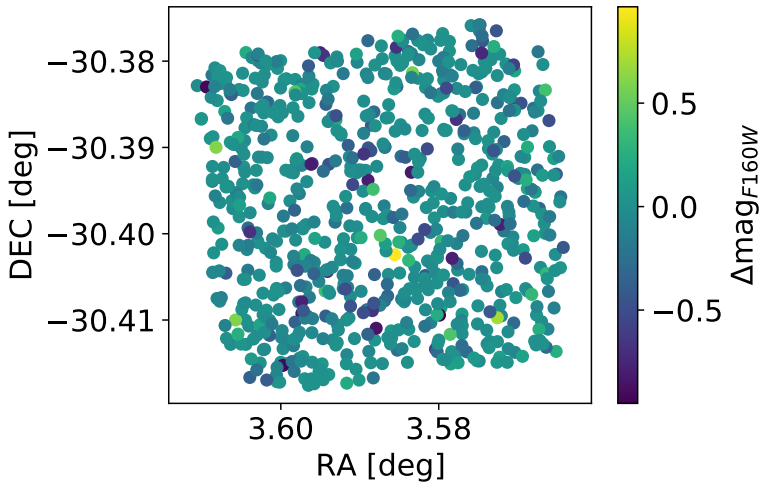

Figure 2.16: $\Delta\text{mag} = \text{mag}_{\text{output}} - \text{mag}_{\text{input}}$ for the F160W band as a function of the position of detected injected objects for the Abell 2744 cluster. There is no clear correlation between the residual and the position of the injected object in the field. Similar results are observed for the rest of the bands analyzed.

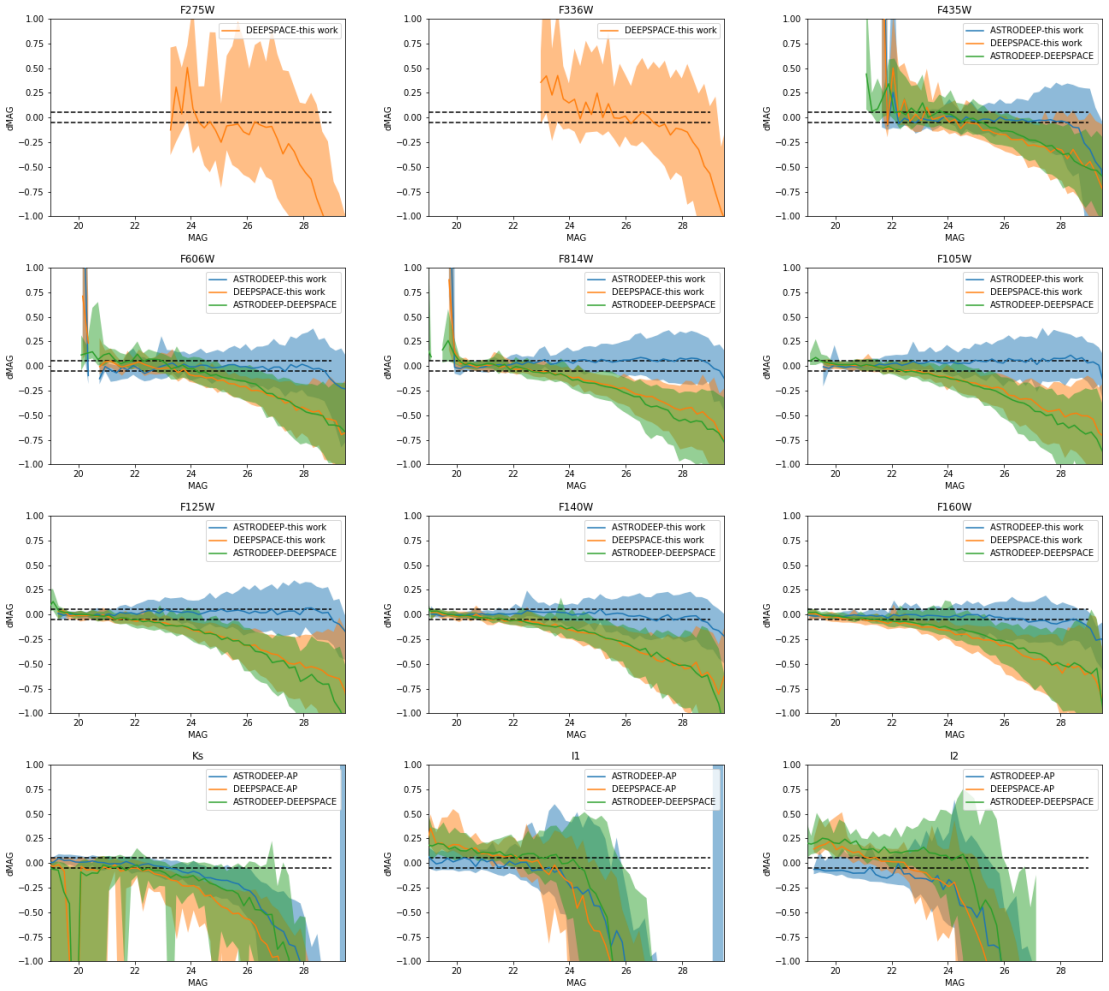

Figure 2.17: Comparison of our extracted photometry with that of the existing data produced by the ASTRODEEP and DEEPSPACE teams. Shown are the Δmag where data exists for cluster-only photometry in each band. The black dashed lines represent magnitude offsets of ± 0.05. The solid lines represent the running median and the shaded region represents the interquartile range of those measurements.

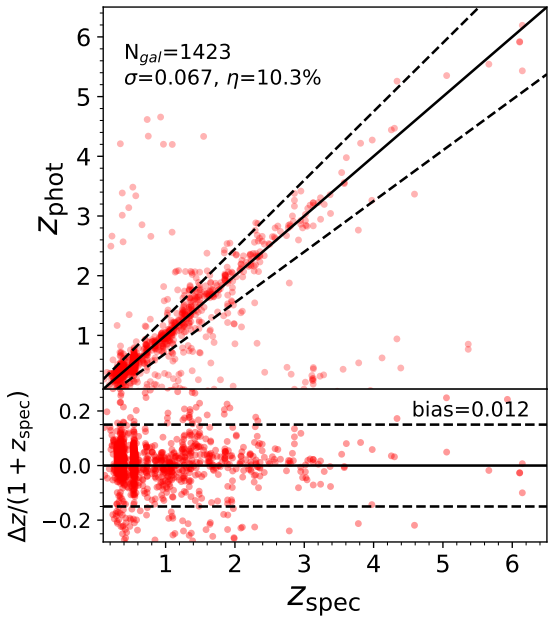

Figure 2.18: Assessing the quality of photometric redshifts estimated through SED fitting. *Upper panel:* $z_{\rm phot}$ vs. $z_{\rm spec}$ comparison. Red dots are 1,423 spectroscopic redshifts with $16 < F160W < 26$, the solid line shows the 1:1 relationship, and the dashed lines encloses the $z_{\rm phot} = z_{\rm spec} \pm 0.15(1+z_{\rm spec})$ threshold used to identify outliers (i.e., catastrophic errors). NMAD scatter (σ) and outlier fraction (η) are reported on the top-left corner. *Lower panel:* $\Delta z \equiv z_{\rm phot} - z_{\rm spec}$ scatter (red dots are spectrosopic objects) with the median bias indicated by a solid line; dashed lines represent the threshold for catastrophic errors as in the upper panel. See Figure 2.19 for detailed performance in each individual cluster.

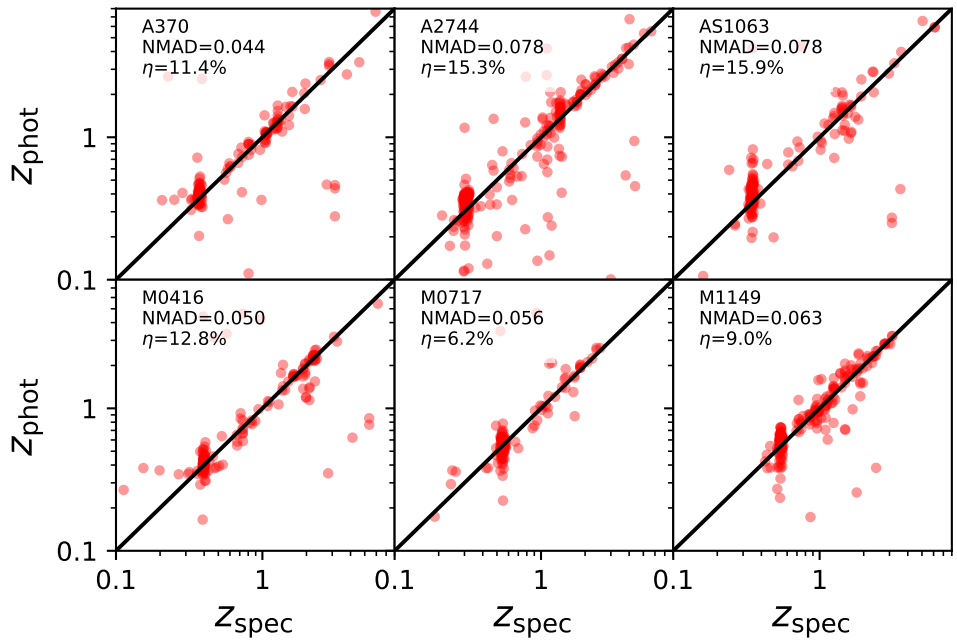

Figure 2.19: Comparison between $z_{\rm phot}$ and $z_{\rm spec}$ using the most reliable spectroscopic redshift (quality flag equal to 4).

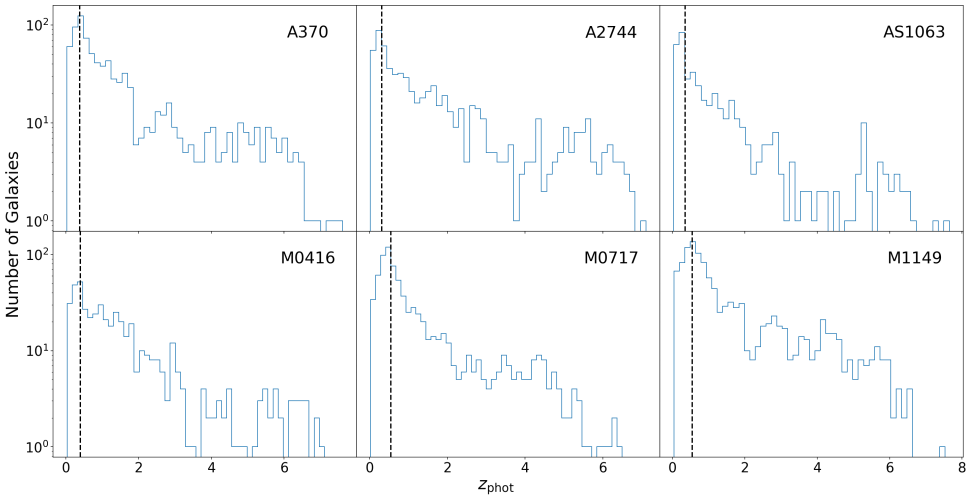

Figure 2.20: Histogram of the photometric redshift distributions for individual clusters. The black dashed line corresponds to the redshift of the cluster. Objects selected have SED fits with a reduced $\chi^2 < 10$

Chapter 3

Photometric catalogs of the BUFFALO *HST* survey and overlapping Spitzer and K-band imaging

This chapter presents new astronomical source catalogs using data from the BUFFALO Survey. These catalogs contain detailed information for over 100,000 astronomical sources in the 6 BUFFALO clusters: Abell 370, Abell 2744, Abell S1063, MACS 0416, MACS 0717, and MACS 1149 spanning a total 240 arcmin^2. The catalogs include positions and forced photometry measurements of these objects in the F435W, F606W, F814W, F105W, F125W, F140W, and F160W *HST*-bands, Keck-NIRC2/VLT-HAWKI Ks band, and IRAC Channel 1 and 2 bands. Additionally, we include photometry measurements in the F475W,

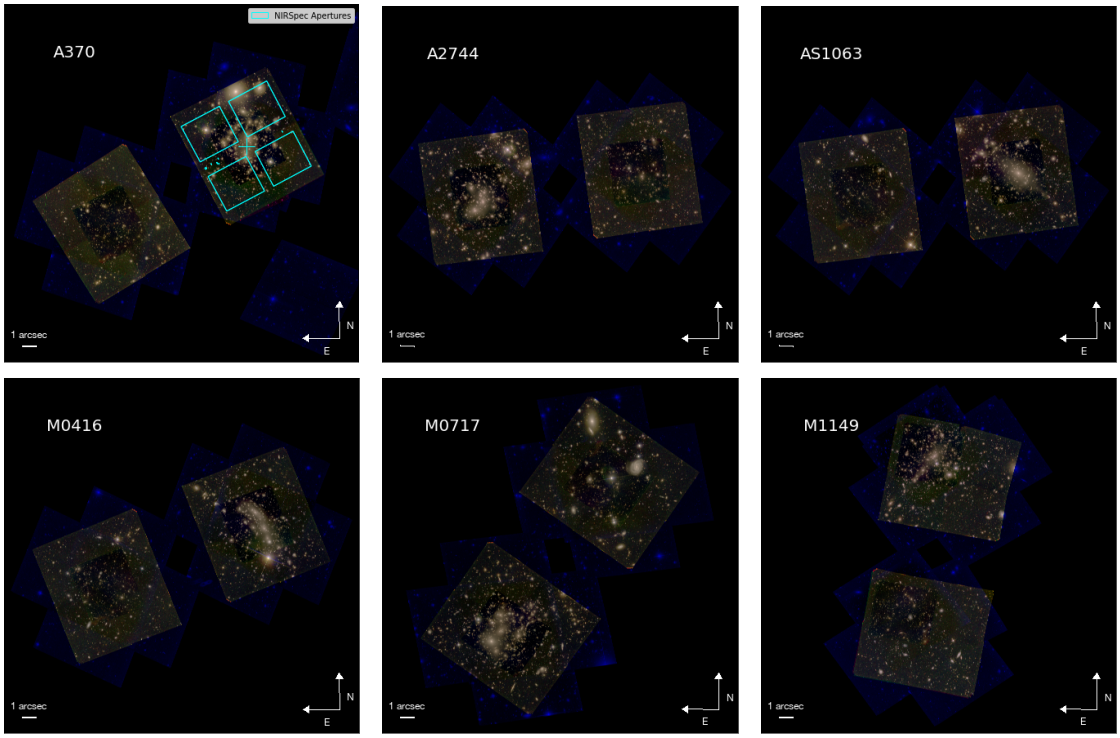

Figure 3.1: BUFFALO cluster footprints analyzed in this work. Color images created using `trilogy` [34], using F160W as the red channel, F105W as the green channel, and F814W as the blue channel. Note that due to the larger area coverage of F814W (ACS) compared to other bands (WFC3), certain areas of the footprint appear as blue. In the top left panel, we include the NIRSpec apertures for reference.

F625W, and F110W bands for Abell 370. This catalog includes photometric redshift estimates using LePhare, and contains ~ 1400 high-redshift ($z > 6$) sources detected with a signal-to-noise ratio larger than 5 in F160W, of which > 500 have high-confidence redshift estimates $\chi^2/\mathrm{ndof} < 1.5$.

3.1 Introduction

The Hubble Frontier Fields (HFF) [95] is a multi-waveband program obtaining deep imaging observations of six massive clusters in a narrow redshift range $z \sim 0.308$

- 0.545. Combining the sensitivity, resolution power and multi-wavelength capability of the Hubble Space Telescope (*HST*), with the gravitational lensing effect introduced by the massive galaxy clusters selected for this study, one can reach unprecedented depths. Two *HST* instruments, the Advanced Camera for Surveys (ACS) and Wide-Field Camera 3 (WFC3), were used in parallel to simultaneously observe each cluster and its parallel field. The parallel fields separated by ~ 6 arcmin from the cluster core, corresponding to > 1.8 projected co-moving Mpc for a $z > 0.3$ cluster. The six parallel fields are comparable in depth to the Hubble Ultra Deep Field [HUDF, 18], corresponding to m(AB) $\sim$ 29 mag. The area coverage and depth of the parallel fields provide significant improvement in the volume covered and statistics of faint galaxies.

The aims of the HFF observations were: (1) leverage gravitational lensing due to massive clusters to magnify fluxes and hence detect very faint background galaxies at $z \sim 5$ - 10 [132, 22, and references therein]; [see 82, for a review]. These galaxies are $\sim$ 10 times fainter than any galaxy known at the time [47]; (2) study the stellar population of these faint galaxies at high redshifts and constrain the mass function of galaxies at early epochs [e.g. 50, Weaver et al 2022 in prep, Ilbert 2022 in press]; (3) study of the morphology and other observable properties of lensed galaxies at $z > 8$ using a statistically large sample.

The Beyond Ultra-deep Frontier Fields and Legacy Observations (BUFFALO) is an *HST* treasury program with 101 prime orbits (and 101 parallel orbits) (GO-15117; PIs: Steinhardt and Jauzac), covering the immediate areas around the HFF clusters where deep Spitzer (IRAC channels 1 and 2) and multi-waveband coverage already exist [137]. The BUFFALO extends the area of each of the six HFF clusters by three to four times.

Observing these fields in five filters (ACS: F606W, F814W and WFC3: F105W, F125W and F160W), BUFFALO provides a factor of 2 improvement in the statistics of high redshift galaxies, improves the cosmic variance and allows a more accurate modeling of the dark matter distribution in the foreground clusters. The *HST* and Spitzer data for BUFFALO, combined with ground-based observations [26, KIFF] will expand the HFF to sufficiently large area allowing a statistically large number of spectroscopic targets for the James Webb Space Telescope NIRSpec observations without the need for *JWST*/NIRCam pre-imaging. The program significantly improves the statistics of galaxies in the outskirts of clusters and field samples. Finally, it constrains distribution of dark matter measured from gravitational lensing effects.

In this paper we present photometric and redshift catalogs for the BUFFALO galaxies. In section 2, we present the data used in this study. In section 3, we briefly outline the data reduction process, referring the reader to [115] for a more detailed description. In section 4, we describe our photometric validation procedure. Section 5, details the data products and results. Section 6 describes the photometric redshifts extracted. Finally, we conclude this study in section 7.

Throughout this paper we assume standard cosmology with $\Omega_M = 0.23$, $\Omega_\Lambda = 0.76$ and $H_0 = 73$ Km/sec/Mpc. Magnitudes are in the AB system.

3.2 The data

We provide a brief summary of the dataset in the following sections. We refer the reader to the BUFFALO overview paper [137] for more details.

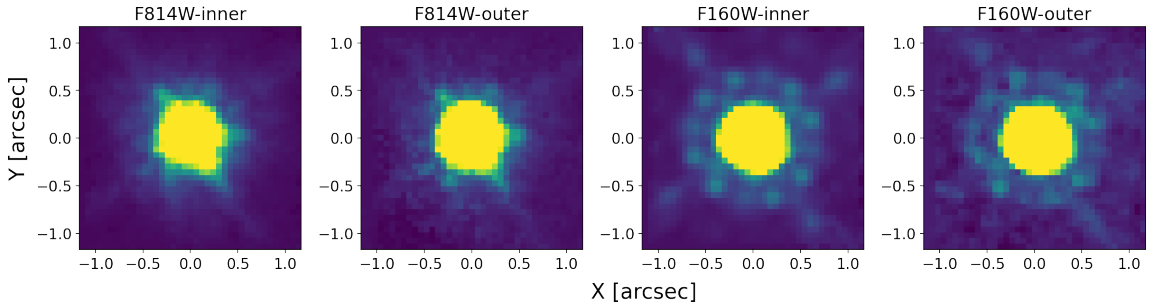

Figure 3.2: Representative examples of PSF for the instruments used in this study, corresponding to a 0.06"/pixel scale normalized with the ZScale algorithm. From left to right, panels show ACS-F814W (inner region), ACS-F814W (outer region), WFC3-F160W (inner region), WFC3-F160W (outer region). See Section 3.1 for more details

3.2.1 *HST* observations

The BUFFALO images provide the deepest exposures of galaxy clusters by *HST*, only second to the HUDF with respect to depth. With 101 additional prime (and 101 parallel) orbits, they build on the existing HFF cluster and parallel field surveys. BUFFALO slightly increases the depth at the center of the HFF clusters while increasing their areal coverage three- to four fold. As a result, it expands the radial coverage of cluster outskirts, providing observations of the global mass distribution of clusters to almost the virial radius, i.e. $\sim 3/4 \times R_{vir}$. The coverage was chosen to increase discovery of z>7 galaxies and to reduce cosmic variance. Furthermore, BUFFALO's footprint is chosen to be is compatible with *JWST*'s NIRSpec field of view, allowing multiwavelength programs with *JWST* (Figure 3.1), which is especially timely for planning robust observations with *JWST*.

The gravitational potential of the clusters' halo, besides binding together the galaxies in the system, produces a lensing magnification that could detect background objects to an *intrinsic* brightness of 30–33 mag, i.e. 10–100 times fainter than previous surveys.

Details of the BUFFALO survey design are provided in [137]. In Table 2.1 we report the main characteristics of the six clusters, with a summary of the ancillary observations in Table 2.3. We use mosaics that have been reduced by the BUFFALO team, with a pixel scale of 0.06"/pix. These images were reduced using the *HST* science data products pipeline [83].

3.2.2 Ancillary data

The large wealth of complementary legacy datasets and programs for the HFF clusters has contributed to its success. The *Spitzer* Space Telescope dedicated more than 1,000 hours of Director's Discretionary time to obtain IRAC 3.6 μm (channel 1) and 4.6 μm (channel 2) imaging down to the depths of 26.5 and 26.0 mag., in cluster and parallel fields respectively (program IDs: Abell 2744: 83, 90275; MACS J0416.1-2403: 80168, 90258; MACS J0717.4+3745: 40652, 60034, 90009, 90259; MACS J1149.4+2223: 60034, 90009, 90260; Abell S1063 (RXC J2248.7-4431): 83, 10170, 60034; Abell 370: 137, 10171, 60034). These observations are especially important for redshift determination, given that they help break the degeneracies between low-redshift interlopers and high-redshift galaxies, and are beneficial in constraining galaxy properties since they provide a good proxy for galaxy stellar mass.

The HFF clusters in the southern sky are also covered in the *Ks* band using the High Acuity Wide Field K-band Imager (HAWK-I) [KIFF 26] at the Very Large Telescope (VLT), reaching a depth of 26.0 mag (5σ, point-like sources) for Abell 2744, MACS-0416, Abell S1063, and Abell 370 clusters. In the northern sky, this campaign used the Multi-Object Spectrometer for Infrared Exploration (MOSFIRE) at Keck to observe MACS-0717 and MACS-1149 to a K-band 5σ depth of 25.5 and 25.1 mag respectively. This data covers

Table 3.1. The Point Spread Function radius and effective wavelengths for different photometric bands used for the BUFFALO fields.

Band	$FWHM$	$\lambda_{\rm pivot}$ (Å)
F435W	013	4329
F606W	011	5922
F814W	010	8045
F105W	020	10551
F125W	020	12486
F140W	020	13923
F160W	020	15369
Ks	036	21524
I1	129	35634
I2	142	45110

Note. — Values were calculated for the Abell 370 cluster.

all of the cluster and parallel field centers, but not the entirety of the outer area observed by BUFFALO. Table 2.3 summarizes the available ancillary data.

3.3 Data processing

The workflow followed for the data processing in this work is the same as the one in [115] (P21 hereafter). The main steps taken to obtain the data products presented here are summarized as follows:

i. Error map correction: we compare the standard deviation of the values of the background pixels in the science image, to the reported root mean-square (rms) values as given by the error maps, and correct the latter so that the mean ratio in the

background pixels are equal to 1.

ii. PSF extraction: Select unsaturated, unblended stars and perform median stacking to obtain an estimate of the PSF.

iii. Intracluster light (ICL) + bright galaxy modeling: Perform multi-object fits to Sérsic profiles, plus a local background using a combination of `GALFIT` [118] and `GALAPAGOS-M` [60].

iv. Bright galaxy photometry: Run SOURCE EXTRACTOR [20] on *HST* bands PSF-matched to the reddest, F160W, band, and obtain photometric measurements.

v. Background galaxy photometry: Subtract bright galaxies and ICL and run SOURCE EXTRACTOR on the "cleaned" field for the PSF-matched *HST* images.

vi. Spitzer and K-band photometry: Use T-PHOT [106] to obtain photometry measurements on the Spitzer and K-band images, using the *HST* images and segmentation map as priors.

vii. Synthetic source injection: Inject synthetic sources and repeat the process to validate and correct the photometric measurements.

viii. Estimate photometric redshifts: The last step consists on using LEPHARE [7, 67] to obtain photometric redshift estimates of detected astronomical sources in these catalogs.

In the following subsections some of these steps are described in more detail. However, for a detailed description of all of the steps, we refer the reader to P21.

3.3.1 Point Spread Function

A well-defined point spread function (PSF) as a function of wavelength is crucial to perform consistent photometry within a 'panchromatic' baseline to correctly model galaxies and obtain galaxy fluxes in PSF-matched images. In order to perform multi-waveband photometry with accurate signal-to-noise and resolution for each aperture, we convolve images with a kernel generated by taking (in Fourier space) the ratio between their original and target PSFs, to match that of the reddest F160W PSF. In order to generate the PSFs for the *HST* and K-band images, we stack isolated and unsaturated stars in each individual image, taking the median of the stack. Up to this point, the procedure is identical to that followed in P21. We improve upon our previous work by creating PSFs for the representative inner (deeper) and outer (shallower) regions in both the cluster- and parallel-fields. Figure 3.2 shows examples of the stacked PSFs derived in different regions and Table 3.2.2 gives the representative FWHM as a function of wavelength. We note that the full-width-half-max (FWHM) in both regions are compatible.

Due to large spatial variations of the PSF in the mid-IR *Spitzer* channels [1], we do not use the same approach to create our *Spitzer* PSF model. Furthermore, the individual pixel response functions (PRFs) are asymmetric and are thus dependent on the orientation of the camera. Moreover, the pixels on IRAC Ch 1 and 2 tend to under sample the PRF. Thus, instead of stacking stars and generating a single PSF per field, we use a synthetic pixel response function (PRF) that combines the information on the PSF, the detector sampling, and the intrapixel sensitivity variation in response to a point-like source, as done in P21.

[1] See https://irsa.ipac.caltech.edu/data/Spitzer/docs/irac/calibrationfiles/psfprf/ the *Spitzer*/IRAC handbook

A PRF model for a given position on the IRAC mosaic is generated by the code `PRFMap` (A. Faisst, private communication) by combining the single-epoch frames that contribute to that mosaic. To do so, `PRFMap` stacks individual PRF models with the same orientation of the frames, resulting in a realistic, spatially-dependent PSF model.

3.3.2 Modeling the intra-cluster light

The deep potential well and high density of galaxy clusters make them rich laboratories to study galaxy dynamics and interactions. Due to these complex processes, stars and gas stripped from their constituent galaxies build up in the cluster core as intracluster light (ICL) [see 111, for a review]. This can bias the flux measurements of galaxies close in angular space to the cluster center. Following [113] and P21, in order to model the ICL in the BUFFALO clusters, we first generate 18×18 arcsecond (300×300 pixel) stamps centered in each galaxy with a magnitude brighter than 26 in each image/band. Using `GALFIT` [118], we fit all of the galaxies in each stamp with a single Sérsic profile, masking those that are fainter than magnitude 26. In case a given pixel with coordinates (x, y) is only included in one cutout, the ICL emission ($F_{\rm ICL}$) is defined as the local background measurement as reported by `GALFIT` (namely, the `sky value` parameter). If there are overlapping cutouts in (x, y), we use the inverse χ^2-weighted mean of their background measurements:

$$F_{\rm ICL}(x,y) = \frac{\Sigma_i s_i(x,y)/\chi_i^2(x,y)}{\Sigma_i 1/\chi_i^2(x,y)} \ , \tag{3.1}$$

where s_i and χ_i^2 are the `sky fit` (fit value to the local background of the postage stamp) and goodness-of-fit values from `GALFIT` for the i-th cutout.

As described in P21, the resulting ICL map has unphysical sharp features, which are smoothed out using a Gaussian kernel whose $\sigma = 4.32$".

Similarly, for the K_s and *Spitzer* bands, we use `T-PHOT` to obtain the local background for each measured source, which is then merged into a single mosaic, and smoothed with a representative kernel.

As a caveat, though these maps primarily contain ICL emission, they also contain inhomogeneities in the background. This ensures a robust 'background+ICL subtraction" in the individual images. Cleaning of these maps via color selection of the individual stamps will be performed in following work.

3.3.3 Modeling the brightest galaxies

The procedure to model bright galaxies (magnitude brighter than 19) is also unchanged from P21. We rely on GALAPAGOS-M [60] to fit Sérsic profiles simultaneously to galaxies in all bands, with the fitting parameters varying as a function of wavelength. The results of the ICL and bright galaxy modeling and subtraction are illustrated in Figure 3.3.

Finally, we apply a median filter to the ICL+bright galaxy subtracted images. We use a filter with a box size of 1° per side, applied only to pixels within 1σ of the background level to reduce the effects of over-subtraction in the residual. Figure 3.3 shows the modeling and filtering process. The lower right panel shows the effect of median filtering. Note that this process does not affect the outskirts of the cluster.

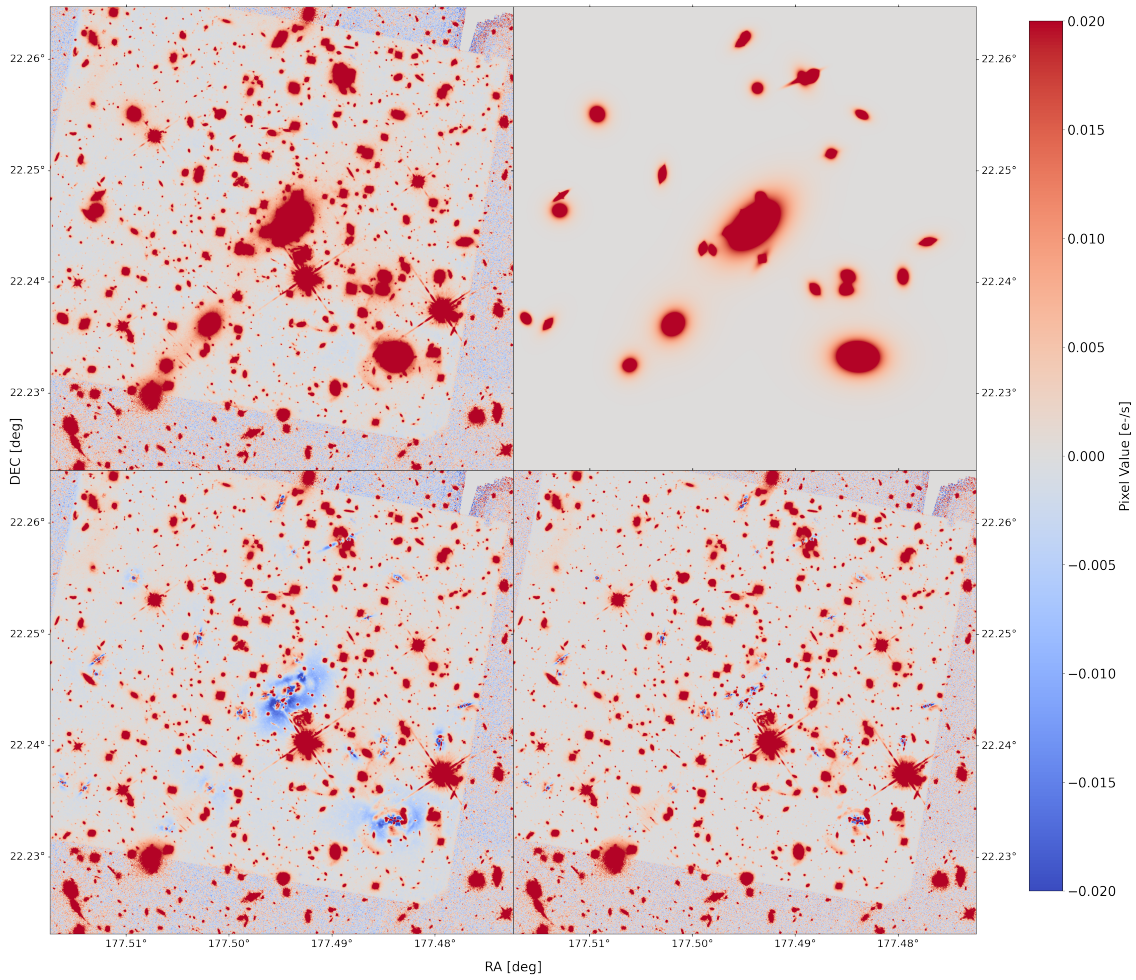

Figure 3.3: Steps in bright cluster + ICL modelling (in this case for cluster MACS 1149) for the F160W band. Upper panels show the original image (left) and the galaxy/ICL models (right). Lower panels show the residual image before and after median filtering (left- and right-hand panel respectively). The colorbar denotes the pixel intensity in counts/s. See Sections from 3.2 to 3.3 for more details

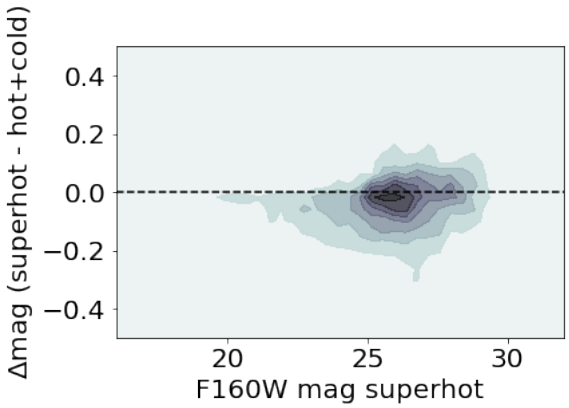

Figure 3.4: Magnitude comparison between "hot+cold" mode as described in P21, and the "super hot" mode used in this work. Note, the magnitude difference is primarily within 0.05 mags.

3.3.4 Source Extraction

To perform detection and measurement of astronomical sources run SOURCE EXTRACTOR, focusing only on a "super hot" mode, rather than creating a dual run with hot and cold modes. This is one of the main differences with the procedure presented in P21 where a second "cold" mode `Source Extractor` run is performed. We find that this second run does not have a significant impact on the detection nor photometric performance, especially after bright galaxy and ICL subtraction. This is a consequence of the cold mode focusing on extracting information about the brightest objects, which have already been removed by the bright galaxy subtraction. This is illustrated in Figure 3.4, where we compare a dual run with our new "super hot" run, finding similar magnitudes for the BUFFALO Abell 370 cluster.

We also show the magnitude distribution of sources in the F160W band for all clusters in Figure 3.5. The large number density (defined as the number of sources divided

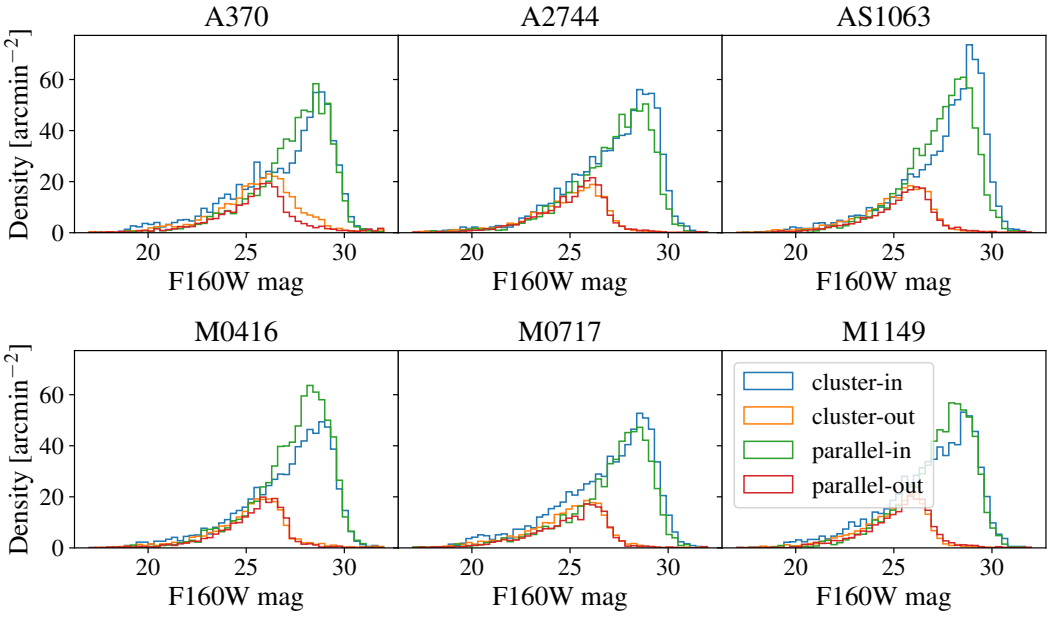

Figure 3.5: Magnitude distributions for sources in the BUFFALO catalogs across all clusters. We subdivide each of the catalogs, one per cluster and per parallel/infall field, into inner (in) and outer (out) regions, which correspond to different depth regimes.

per square arcmin) and depth of these catalogs. We subdivided the catalogs into sources detected in the inner field regions (the overlap with HFF), which reaches to significant depth, and the outer regions (the extension), where the depth is noticeably lower. In general, we find similar densities to those found in previous works [106, 136, 24, 115]. The differences between the distributions of the cluster and the parallel regions is apparent. The cluster regions typically contain an over-abundance of brighter galaxies, whereas the parallel fields contain less of these bright objects but reach slightly deeper levels.

3.3.5 Photometry in Ancillary images

Because the *Ks* and *Spitzer* images have lower angular resolution than the *HST* images, they are more affected by blending. In order to effectively deblend sources and

maximize the information extracted in each image, we use T-PHOT as in P21 to perform forced photometry in the Ks- and IRAC images on sources detected in the IR-Weighted *HST* image. T-PHOT [106] is a software that uses priors from high resolution data in order to deblend and extract fluxes of the same objects in a lower resolution image. We first use T-PHOT's built-in background routine to generate a local background for each source and remove the excess ICL light as well as inhomogenieties in the backgrounds. Then, as "real" galaxy priors, we use the IR-Weighted segmentation map and flux measurements from the F160W-band image. Additionally, we use the galaxy models that have been created in the bright galaxy+ICL removal step as the "model" priors. Given the spatial variation of the PRF in the IRAC bands, we take advantage of T-PHOT's "multikernel" option, and use a separate PRF to model sources at each position. We emphaize that the flux (FitQty) that is provided by T-PHOT corresponds to the total flux emitted by a given source.

3.4 Photometric validation

In order to characterize the performance of our detection and measurement procedures, we proceed as in P21 injecting synthetic galaxies in the original BUFFALO images using `GalSim` [126] to render noiseless realistic galaxies via the `RealGalaxy` class following the morphology measurements in *COSMOS* by [93]. This catalog only contains information for fluxes in the F814W band. Thus, we match these sources to the COSMOS catalog [90] in order to obtain the fluxes in the rest of our bands of interest. We choose to keep the morphology and centroids fixed across bands in order to simplify data handling and bookkeeping. In this case, we generate 10 realizations of a set of 160 sources using the F160W

image footprint as reference. Note that, since not all bands cover the same footprint, some sources will not be recovered after processing. We then insert these sources in the original images, run our pipeline on the resulting combined image (which is the sum of the original and the noiseless synthetic sources) and compare their measured fluxes and positions to their inputs.

This provides valuable information about completeness and absolute zeropoint calibration. The two catalogs are matched using a nearest neighbor matching routine, `match_coordinates_sky`, included in the `astropy` package [9, 8]. The results of this comparison are shown in Figure 3.6. We see that for all of the *HST* bands (F435W, F606W, F814W, F105W, F125W, F140W, F160W) the recovered magnitude is within 20 mmags of the input, and that the reconstruction of the fluxes is relatively stable across the considered range of magnitudes. We note that at the bright end, there is a small fraction of the flux missing, probably due to the extended tails of the sources not being captured by the aperture. This photometric bias becomes smaller with increasing magnitude up to the point where we start to lose sensitivity. We use these offsets to robustly correct the fluxes in each band. For Ks the performance is also excellent and we find a median value of $\Delta\text{mag} = -0.05\text{mag}$. For the Spitzer IRAC channels, we find a small photometric offset $\Delta\text{mag} = -0.12$ and $\Delta\text{mag} = -0.13$ for I1 and I2, respectively.

We compare the mean uncertainty reported by the measurement pipeline to the standard deviation of Δmag as a function of magnitude. Again, for the *HST* bands the performance is excellent, and we find that the reported errors are in good agreement with the scatter measured using our synthetic sources. This is not the case for Ks nor IRAC,

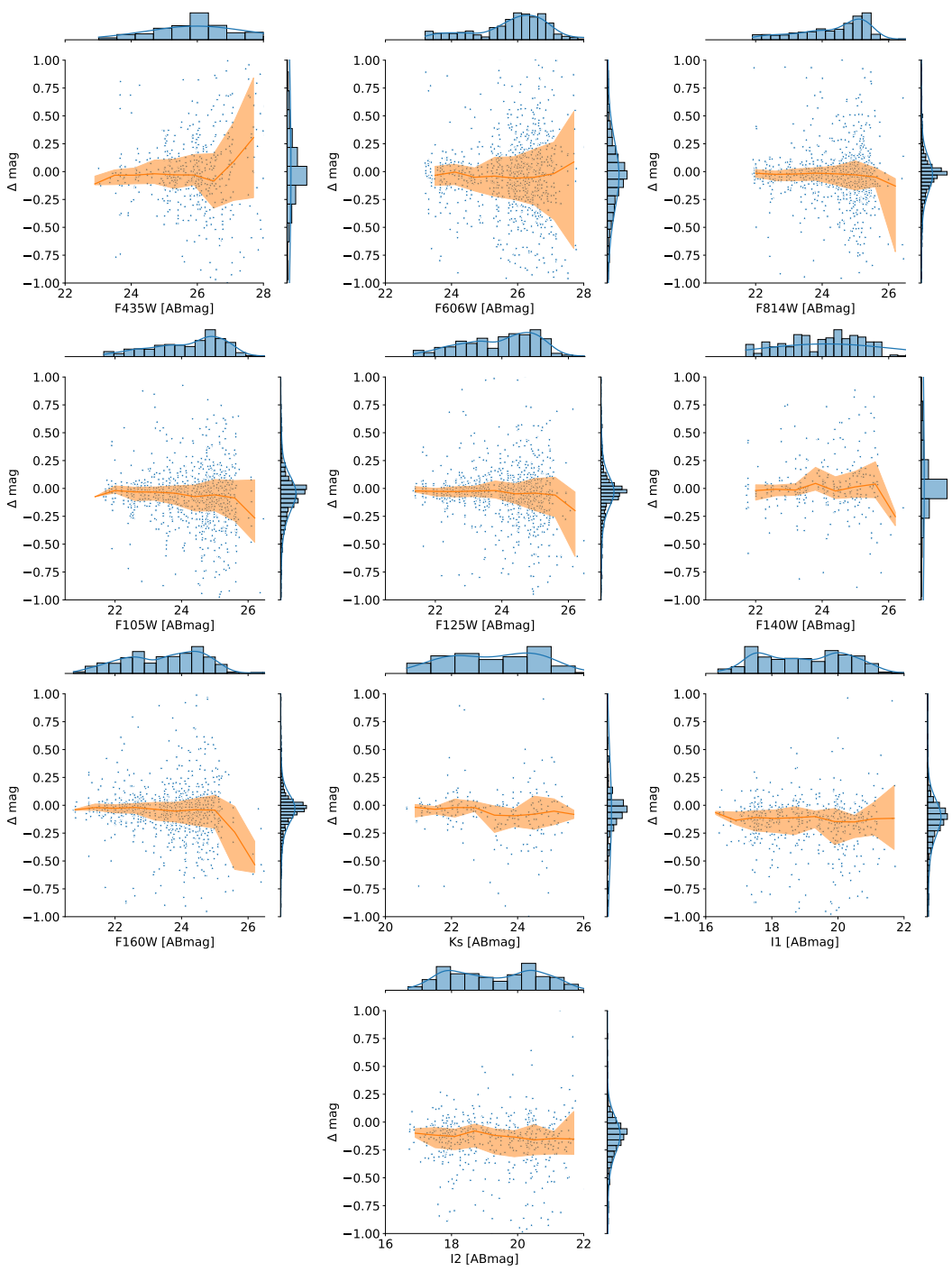

Figure 3.6: Photometric validation of BUFFALO catalogs. Scatter plot of $\Delta\text{mag} = \text{mag}_{\text{in}} - \text{mag}_{\text{out}}$ as a function of the input magnitude for the different bands considered in this work. The solid line shows the rolling mean magnitude offset and the shaded area corresponds to the inter-quartile range. Additionally, each panel includes the input magnitude histogram (top horizontal histogram) as well as the Δmag histogram (right vertical histogram).

where we find that a correction is needed. In particular, we use a power-law correction:

$$\Delta F_{new} = \Delta F_{old} A F^{B}, \tag{3.2}$$

where ΔF_{new} is the corrected uncertainty estimate, ΔF_{old} is the reported uncertainty by the measurement software, F is the reported flux, and A, B are free parameters. We fit A, B and tabulate the results in Table 3.2.

Band	A [counts/s]$^{-1}$	B
Ks	2.05	0.26
I1	164.67	0.44
I2	123.14	0.43

Table 3.2: Best-fit coefficients used to perform the uncertainty correction as a function of flux.

3.5 Data products and results

In this section we discuss the data products from this work and present some validation results. We produce several new data products from the BUFFALO, including: catalogs, models for the point spread function, and models for the ICL and bright galaxies. The final catalogs include properties of >100,000 sources in the 6 BUFFALO Frontier Fields cluster and parallel fields, and extend the Frontier Fields footprint, covering a total of ~ 240 square-arcminutes. These include positions, photometry, and photometric redshift estimates for the sources detected as provided by LePhare [7, 67].

Point spread function (PSF) estimates are provided as as FITS images. Sec-

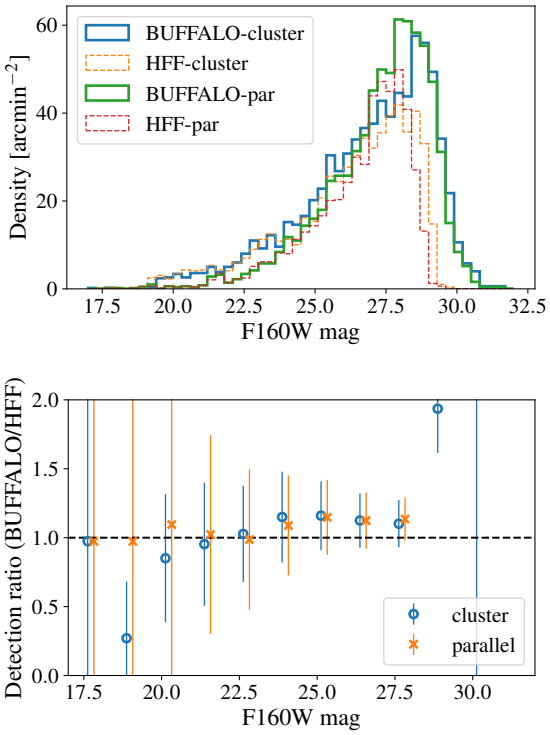

Figure 3.7: **Top panel:** Comparison of magnitude distribution in the F160W band between BUFFALO sources (solid lines) and HFF (broken lines) for both the cluster and parallel (par) fields in the deepest part of the images for MACS 1149. **Bottom panel:** Ratio between the histograms in the top panel for the cluster field (blue open circles) and parallel field (orange crosses). Other fields show similar behavior

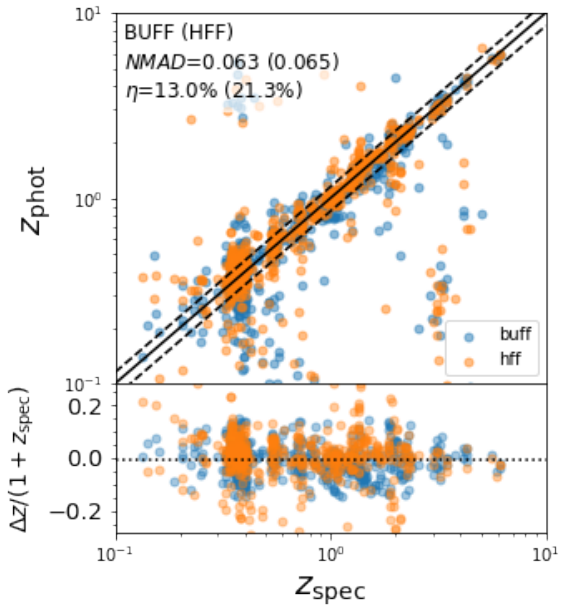

Figure 3.8: Comparing the quality of photometric redshifts estimated through SED fitting of overlapping galaxies in the HFF and BUFFALO. Blue points correspond to BUFFALO measurements and orange points correspond to HFF measurements. Upper panel: zphot vs. zspec comparison. Blue and orange points are spectroscopic redshifts with 17 ¡ F 160W ¡ 27 selected in the BUFFALO sample, the solid line shows the 1:1 relationship, and the dashed lines encloses the zphot = zspec±0.15(1+zspec) threshold used to identify outliers (i.e., catastrophic errors). NMAD scatter (σ) and outlier fraction (η) are reported on the top-left corner. Lower panel: $\Delta z \equiv$ zphot − zspec scatter (red dots are spectroscopic objects) with the median bias indicated by a solid line; dashed lines represent the threshold for catastrophic errors as in the upper panel.

tion 3.3.1 describes the modeling of the PSFs. We summarize some of their properties in table 3.2.2. Unsurprisingly, these results are very similar to those found by P21, as the BUFFALO fields are mostly extensions of the HFF.

The procedure to obtain models for the ICL and bright galaxies is described in Section 3.3.3. These models are also available as FITS images.

3.5.1 Photometric redshifts

In this section we present our redshift estimates based on the photometric measurements presented in previous sections. We run LePhare [7], LePhare2006, a template-based code that derives a redshift likelihood function for each source. As in P21, the fluxes used as inputs to LePhare are rescaled by a factor:

$$f_{\rm tot} = \frac{\sum_i w_i (\text{FLUX\_AUTO}/\text{FLUX\_ISO})_i}{\sum_i w_i}, \tag{3.3}$$

i.e. the weighted mean of the AUTO-to-ISO flux ratio summed over the observed *HST* bands, where the weights, w_i, are the sum in quadrature of the Source Extractor errors: $w_i = \sqrt{\sigma^2_{i,\rm AUTO} + \sigma^2_{i,\rm ISO}}$. This is done in order to improve the accuracy of the colors. For the `TPHOT`-based photometry (Ks, and IRAC bands), as we do not have an equivalent to FLUX_ISO, we include our baseline fluxes. The template library, and dust attenuation follows [89], using [122] or [31] extinction laws depending on the galaxy type. For details about the templates and the extinction prescriptions we refer the reader to [89] and P21. In our catalog the redshift estimates, `ZPDF`, correspond to the position of the maximum-likelihood for each object.

Table 3.3. Multiplicative factors applied to each band in the photo-z calibration step.

Band	Multiplicative Factor
F435W	1.09
F475W	1.05
F606W	1.01
F625W	1.00
F814W	1.00
F105W	1.01
F110W	1.00
F125W	1.00
F140W	1.00
F160W	1.00
Ks	0.87
IRAC1	1.14
IRAC2	1.21

The redshift calibration procedure is similar to that presented in P21, which is based on spectroscopic data described in [114, 45, 124, 12, 140, 131, 88, 97, 87]. We obtain the best-fit template for each source and try to find a systematic offset in each band by comparing the predicted and observed flux for all sources that have a measured spectroscopic redshift with a spectroscopic quality flag > 3. These magnitude offsets, when applied to the photometric baseline, compensate for a possible bias in the template library and/or for calibration issues in data reduction. We find these corrections to be below 10% for all the *HST* bands. For $K_{\rm s}$ we find a correction of 0.87 while in the IRAC channels 1 and 2 the correction is a factor 1.14 and 1.2, respectively. These corrections are shown in Table 3.5.1.

3.6 Comparison with the Hubble Frontier Fields

By design, there is significant overlap between the HFF and the BUFFALO fields. This makes the HFF catalogs an exceptional reference to verify and validate the data presented in this work and to check for potential improvements, given the increased number of exposures. Here, we compare our BUFFALO data products with those presented in P21.

Figure 3.7 compares the magnitude distribution of sources in the F160W band between the catalog presented here and the catalogs in P21 in the overlapping region of the MACS 1149 band. It is clear that our new BUFFALO catalogs reach fainter sources than those from HFF. We also show the fraction of detected objects as a function of magnitude, showing that both catalogs have a similar completeness to magnitude ~ 27.5 in the F160W band. This is in agreement with P21, where the completeness dropped below 100% at ~ 27.5. Other bands and clusters show a similar behavior.

We also compare the photometric redshift performance of overlapping sources in the two catalogs. We subselect for objects which are observed in 5 or more bands, $17<\mathrm{mag}_{F160W}<27$, and which have a spectroscopic redshift flag of 4 (the highest quality flag). We find that the photometric redshifts in the BUFFALO catalog have a smaller outlier fraction (13.0% compared to 21.3%), as well as a marginally smaller spread (0.063 compared to 0.065) than the HFF catalogs, as shown in Figure 3.8.

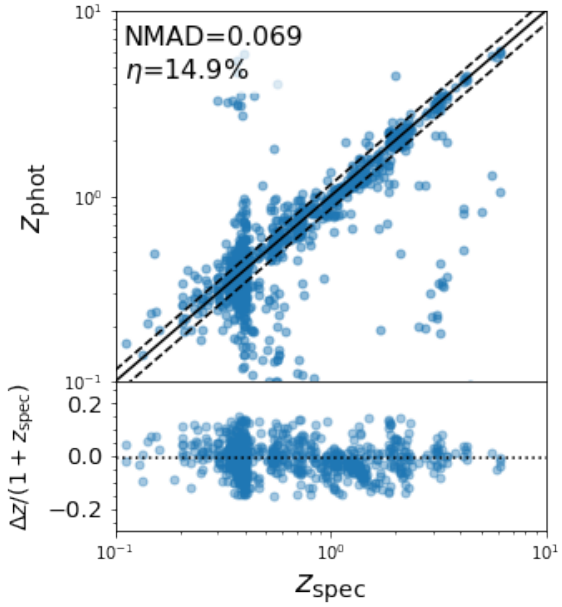

Figure 3.9: Assessing the quality of photometric redshifts estimated through SED fitting. Upper panel: zphot vs. zspec comparison. Blue points are spectroscopic redshifts with 17 $<$ F 160W $<$ 27, the solid line shows the 1:1 relationship, and the dashed lines encloses the zphot = zspec$\pm$0.15(1+zspec) threshold used to identify outliers (i.e., catastrophic errors). NMAD scatter (σ) and outlier fraction (η) are reported on the top-left corner. Lower panel: Δz $\equiv$ zphot $-$ zspec scatter (red dots are spectroscopic objects) with the median bias indicated by a solid line; dashed lines represent the threshold for catastrophic errors as in the upper panel.

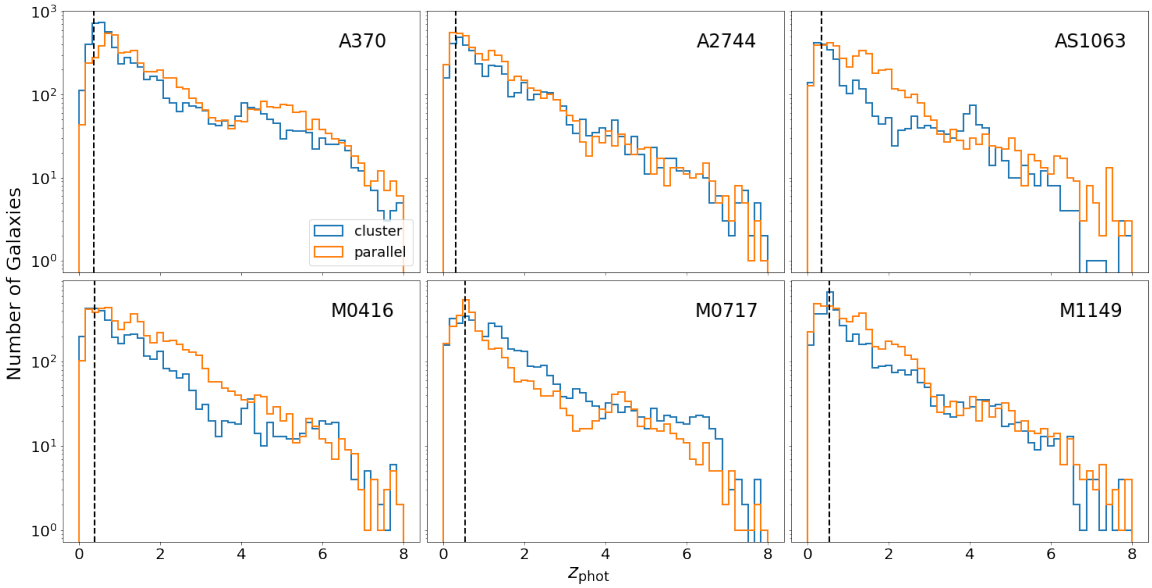

Figure 3.10: Redshift histograms for each cluster field. Dotted line corresponds to the redshift of the cluster. Sources were chosen with mag$AB_{F160W} < 28.5$ and $\chi^2/\text{ndof} < 5$.

3.7 Summary

The wealth of deep (*HST*) observations and ancillary data in the HFF [95], open a window to the high-redshift universe, and get a taste of what data from the James Webb Space Telescope (*JWST*) can unveil. The BUFFALO survey [137] used these data and extended the observations in the 6 HFFs, to allow for *JWST* spectroscopic measurements without the need of *JWST* imaging. This work presents a new set of data products based on the BUFFALO observations. The data products include models for the point spread function (PSF), intra-cluster light (ICL), the bright galaxies, and catalogs of astronomical sources. The catalogs contain detailed information (including positions and photometry) of over 100,000 sources distributed across 6 separate fields covering a total area of 240 arcmin^2.

The data products are obtained using a similar procedure to that outlined in [115]: First a model of the bright galaxies, and the ICL are created. These models are then sub-

tracted from the original image, in order to increase our sensitivity allowing us to observe fainter sources, which are detected and measured using SOURCE EXTRACTOR in the *HST* bands. We then use the IR-weighted segmentation map as priors in the T-PHOT package to obtain forced-photometry in ancillary data from Keck Ks band, and Spitzer IRAC channels 1 and 2. The photometric measurements are validated using synthetic source injection. Finally, LEPHARE is run to obtain redshift estimates based on our photometric measurements. The main change with respect to the procedure in P21 is the usage of a "super hot" mode Source Extractor run, that simplifies bookkeping, while not biasing the photometric estimates.

The data products presented in this work will be made publicly available to the astronomical community.

Chapter 4

First measurement of the 2-point correlation function of galaxies at $z > 6$ in BUFFALO cluster Abell 370

4.1 Introduction

Observations of the Large-scale structure (LSS) of the Universe have been continuously improving their sensitivity to the growth of structure. Recent experiments such as the Dark Energy Survey [DES, 48, 35, 1], the Kilo-Degree Survey [KiDS, 86, 61], the Hyper-Suprime Cam Subaru Strategic Program [2, 62], and the Extended Baryon Oscillations Spectroscopic Survey [eBOSS, 4] provided constraints of the growth of structure with

comparable sensitivity to those from observations of the cosmic microwave background (CMB), using ground observations of the late-time ($z < 2.5$) LSS. However, the estimates of the amplitude of matter fluctuations σ_8 appear to be in tension with the measurements from the CMB [62, 61, 4, 1]. Current and upcoming experiments such as the Dark Energy Spectroscopic Instrument [DESI, 38] Vera C. Rubin Observatory Legacy Survey of Space and Time [70, LSST,], and the Nancy Grace Roman Space Telescope [formerly known as WFIRST, 3] will clarify the origin of these tensions, by increased statistics and by exploring a larger redshift regime. However, measurements of the σ_8 parameter, in particular those using galaxy-clustering, are typically degenerate with the measurement of the so-called galaxy bias, b, which characterizes the relative clustering between galaxies and dark-matter at large-scales [76, 13, and references thereafter]. The bias parameter depends on the galaxy population details, redshift, and scale [for a review on galaxy bias see 39], but characterizing the large-scale galaxy bias at $z > 2$ sets an important point of reference for these surveys to extract their maximum potential. In such spirit, the work by [17] presented some initial measurements of the galaxy bias of high-redshift galaxies in the HSC data, selected using the dropout technique. As one of the deepest datasets to date, the BUFFALO HST survey data [138, 115, 51] opens a window to previously unexplored regimes. In this letter, we extend the redshift regime with a new set of two-point statistics, and derived galaxy biases are presented for the BUFFALO data.

This work is organized as follows: Section 4.2 describes the data products used for the analysis; section 4.3 introduces the theoretical framework and measurement process to obtain the results; section 4.4 presents the two-point statistics, and bias results. Finally,

section 4.5 presents some concluding remarks and discussion.

Throughout this work it is assumed a Flat ΛCDM cosmology with [119] cosmological parameters: $h = 0.674$, $\Omega_m = 0.3147, \sigma_8 = 0.8101$.

4.2 Data and sample selection

This study uses the new HST observations of the HFF cluster Abell 370 from the BUFFALO survey [138] which obtained new deep *Advanced Camera for Surveys* (ACS) data in the F606W and the F814W band and *Wide Field Camera Three* (WFC3) infrared (IR) data in the F105W, F125W and F160W bands around all six HFF clusters. We use the full BUFFALO mosaics of Abell 370 which include all existing HST data of the cluster and were produced using updated versions of the pipelines described in [84]. In addition to the new BUFFALO data, existing HST observations of Abell 370 also include the HFF mosaics in the F435W and the F140W bands as well as ancillary data sets in the F475W, F625W and F110W bands. While we use all of these in our analysis, note that only the five BUFFALO filters cover the full extended area around the cluster core and the HFF parallel field.

In addition to the HST data we have the deep *Spitzer Frontier Fields* [95] observations of Abell 370 at our disposal, the *Infrared Array Camera* [IRAC; 46] channel 1 (3.6) and channel 2 (4.5) mosaics of which are deep enough ($\sim$ 26 mag) to detect high-redshift galaxies and cover the whole BUFFALO field-of-view. We will hereafter refer to these bands as IRAC1 and IRAC2. Finally, while ground-based *Ks*-band (2.2) observations of Abell 370 obtained with the *High Acuity Wide-field K-band Imager* [HAWK-I; 81] on ESO's

Very Large Telescope (VLT) do exist [27], will not use them in our analysis as they do not cover the complete BUFFALO area.

Note that from here on we will refer to the deeper central region of the BUFFALO field-of-view [see Fig. 9 in 138], which corresponds to the HFF area, as the 'inner' field and to the shallower region corresponding to the new area observed with BUFFALO as the 'outer' field.

4.2.1 Photometry

Galaxies are detected in the entire BUFFALO mosaic, i.e. including the HFF area and the parallel field, using high-sensitivity methods for high-redshift galaxy detection in HST data developed for the HFF in [10, 11] and adapting them to the BUFFALO data. We use `SExtractor` [21] in dual mode to detect galaxies and measure photometry with three different detection images: A stack of the three BUFFALO WFC3/IR bands (F105W, F125W and F160W) for $z \sim 6-7$ detection, a stack of the F125W and F160W bands for $z \sim 8-9$ detection and the F160W band mosaic for $z \sim 9-10$ detection. All three detection images are composed of the foreground-subtracted and point-spread-function (PSF) matched images compiled for the BUFFALO catalogs (Pagul et al. in prep.). We modulate the detection and deblending parameters between the inner and outer fields of the BUFFALO mosaics in order to account for the difference in depth [cf. 138, Pagul et al. in prep.]. Note that while the detection is performed on the three infrared BUFFALO bands, the photometry is measured in all 10 available HST filters. We then measure the IRAC1 and IRAC2 photometry of sources detected in HST with the `photutils` package [25] using the same apertures and correction factors as in [51].

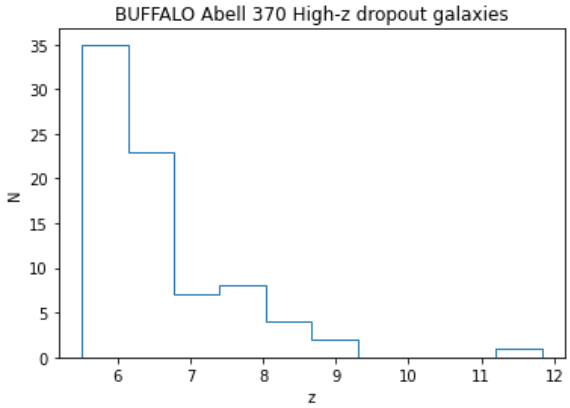

Figure 4.1: Photometric redshift distribution of BUFFALO high-redshift candidate galaxies in Abell 370.

4.2.2 High-redshift sample selection

4.3 Theory

Two-point statistics have a long history as the tool of choice for a lot of cosmological measurements [116, and references thereafter]. This work is centered on the angular two-point correlation function, $w(\theta)$, which describes the excess of probability of finding a pair of galaxies at a separation distance θ compared to a uniform random distribution. Throughout this work, the correlation function is estimated using `TreeCorr` [71] via the Landy-Szalay estimator [91], which uses a set of uniformly distributed random points across the footprint of the survey in order to estimate the correlation function as follows:

$$w(\theta) = \frac{DD(\theta) - 2DR(\theta) + RR(\theta)}{RR(\theta)}, \tag{4.1}$$

where DD represents the data-data pairs, DR the data-random pairs, and RR the random-random pairs. We use a random dataset 100 times larger than the number of sources.

We choose to use 8 log-spaced bins between $1'' < \theta < 120''$. This choice is mainly driven by the density of objects in the parallel fields, as adding more angular bins, increases the complexity of the covariance estimation.

The observed correlation function at these scales is well approximated by a power-law [123]:

$$w_{obs}(\theta) = \langle \delta_{obs} \delta_{obs} \rangle = A_w \theta^{-\beta} - IC. \tag{4.2}$$

Where δ_{obs} is the observed galaxy density contrast, and IC the so-called integral constraint. IC is the so-called integral constraint [59], which can be estimated as [123]:

$$IC = \frac{\sum_i A_w \theta_i^{-\beta} RR(\theta_i)}{\sum_i RR(\theta_i)} + \frac{1}{N_{gal}}. \tag{4.3}$$

If the angular correlation function is a power-law, the 3D correlation function $\xi(r)$, is also a power law:

$$\xi(r) = \left(\frac{r}{r_0} \right)^{-\gamma}, \tag{4.4}$$

where r_0 is the correlation length and $\gamma = \beta + 1$. The amplitude of the angular correlation function is related to both r_0, and γ via:

$$A_w = \frac{K_\gamma r_0^\gamma \int dz F(z) r_c^{1-\gamma}(z) N^2(z) H(z)}{c \left[\int dz N(z) \right]^2}, \tag{4.5}$$

where c is the speed of light in the vacuum, $H(z)$ is the Hubble parameter at redshift z,

$N(z)$ is the redshift distribution of the sample, $r_c(z)$ is the comoving distance at redshift z, $F(z)$ describes the evolution of clustering with redshift, and K_γ is given by:

$$K_\gamma = \Gamma(1/2)\frac{\Gamma[(\gamma-1)/2]}{\Gamma(\gamma/2)}. \tag{4.6}$$

Following [123, 80] we assume constant clustering in the redshift range that our sample spans ($5 < z < 10$), i.e., $F(z) = 1$. Under these assumptions, the galaxy bias, b, is related to r_0, γ [117]:

$$b = \frac{\sigma_{8,gal}}{\sigma_8(z)}, \tag{4.7}$$

with $\sigma_{8,gal}$ given by [117]

$$\sigma_{8,gal} = \frac{72}{(3-\gamma)(4-\gamma)(6-\gamma)2^\gamma}\left(\frac{r_0}{8h^{-1}\mathrm{Mpc}}\right)^\gamma, \tag{4.8}$$

and $\sigma_8(z)$ the amplitude of matter density fluctuations at 8 Mpc h^{-1} at redshift z.

4.3.1 Deflection Corrections

Galaxy clusters are incredibly powerful tools in probing the faintest objects, pushing beyond the technical limits of our current instruments. The BUFFALO images provide the deepest look at galaxy clusters at these wavelengths to date, and its blank fields are second only to the Hubble Ultra Deep Field [HUDF, 18].

However, given the nature of lensing, galaxy positions are distorted on the angular plane. In order to measure the 2-point correlation function of galaxies in this sample, we use

the deflection maps for the Abell 370 cluster[1] [23, 124, 41, 79, 101, 107, 74, 94] to recover the native positions of the sources. We use these maps and scale the deflection angles, $\alpha(\hat{n})$, along the direction of the sky $\hat{n}$ from the lens to the source as follows:

$$\alpha(\hat{n})' = \alpha(\hat{n})\frac{r(z_l, z_s)}{r(z_s)}, \tag{4.9}$$

where $r(z_l, z_s)$ is the comoving distance between the lens and source planes, and $r(z_s)$ is the comoving distance at the source plane, z_s at which the deflection maps are provided. In other words, a source measured along the direction of the sky $\hat{n}$ is considered to be at $\hat{n} + \alpha'$.

We estimate the correlation function for each of these maps, $w(\theta)_{mp}$, except for the Zitrin-team maps, as we find that the orientation of the galaxies seems to be rotated by 90 degrees with respect to the rest. After this a systematic uncertainty due to differences in the lensing models, $\delta w_{\rm defl}$, is computed as the standard deviation of the $w(\theta)_{mp}$ estimates for each map, i.e.,

$$\delta w_{\rm defl} = \sqrt{\frac{1}{N}\left[\sum_{mp} w_{mp}^2(\theta) - \left(\sum_{mp} w_{mp}(\theta)\right)^2\right]} \tag{4.10}$$

4.3.2 Magnification bias

Gravitational lensing modifies the observed number of counts, as magnification allows us to detect galaxies past the unlensed detection threshold of an image, but stretches the observed solid angle behind the lenses [134]. In the presence of magnification, the

[1] available at https://archive.stsci.edu/prepds/frontier/lensmodels/

observed density contrast, $\delta_{obs}(\hat{n})$, in a given direction of the sky $\hat{n}$ can be written as:

$$\delta_{obs}(\hat{n}) = \rho_{obs}(\hat{n})/\langle\rho\rangle - 1 = \delta_{gal}(\hat{n}) + \delta_{\mu}(\hat{n}), \tag{4.11}$$

where $\delta_g(\hat{n}) = b\delta_m(\hat{n})$ describes the intrinsic fluctuations on the number of galaxies, where b is the galaxy bias, and $\delta_{mu}(\hat{n})$ the fluctuations induced by magnification. Following [16] and [104] the magnification in a direction of the sky $\hat{n}$ can be written as

$$\delta_{\mu}(\hat{n}) = \frac{N_{\mu}(\hat{n}, z, f_{\mu})}{N_0(\hat{n}, z, f_0)} - 1, \tag{4.12}$$

where $N_{\mu}(\hat{n}, z, f_{\mu})$ is the lensed cumulative number of counts affected by magnification, and $N_0(\hat{n}, z, f_0)$ the unlensed number of counts, with a flux greater than a threshold f_0, and $f_{\mu} = f_0/\mu$, where μ is the magnification. Parametrizing the cumulative number of counts as a power-law δ_{μ} can be written as [54]:

$$\delta_{\mu}(\hat{n}) = \mu(\hat{n})^{-\alpha(f_{\mu})-1} - 1, \tag{4.13}$$

where $\alpha(f_{\mu})$ can be estimated using the observed number of sources. If we convert to magnitudes the estimation of α can be performed via:

$$\alpha(m) = 2.5\frac{\mathrm{d}}{\mathrm{d}m}\log_{10} N(m). \tag{4.14}$$

Thus, given a magnification map, we can compute δ_μ, and estimate the cross-correlation between the observed number of galaxies and the map:

$$w_{obs,\mu}(\theta) = \langle \delta_{obs} \delta_\mu \rangle = \langle \delta_g \delta_\mu \rangle + \langle \delta_\mu \delta_\mu \rangle. \tag{4.15}$$

On the other hand, the observed angular correlation function of galaxies can be written as

$$\begin{aligned} w_{obs}(\theta) &= \langle \delta_{obs} \delta_{obs} \rangle = \langle \delta_{obs} (\delta_g + \delta_{mu}) \rangle \\ &= \langle \delta_g \delta_g \rangle + \langle \delta_\mu \delta_\mu \rangle + 2 \langle \delta_\mu \delta_g \rangle. \end{aligned} \tag{4.16}$$

Thus, in the case of a field with a large magnification, we can modify the model in equation 4.2 to include the effect of magnification bias as follows:

$$w_{obs}(\theta) = A_w \theta^{-\beta} - IC + 2 w_{\mu,obs}(\theta) - w_\mu(\theta). \tag{4.17}$$

Where $w_{\mu,obs}$ is the cross-correlation between the observed galaxy density and δ_μ, and $w_\mu(\theta)$ is the autocorrelation of δ_μ.

4.3.3 Covariance

For the estimation of the covariance matrix we use the eliminate-one jackknife technique as implemented in `TreeCorr` using 20 equal-area ($\approx$ 1 arcmin^2) regions. This choice is limited by the area coverage of our data, but it allows to properly map the covariance of all angular bins except for the last. This technique can induce biases at the time of inverting that can be corrected by multiplying by a factor H to get the unbiased

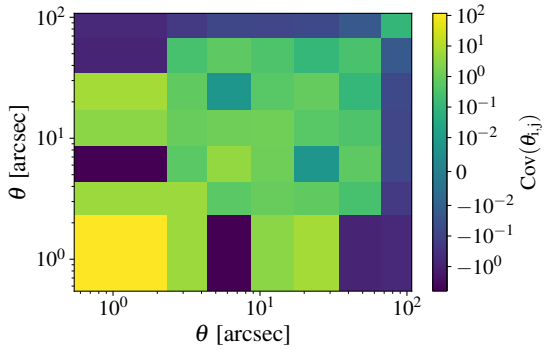

Figure 4.2: Covariance matrix of the cluster field.

covariance [77]:

$$\mathcal{C}_H^{-1} = H\mathcal{C}^{-1} = \left(\frac{N_{\rm JK} - N_{\rm bins} - 2}{N_{\rm JK} - 1}\right)\mathcal{C}^{-1} \,, \tag{4.18}$$

where $N_{\rm bins}$ is the number of angular bins used in the data-vector, $N_{\rm JK}$ is the number of jackknife regions (in our case 20), and C^{-1} the inverse of the jackknife covariance, C. In our case, the original jackknife covariance is corrected by systematic uncertainty in the deflected position as estimated in the previous section, so $C = C_{JK} + (\delta w_{\rm defl})^2 I$, with I the identity matrix. As an example, the covariance matrix for the cluster field is shown in Figure 4.2.

4.4 Galaxy correlation results

In this section we present the estimated values for the angular correlation function of galaxies in the Abell 370 catalogs from BUFFALO in the cluster, the parallel field, and when we consider both fields simultaneously. The results are shown in Figure 4.3. In general, we can see that the different deflection maps give a similar order of magnitude for the angular correlation function of the galaxy sample considered in this work. On the other

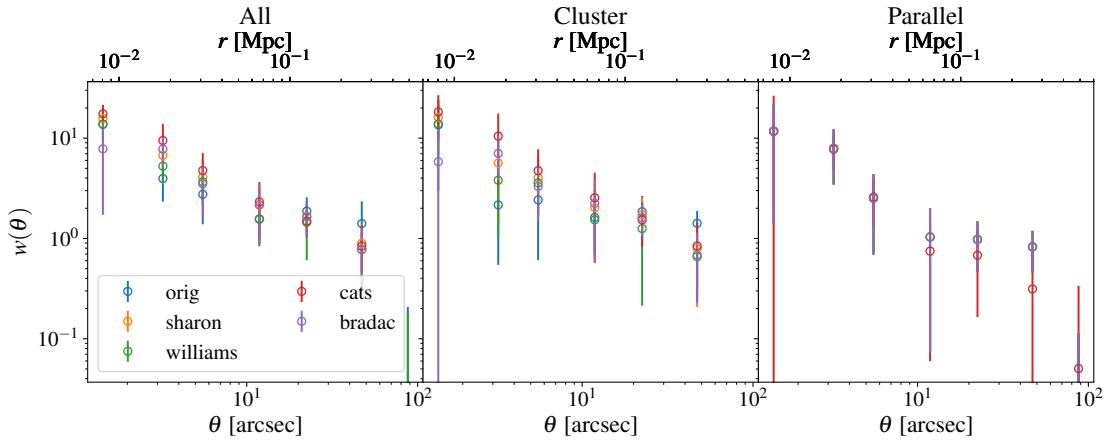

Figure 4.3: Results of correlation function for galaxies z>6 for all fields combined (left), the cluster field (middle), and the parallel field (right). We show the measurements for each of the deflection maps, and without any deflection (orig, blue points). The parallel field is only covered by the CATS map, so all the other maps match with the original measurements.

hand, we can see that for the parallel field we only have two sets of points, as only one of the maps (CATS) covers that area. This is why we consider the CATS results as our fiducial measurements.

4.4.1 Parallel field

For the parallel field, the magnification effect is much lower than for the cluster field, and we can simply follow previous works in the literature [123, 55] and fit the model in equation 4.2 to our data. We minimize the

$$\chi^2 = [w_{obs}(\theta_i) - w_{model}(\theta_i)]\, C_{ij}^{-1}\, [w_{obs}(\theta_j) - w_{model}(\theta_j)] \tag{4.19}$$

and obtain the results in Figure 4.4. We run a Markov Chain Monte Carlo (MCMC) process with `emcee` [49], and use the samples in the chain to obtain the best-

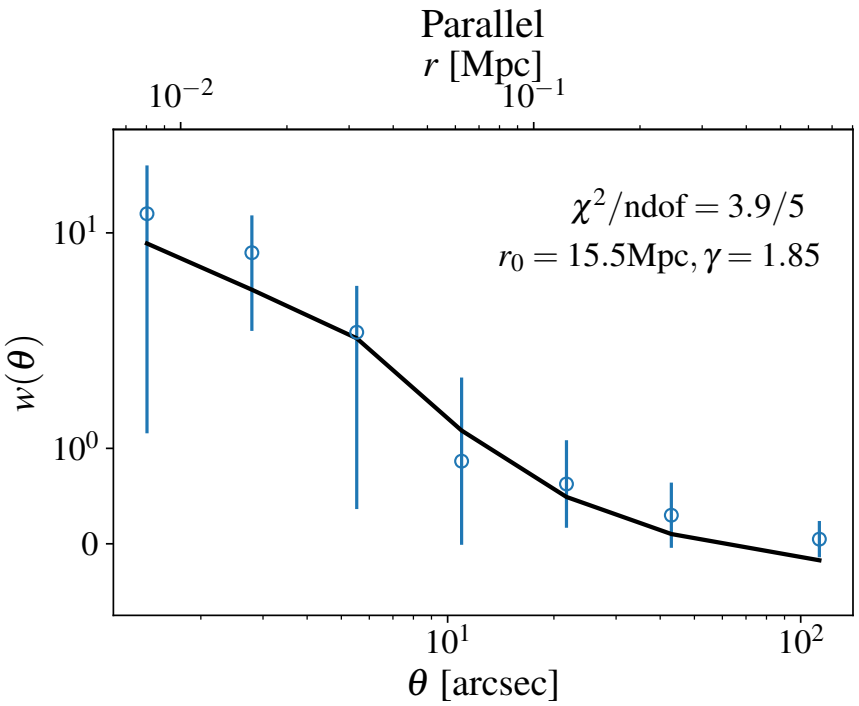

Figure 4.4: Measurement and best-fit model for the parallel field, using the CATS maps deflections.

fit bias and its uncertainty $b = 16.2^{+10.1}_{-6.5}$ (stat.) $\pm$ 1.75 (sys.), at $z \sim 6.32$.

4.4.2 Cluster field

In the case of the cluster field magnification plays a larger role, and should be considered carefully. We compute the correlation function for the galaxies, applying the deflection correction for each of the maps. Additionally, we compute the cross-correlation between the galaxies positions and δ_μ for each of the maps as well as the auto-correlation of δ_μ. Then, we fit the models in equations 4.2 and 4.17 to the observed data obtaining (r_0, γ) for each of the maps.

4.4.3 Systematics

Photometric redshifts

Our models in equations 4.2 and 4.17 require an accurate knowledge of the ensemble redshift distribution of the galaxy sample considered for the analysis. If this distribution is poorly determined or biased, our results would be impacted. In order to evaluate the impact of the redshift uncertainty in our measurements, what we do is to use three different samples from the photo-z probability distributions of each galaxy in our dataset, and evaluate the difference in the best-fit biases.

Deflection and magnification uncertainties

Different lensing maps seem to give different values for the best-fit (r_0, γ), and consequently the inferred galaxy bias. Thus, we run our measurements, and inference pipeline to obtain (r_0, γ, b), and assign a systematic uncertainty to the final bias result computed as the standard deviation of the best-bias values obtained for each map.

4.5 Summary and Future Work

This chapter presents the first measurement of the 2-point correlation function at redshift >6 for drop-out galaxies. Leveraging the clusters' strong lensing, we measure a statistically significant signal in the correlation function. After fitting the signal to a power-law, we recover a clustering radius, $r_0 = 15.5$Mpc, and a $gamma = 1.85$. From this, we extract a galaxy bias, $b_0 = 16.2^{+10.09}_{-6.52}$. This value is compatible with extrapolating previous works. Figure 4.5 shows these results, where our measurement is in black and it

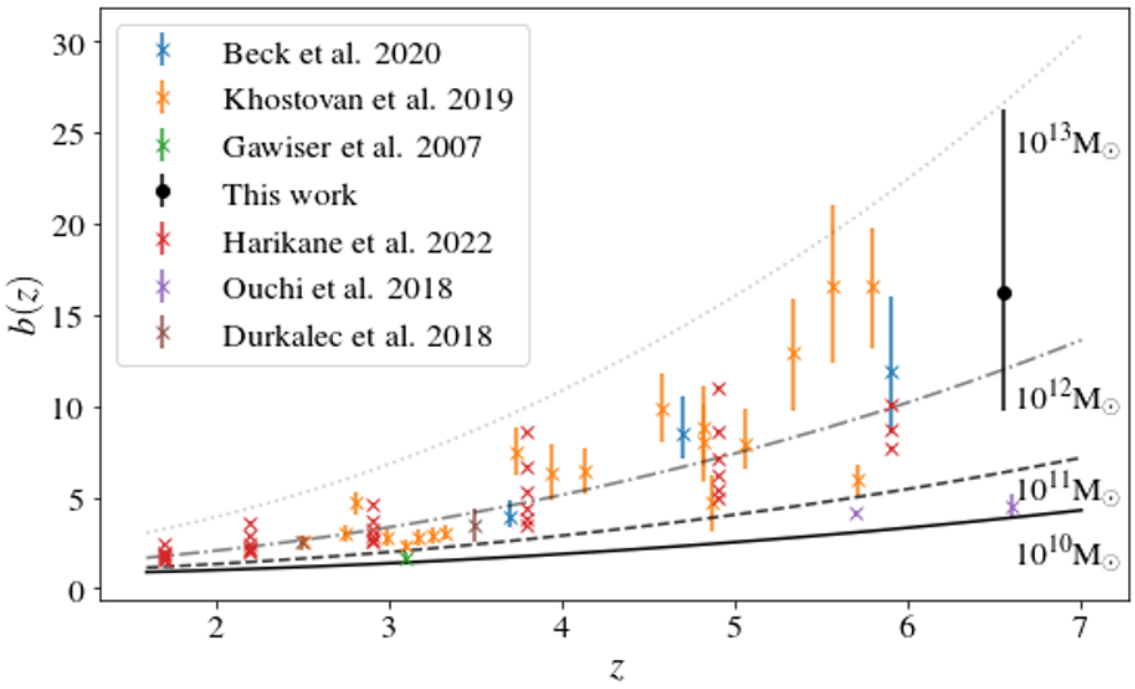

Figure 4.5: The black-filled circle corresponds to the galaxy bias value measured in this work. The other shapes correspond to the previous works, as labeled in the legend, that measured galaxy bias at varying redshifts.

is over plotted on previous works.

We also note compatibility with results whose sample selection and cuts were different from this work. This means that different works might be probing different populations of galaxies. For example, the orange $\times$ correspond to a sample of Lyman-alpha emitters (LAE), which probe blue galaxies, in contrast to our sample of drop-out galaxies that tend to probe redder galaxies. The compatibility between these measurements, then, might be surprising. However, previous works, such as in ref [44], imply that the difference in the galaxy bias between different galaxy populations converges with higher redshift (i.e. $z >\sim 2.75$).

Future developments of this work include measuring and fitting cosmology pa-

rameters to the 2-pt correlation function of the cluster field, and ultimately extending this analysis to the remaining five HFF/BUFFALO clusters. This will increase our signal-to-noise by a factor $\sim \sqrt{5}$, which will ultimately reduce our error bars to increase sensitivity to the bias parameter.

Chapter 5

Ongoing and Future Work

5.1 Intra-cluster light as a tracer of dark matter

5.1.1 Introduction

It is well-established that galaxies are biased tracers of the matter density field, particularly at small scales, where astrophysical processes such as feedback dominate over the gravitational effects. The gas responsible for the emission of the intracluster light follows the same gravitational potential as the underlying dark matter density field. If we consider the intracluster light to be a proxy for a test particle that is not gravitationally bound to any specific galaxy, but is instead bound predominantly to the underlying dark matter density field of the cluster itself, we can access information at smaller scales of the density field. Several studies have shown indications of a correlation between the ICL and the DM field [112, 129]. Future studies like the one we propose are vital in furthering our understanding of these correlations. If confirmed, these ICL maps can both inform lensing

models/mass maps, and establish metrics that test the reliability of these mass maps. These metrics include: the measurement of the degree of correlation between the ICL models and the mass (DM) maps (Fig. 5) and the comparison of this degree of correlation with the robustness metrics that the lensing community already uses (i.e. the offset that measures the astrometric difference between where lenses should be based on their model and where they are located in real data). If we find our ICL maps correlate best with the best self-report lens maps, we will use the ICL maps a prior to inform the construction of new, more reliable, lens maps.

Furthermore, there are still significant open questions about the nature of the ICL, which include: (i) intra-cluster light is shown to contribute significantly to the light in clusters. However, the actual contribution ranges between 10-50% according to different studies [19, 143]. We will set tighter constraints on these fractions by comparing the total light in the cluster to the ICL models that we constructed for HFF and BUFFALO, along with publicly available data. (ii) There is a limited understanding of the color and nature of the ICL. Currently, it is unclear how the color of the ICL correlates with the galaxies in the cluster. We will use our models of both the ICL and the cluster galaxies to study these correlations and create a picture of how the fluxes change in both as a function of wavelength.

5.1.2 Comparing intra-cluster light maps with lensing κ maps

In order to test the theory that the ICL light traces the underlying dark matter gravitational potential, we begin by matching the resolution, pixel, and image size between different κ maps produced by the lensing community and the ICL for the Abell 2744 cluster.

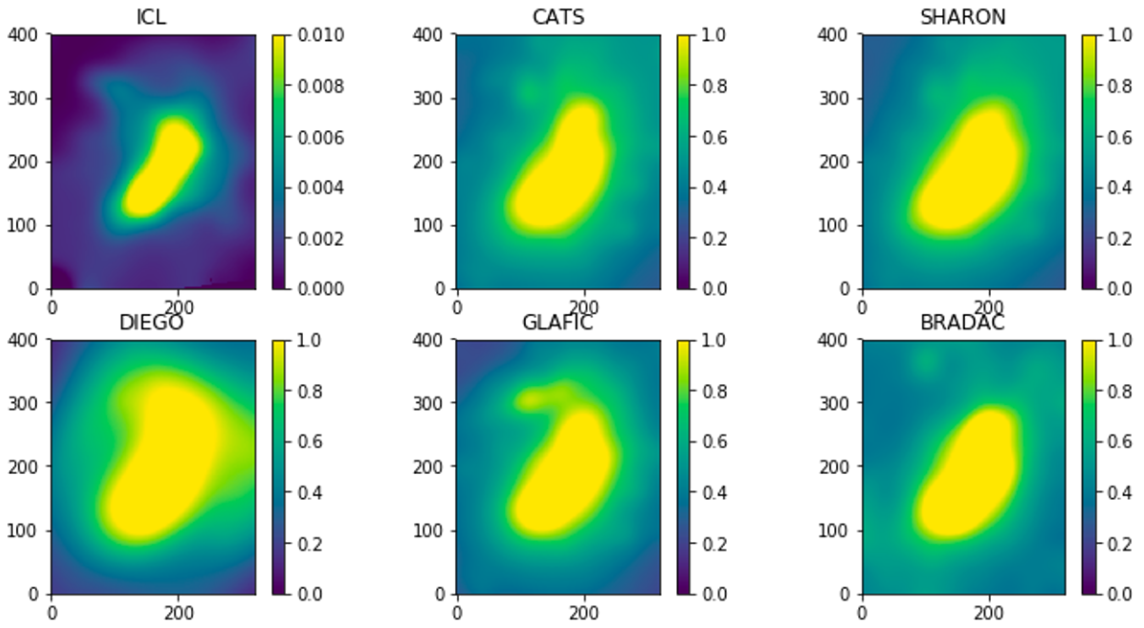

Figure 5.1: Caption

Figure 5.1 shows the maps used in this analysis. Qualitatively, it is immediately clear that the shapes of these maps are comparable.

Following [112], in order to measure the similarity between the maps in Figure 5.1, we use a shape similarity metric called the Modified Hausdorff Distance (MHD), which is defined as:

$$d(X,Y) = \frac{1}{N_X} \sum_{x_i \in X} \min_{y_j \in Y} ||x_i - y_j|| \tag{5.1}$$

where x and y correspond to pixel coordinates, X and Y is the set containing pixels x and y, and N is the total number of pixels in X. The smaller the MHD values, the more similar the shapes.

We measure the MHD between our ICL and the κ maps, as well as the MHD between the maps themselves. The results of these measurements are shown in Figure 5.2.

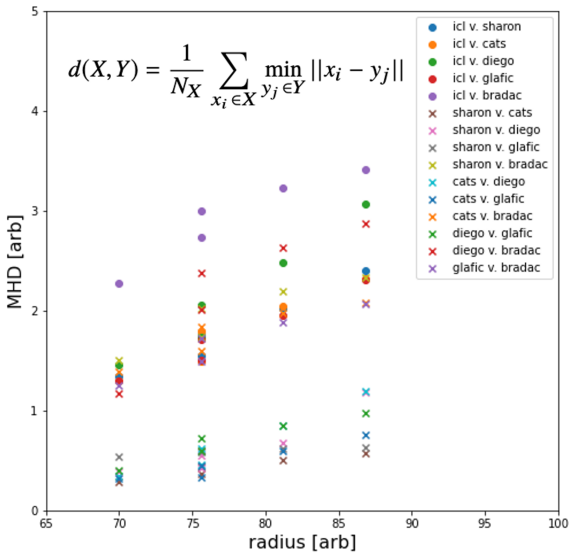

Figure 5.2: MHD measurements as a function of aperture for the ICL and κ maps in the Abell 370 cluster. The ICL and κ map comparisons are denoted with circles, where the color corresponds to each individual κ map. The MHD comparing the κ maps to eachother are denoted with a $\times$.

The MHD comparing the ICL to the κ maps are denoted with circles, where the color corresponds to each individual κ map. The MHD comparing the κ maps to eachother are denoted with a $\times$. We note that the scatter in the MHD measurement for both cases is similar. The trend of the MHD between pairs of maps is consistent for all the aperture radii.

5.1.3 Future work

The ICL contains a wealth of information about cluster formation and the dark matter content. In the future, I will perform similarity measurements with the rest of the clusters to check for consistency across different fields. I aim to analyze the trends in the astrometric offset of κ maps which are most similar to the ICL. Astrometric offsets are one

of the metrics lens team use to indicate the quality of their κ maps.

I will also study how the ICL changes as a function of wavelength. This will help us understand where the cluster is in its evolution. This will further help us understand the distribution of the underlying dark matter density field and its shape discrepancies with the ICL. For example, due to fluid dynamics, baryonic processes, such as mergers, rearrange the distribution of the baryons in the field on smaller time scales than cold dark matter particles (which are only acted upon by gravity). Therefore, the dark matter density field needs time to catch up to the perturbed field, and this can cause shape discrepancies between the ICL and the κ maps. Understanding how the ICL changes as a function of wavelength can better inform baryonic process that it underwent, and we can use that as a floating parameter when comparing with the community's κ maps.

5.2 Combining space- and ground-based data with the Hubble Frontier Fields and the Dark Energy Survey

5.2.1 Introduction

In order to maximize the scientific outcome of current surveys and effectively prepare for the upcoming generation of large surveys, developing synergies between deep space-based data and wide ground-based data is required. Leveraging data from these two sources will help us better understand the largest- and smallest-scale features of the universe, and even more importantly, connect the underlying physical processes between these two scales. I utilize data from both the Hubble Frontier Fields (HFF) program [95] and the Fermilab-led Dark Energy Survey (DES) [48] to find synergies between the two.

For example, the more than 300 million galaxies observed in DES provide robust statistical information about the properties of our universe. This information can be used to drive error analyses and characterizations of the galaxy population in the HFF. On the other hand, the unparalleled resolution and depth of the HFF images provide resolved information about galaxy morphology, formation, and evolution beyond DES capabilities. The optical HFF wavebands these clusters were observed in overlap with the DES grizY filter system, making it possible to compare the datasets in a robust way. Combined, these clusters and their parallel fields provide a unique sample overlapping with DES, consisting of thousands of galaxies in various environments and redshifts, necessary to address questions about galaxy cluster formation and evolution. This dataset has the potential to inform and calibrate large statistical studies in DES.

5.2.2 Results

Data gathering and processing:

i. I identified the tiles that corresponded to each of the 4 Frontier Field (FF) clusters in DES (and 1 in DECals), and obtained the relevant data products including PSF characterizations, detection maps, catalogs, and the images themselves.

ii. I set up the TPHOT pipeline (a prior based photometry code) to run on the DES data and use the FF data as priors, identifying the deblended galaxies and their positions.

iii. After tests with TPHOT, I have constructed an analytic PSF for the DES data since the measured PSF generated artifacts in the TPHOT measurements. I am exploring why this is the case, as both analytic and measured PSFs seem to behave similarly.

iv. I created catalogs for the HST Abell 370 cluster and matched the detected objects to the relevant DES catalog.

Deblending and photometry results:

i. I have successfully modeled the DES galaxies using the HST images as priors, as evidenced by residuals consistent with noise levels (Figure 5.3, where the original DES image is on the left, and the residual after modeling is on the right).

ii. I found consistent photometry between DES and the FF up until the 5-sigma depth in 3 bands, g-, r-, and i-band (matched with the F435W, F606W, and F814W HST bands, respectively), showing the great quality of the DES data, and validating this procedure. Discrepancies started to show up on the fainter end due to noise fluctuations, as expected.

iii. I have also characterized the deblending efficiency in this crowded environment. In these extreme, high density environments, $\sim 30\%$ of the objects detected show some degree of blending still to be characterized.

5.2.3 Future Work

I will finish the analysis of the Abell 370 cluster, and continue with the remaining three available HFF clusters (Abell 2744, Abell S1063, MACS 0416) which exist in the DES footprint (along with an additional cluster, MACS 1149, which appears in the DECam Legacy Surveys). This overlap provides a unique and exciting opportunity to explore the relationships between these large datasets. I also plan on measuring the relationship between

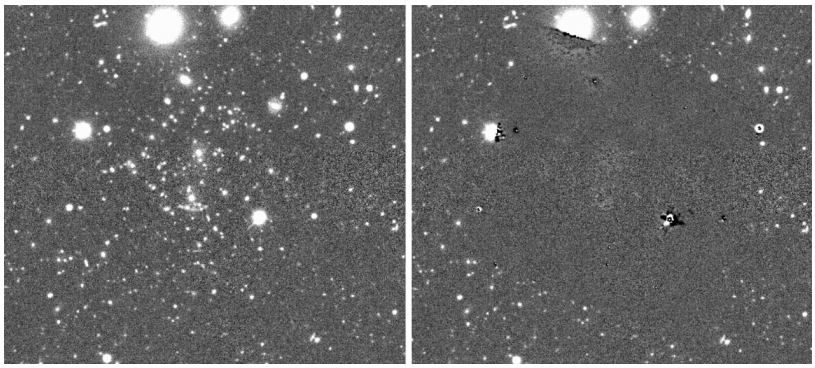

Figure 5.3: Left: Original DES Abell 370 image in g-band, Right: Residual after model subtraction, showing that only part of the Intra cluster light and the background fluctuations are left after the model subtraction.

the surface brightness of each galaxy versus its redshift in order to test redshift calibration and cosmology.

5.3 Preparing for the James Webb Space Telescope

5.3.1 Introduction

With the recent launch of the James Webb Space Telescope (JWST) it is an exciting time to be an astronomer. The JWST early release data has already shown dramatic improvements in resolution and depth compared with previous surveys. Given the experience in image processing gained in performing the work in this thesis, it is especially timely to apply these pipelines to the newly released data.

5.3.2 Preliminary morphology tests

We turn our attention to the SMACS-0723 cluster that was observed by JWST. As an initial check, we only select the filters (F090W and F200W) which either overlap,

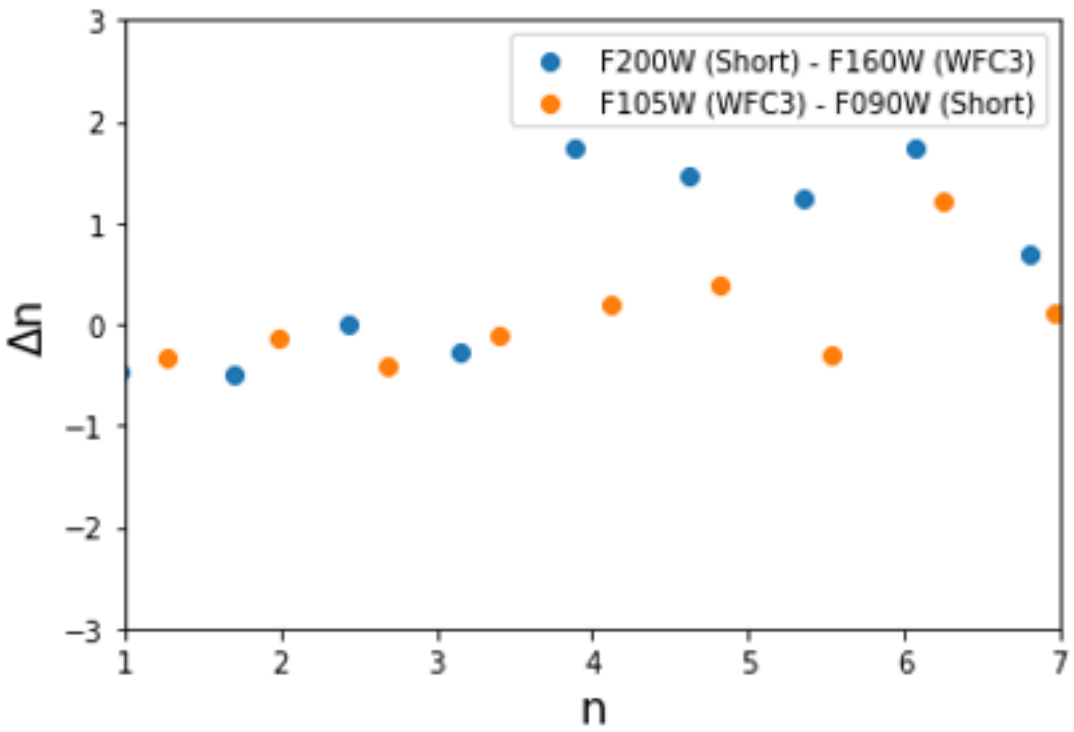

Figure 5.4: Difference in S'ersic index between the closest HST and JWST overlapping bands where the bluer band is subtracted from the redder band. Orange points correspond to $n_{\mathrm{F200W}} - \mathrm{F160W}$. Blue points correspond to $n_{\mathrm{F105W}} - n_{\mathrm{F090W}}$.

or are directly adjacent to, an HST filter (F105W and F200W, respectively). We use the previously described GALAPAGOS-M in order to perform morphology fits to the brightest galaxies in this field, and compare the resulting morphology between the HST data and the JWST data of the same galaxies. Figure 5.4, shows a subset of the results of this analysis. We plot the difference in the Sérsic index, Δn, between the closest JWST and HST bands. We note that Δn is approximately consistent between the bands up until $n \sim 4$. This is a reassuring test which shows the robustness of the data. We note that because the Sérsic index is the power term in the measurement of the galaxy profile, the discrepancy after n$\sim$4 does not represent a large difference in the galaxy profiles.

5.3.3 Future work

With this robustness check, we aim to perform a morphological analysis of all of the galaxies in the SMACS-0723 cluster for all JWST bands. This will open a window into understanding properties of galaxies at redder wavelengths that reach beyond the HST range with unprecedented resolution and depth. We also aim to work with the community to develop tools that can be used to robustly reduce this rich dataset.

Chapter 6

Conclusions

To reiterate the first sentence of this thesis, *galaxy clusters are the bridge between cosmology and astrophysics*. In this thesis, I aim to understand galaxy clusters at the pixel level, and develop tools to robustly extract information to answer open questions in astrophysics and cosmology. This point is fundamentally important because understanding behavior, systematics, and fine details of the low-level products enables us to further push the limits of this dataset.

I have presented a comprehensive study of how to extract meaningful information in extremely crowded and complex environments. I have used this pipeline and demonstrated its adaptability to new and improved datasets. The data products are available for the community and have served as input for other studies (Santini et al. in prep).

I have used these data products to understand the galaxy-halo connection at high redshift by measuring the 2-pt correlation function and extracting the galaxy bias. Our measurements indicate that the bias values recovered are compatible with previous studies

which use a sample of galaxy dropouts at lower redshifts. This work also points to the compatibility of the galaxy bias between different galaxy populations at high redshift.

I have also explored ways in which to use the tools developed for this thesis to combine space- and ground-based datasets from HFF and DES. This is particularly challenging due to the resolution, depth, and coverage differences. However, this study could be particularly helpful to make precise predictions for future missions such as JWST, LSST, EUCLID, and Roman, which include understanding number densities at a different depths, the luminosity function at high redshifts, and performance of photometric redshift algorithms for high-z galaxies.

I have started using these data products to explore the light-to-dark relationship between the ICL and the underlying dark matter density fields, which are modeled as convergence κ maps by different teams. This work indicated correlation of shape between the ICL and κ maps. Furthermore, we quantify the similarity between the κ and ICL maps using the MHD, as well as the κ maps between themselves. This tool allows us to identify discrepancies and trends among the lensing maps.

Finally, with the launch of JWST, data of unprecedented depth and resolution will unveil the secrets of the infrared universe. It is especially important to have robust tools to efficiently reduce this wealth of data. In this work, I present an early morphology comparison with HST data on overlapping or adjacent filter bands. We find that these preliminary morphology results are promising, showing compatibility between HST and JWST. With this first result, we demonstrate the adaptability of the pipeline presented in this work.

This is an especially exciting time to be an astronomer and I am excited to continue and expand the knowledge and tools gained from this work to further push the boundaries and understanding of our universe.

Bibliography

[1] T. M. C. Abbott, M. Aguena, A. Alarcon, S. Allam, O. Alves, A. Amon, F. Andrade-Oliveira, J. Annis, S. Avila, D. Bacon, E. Baxter, K. Bechtol, M. R. Becker, G. M. Bernstein, S. Bhargava, S. Birrer, J. Blazek, A. Brandao-Souza, S. L. Bridle, D. Brooks, E. Buckley-Geer, D. L. Burke, H. Camacho, A. Campos, A. Carnero Rosell, M. Carrasco Kind, J. Carretero, F. J. Castander, R. Cawthon, C. Chang, A. Chen, R. Chen, A. Choi, C. Conselice, J. Cordero, M. Costanzi, M. Crocce, L. N. da Costa, M. E. da Silva Pereira, C. Davis, T. M. Davis, J. De Vicente, J. DeRose, S. Desai, E. Di Valentino, H. T. Diehl, J. P. Dietrich, S. Dodelson, P. Doel, C. Doux, A. Drlica-Wagner, K. Eckert, T. F. Eifler, F. Elsner, J. Elvin-Poole, S. Everett, A. E. Evrard, X. Fang, A. Farahi, E. Fernandez, I. Ferrero, A. Ferté, P. Fosalba, O. Friedrich, J. Frieman, J. García-Bellido, M. Gatti, E. Gaztanaga, D. W. Gerdes, T. Giannantonio, G. Giannini, D. Gruen, R. A. Gruendl, J. Gschwend, G. Gutierrez, I. Harrison, W. G. Hartley, K. Herner, S. R. Hinton, D. L. Hollowood, K. Honscheid, B. Hoyle, E. M. Huff, D. Huterer, B. Jain, D. J. James, M. Jarvis, N. Jeffrey, T. Jeltema, A. Kovacs, E. Krause, R. Kron, K. Kuehn, N. Kuropatkin, O. Lahav, P. F. Leget, P. Lemos, A. R. Liddle, C. Lidman, M. Lima, H. Lin, N. MacCrann, M. A. G. Maia, J. L. Marshall, P. Martini, J. McCullough, P. Melchior, J. Mena-Fernández, F. Menanteau, R. Miquel, J. J. Mohr, R. Morgan, J. Muir, J. Myles, S. Nadathur, A. Navarro-Alsina, R. C. Nichol, R. L. C. Ogando, Y. Omori, A. Palmese, S. Pandey, Y. Park, F. Paz-Chinchón, D. Petravick, A. Pieres, A. A. Plazas Malagón, A. Porredon, J. Prat, M. Raveri, M. Rodriguez-Monroy, R. P. Rollins, A. K. Romer, A. Roodman, R. Rosenfeld, A. J. Ross, E. S. Rykoff, S. Samuroff, C. Sánchez, E. Sanchez, J. Sanchez, D. Sanchez Cid, V. Scarpine, M. Schubnell, D. Scolnic, L. F. Secco, S. Serrano, I. Sevilla-Noarbe, E. Sheldon, T. Shin, M. Smith, M. Soares-Santos, E. Suchyta, M. E. C. Swanson, M. Tabbutt, G. Tarle, D. Thomas, C. To, A. Troja, M. A. Troxel, D. L. Tucker, I. Tutusaus, T. N. Varga, A. R. Walker, N. Weaverdyck, R. Wechsler, J. Weller, B. Yanny, B. Yin, Y. Zhang, J. Zuntz, and DES Collaboration. Dark Energy Survey Year 3 results: Cosmological constraints from galaxy clustering and weak lensing. , 105(2):023520, January 2022.

[2] Hiroaki Aihara, Nobuo Arimoto, Robert Armstrong, Stéphane Arnouts, Neta A. Bahcall, Steven Bickerton, James Bosch, Kevin Bundy, Peter L. Capak, James H. H. Chan, Masashi Chiba, Jean Coupon, Eiichi Egami, Motohiro Enoki, Francois Finet, Hiroki Fujimori, Seiji Fujimoto, Hisanori Furusawa, Junko Furusawa, Tomotsugu Goto, Andy Goulding, Johnny P. Greco, Jenny E. Greene, James E. Gunn, Takashi

Hamana, Yuichi Harikane, Yasuhiro Hashimoto, Takashi Hattori, Masao Hayashi, Yusuke Hayashi, Krzysztof G. Hełminiak, Ryo Higuchi, Chiaki Hikage, Paul T. P. Ho, Bau-Ching Hsieh, Kuiyun Huang, Song Huang, Hiroyuki Ikeda, Masatoshi Imanishi, Akio K. Inoue, Kazushi Iwasawa, Ikuru Iwata, Anton T. Jaelani, Hung-Yu Jian, Yukiko Kamata, Hiroshi Karoji, Nobunari Kashikawa, Nobuhiko Katayama, Satoshi Kawanomoto, Issha Kayo, Jin Koda, Michitaro Koike, Takashi Kojima, Yutaka Komiyama, Akira Konno, Shintaro Koshida, Yusei Koyama, Haruka Kusakabe, Alexie Leauthaud, Chien-Hsiu Lee, Lihwai Lin, Yen-Ting Lin, Robert H. Lupton, Rachel Mandelbaum, Yoshiki Matsuoka, Elinor Medezinski, Sogo Mineo, Shoken Miyama, Hironao Miyatake, Satoshi Miyazaki, Rieko Momose, Anupreeta More, Surhud More, Yuki Moritani, Takashi J. Moriya, Tomoki Morokuma, Shiro Mukae, Ryoma Murata, Hitoshi Murayama, Tohru Nagao, Fumiaki Nakata, Mana Niida, Hiroko Niikura, Atsushi J. Nishizawa, Yoshiyuki Obuchi, Masamune Oguri, Yukie Oishi, Nobuhiro Okabe, Sakurako Okamoto, Yuki Okura, Yoshiaki Ono, Masato Onodera, Masafusa Onoue, Ken Osato, Masami Ouchi, Paul A. Price, Tae-Soo Pyo, Masao Sako, Marcin Sawicki, Takatoshi Shibuya, Kazuhiro Shimasaku, Atsushi Shimono, Masato Shirasaki, John D. Silverman, Melanie Simet, Joshua Speagle, David N. Spergel, Michael A. Strauss, Yuma Sugahara, Naoshi Sugiyama, Yasushi Suto, Sherry H. Suyu, Nao Suzuki, Philip J. Tait, Masahiro Takada, Tadafumi Takata, Naoyuki Tamura, Manobu M. Tanaka, Masaomi Tanaka, Masayuki Tanaka, Yoko Tanaka, Tsuyoshi Terai, Yuichi Terashima, Yoshiki Toba, Nozomu Tominaga, Jun Toshikawa, Edwin L. Turner, Tomohisa Uchida, Hisakazu Uchiyama, Keiichi Umetsu, Fumihiro Uraguchi, Yuji Urata, Tomonori Usuda, Yousuke Utsumi, Shiang-Yu Wang, Wei-Hao Wang, Kenneth C. Wong, Kiyoto Yabe, Yoshihiko Yamada, Hitomi Yamanoi, Naoki Yasuda, Sherry Yeh, Atsunori Yonehara, and Suraphong Yuma. The Hyper Suprime-Cam SSP Survey: Overview and survey design. , 70:S4, January 2018.

[3] Rachel Akeson, Lee Armus, Etienne Bachelet, Vanessa Bailey, Lisa Bartusek, Andrea Bellini, Dominic Benford, David Bennett, Aparna Bhattacharya, Ralph Bohlin, Martha Boyer, Valerio Bozza, Geoffrey Bryden, Sebastiano Calchi Novati, Kenneth Carpenter, Stefano Casertano, Ami Choi, David Content, Pratika Dayal, Alan Dressler, Olivier Doré, S. Michael Fall, Xiaohui Fan, Xiao Fang, Alexei Filippenko, Steven Finkelstein, Ryan Foley, Steven Furlanetto, Jason Kalirai, B. Scott Gaudi, Karoline Gilbert, Julien Girard, Kevin Grady, Jenny Greene, Puragra Guhathakurta, Chen Heinrich, Shoubaneh Hemmati, David Hendel, Calen Henderson, Thomas Henning, Christopher Hirata, Shirley Ho, Eric Huff, Anne Hutter, Rolf Jansen, Saurabh Jha, Samson Johnson, David Jones, Jeremy Kasdin, Patrick Kelly, Robert Kirshner, Anton Koekemoer, Jeffrey Kruk, Nikole Lewis, Bruce Macintosh, Piero Madau, Sangeeta Malhotra, Kaisey Mandel, Elena Massara, Daniel Masters, Julie McEnery, Kristen McQuinn, Peter Melchior, Mark Melton, Bertrand Mennesson, Molly Peeples, Matthew Penny, Saul Perlmutter, Alice Pisani, Andrés Plazas, Radek Poleski, Marc Postman, Clément Ranc, Bernard Rauscher, Armin Rest, Aki Roberge, Brant Robertson, Steven Rodney, James Rhoads, Jason Rhodes, Jr. Ryan, Russell, Kailash Sahu, David Sand, Dan Scolnic, Anil Seth, Yossi Shvartzvald, Karelle Siellez, Arfon Smith, David Spergel, Keivan Stassun, Rachel Street, Louis-Gregory Strolger, Alexander

Szalay, John Trauger, M. A. Troxel, Margaret Turnbull, Roeland van der Marel, Anja von der Linden, Yun Wang, David Weinberg, Benjamin Williams, Rogier Windhorst, Edward Wollack, Hao-Yi Wu, Jennifer Yee, and Neil Zimmerman. The Wide Field Infrared Survey Telescope: 100 Hubbles for the 2020s. *arXiv e-prints*, page arXiv:1902.05569, February 2019.

[4] Shadab Alam, Marie Aubert, Santiago Avila, Christophe Balland, Julian E. Bautista, Matthew A. Bershady, Dmitry Bizyaev, Michael R. Blanton, Adam S. Bolton, Jo Bovy, Jonathan Brinkmann, Joel R. Brownstein, Etienne Burtin, Solène Chabanier, Michael J. Chapman, Peter Doohyun Choi, Chia-Hsun Chuang, Johan Comparat, Marie-Claude Cousinou, Andrei Cuceu, Kyle S. Dawson, Sylvain de la Torre, Arnaud de Mattia, Victoria de Sainte Agathe, Hélion du Mas des Bourboux, Stephanie Escoffier, Thomas Etourneau, James Farr, Andreu Font-Ribera, Peter M. Frinchaboy, Sebastien Fromenteau, Héctor Gil-Marín, Jean-Marc Le Goff, Alma X. Gonzalez-Morales, Violeta Gonzalez-Perez, Kathleen Grabowski, Julien Guy, Adam J. Hawken, Jiamin Hou, Hui Kong, James Parker, Mark Klaene, Jean-Paul Kneib, Sicheng Lin, Daniel Long, Brad W. Lyke, Axel de la Macorra, Paul Martini, Karen Masters, Faizan G. Mohammad, Jeongin Moon, Eva-Maria Mueller, Andrea Muñoz-Gutiérrez, Adam D. Myers, Seshadri Nadathur, Richard Neveux, Jeffrey A. Newman, Pasquier Noterdaeme, Audrey Oravetz, Daniel Oravetz, Nathalie Palanque-Delabrouille, Kaike Pan, Romain Paviot, Will J. Percival, Ignasi Pérez-Ràfols, Patrick Petitjean, Matthew M. Pieri, Abhishek Prakash, Anand Raichoor, Corentin Ravoux, Mehdi Rezaie, James Rich, Ashley J. Ross, Graziano Rossi, Rossana Ruggeri, Vanina Ruhlmann-Kleider, Ariel G. Sánchez, F. Javier Sánchez, José R. Sánchez-Gallego, Conor Sayres, Donald P. Schneider, Hee-Jong Seo, Arman Shafieloo, Anže Slosar, Alex Smith, Julianna Stermer, Amelie Tamone, Jeremy L. Tinker, Rita Tojeiro, Mariana Vargas-Magaña, Andrei Variu, Yuting Wang, Benjamin A. Weaver, Anne-Marie Weijmans, Christophe Yèche, Pauline Zarrouk, Cheng Zhao, Gong-Bo Zhao, and Zheng Zheng. Completed SDSS-IV extended Baryon Oscillation Spectroscopic Survey: Cosmological implications from two decades of spectroscopic surveys at the Apache Point Observatory. , 103(8):083533, April 2021.

[5] C. Alard and Robert H. Lupton. A Method for Optimal Image Subtraction. , 503(1):325–331, Aug 1998.

[6] Anahita Alavi, Brian Siana, Johan Richard, Marc Rafelski, Mathilde Jauzac, Marceau Limousin, William R. Freeman, Claudia Scarlata, Brant Robertson, Daniel P. Stark, Harry I. Teplitz, and Vandana Desai. The Evolution of the Faint End of the UV Luminosity Function during the Peak Epoch of Star Formation (1 < z < 3). , 832(1):56, Nov 2016.

[7] S. Arnouts, S. Cristiani, L. Moscardini, S. Matarrese, F. Lucchin, A. Fontana, and E. Giallongo. Measuring and modelling the redshift evolution of clustering: the Hubble Deep Field North. , 310(2):540–556, December 1999.

[8] Astropy Collaboration, A. M. Price-Whelan, B. M. Sipőcz, H. M. Günther, P. L. Lim, S. M. Crawford, S. Conseil, D. L. Shupe, M. W. Craig, N. Dencheva, A. Ginsburg,

J. T. Vand erPlas, L. D. Bradley, D. Pérez-Suárez, M. de Val-Borro, T. L. Aldcroft, K. L. Cruz, T. P. Robitaille, E. J. Tollerud, C. Ardelean, T. Babej, Y. P. Bach, M. Bachetti, A. V. Bakanov, S. P. Bamford, G. Barentsen, P. Barmby, A. Baumbach, K. L. Berry, F. Biscani, M. Boquien, K. A. Bostroem, L. G. Bouma, G. B. Brammer, E. M. Bray, H. Breytenbach, H. Buddelmeijer, D. J. Burke, G. Calderone, J. L. Cano Rodríguez, M. Cara, J. V. M. Cardoso, S. Cheedella, Y. Copin, L. Corrales, D. Crichton, D. D'Avella, C. Deil, É. Depagne, J. P. Dietrich, A. Donath, M. Droettboom, N. Earl, T. Erben, S. Fabbro, L. A. Ferreira, T. Finethy, R. T. Fox, L. H. Garrison, S. L. J. Gibbons, D. A. Goldstein, R. Gommers, J. P. Greco, P. Greenfield, A. M. Groener, F. Grollier, A. Hagen, P. Hirst, D. Homeier, A. J. Horton, G. Hosseinzadeh, L. Hu, J. S. Hunkeler, Ž. Ivezić, A. Jain, T. Jenness, G. Kanarek, S. Kendrew, N. S. Kern, W. E. Kerzendorf, A. Khvalko, J. King, D. Kirkby, A. M. Kulkarni, A. Kumar, A. Lee, D. Lenz, S. P. Littlefair, Z. Ma, D. M. Macleod, M. Mastropietro, C. McCully, S. Montagnac, B. M. Morris, M. Mueller, S. J. Mumford, D. Muna, N. A. Murphy, S. Nelson, G. H. Nguyen, J. P. Ninan, M. Nöthe, S. Ogaz, S. Oh, J. K. Parejko, N. Parley, S. Pascual, R. Patil, A. A. Patil, A. L. Plunkett, J. X. Prochaska, T. Rastogi, V. Reddy Janga, J. Sabater, P. Sakurikar, M. Seifert, L. E. Sherbert, H. Sherwood-Taylor, A. Y. Shih, J. Sick, M. T. Silbiger, S. Singanamalla, L. P. Singer, P. H. Sladen, K. A. Sooley, S. Sornarajah, O. Streicher, P. Teuben, S. W. Thomas, G. R. Tremblay, J. E. H. Turner, V. Terrón, M. H. van Kerkwijk, A. de la Vega, L. L. Watkins, B. A. Weaver, J. B. Whitmore, J. Woillez, V. Zabalza, and Astropy Contributors. The Astropy Project: Building an Open-science Project and Status of the v2.0 Core Package. , 156(3):123, September 2018.

[9] Astropy Collaboration, T. P. Robitaille, E. J. Tollerud, P. Greenfield, M. Droettboom, E. Bray, T. Aldcroft, M. Davis, A. Ginsburg, A. M. Price-Whelan, W. E. Kerzendorf, A. Conley, N. Crighton, K. Barbary, D. Muna, H. Ferguson, F. Grollier, M. M. Parikh, P. H. Nair, H. M. Unther, C. Deil, J. Woillez, S. Conseil, R. Kramer, J. E. H. Turner, L. Singer, R. Fox, B. A. Weaver, V. Zabalza, Z. I. Edwards, K. Azalee Bostroem, D. J. Burke, A. R. Casey, S. M. Crawford, N. Dencheva, J. Ely, T. Jenness, K. Labrie, P. L. Lim, F. Pierfederici, A. Pontzen, A. Ptak, B. Refsdal, M. Servillat, and O. Streicher. Astropy: A community Python package for astronomy. , 558:A33, October 2013.

[10] H. Atek, J. Richard, J.-P. Kneib, M. Jauzac, D. Schaerer, B. Clement, M. Limousin, E. Jullo, P. Natarajan, E. Egami, and H. Ebeling. New Constraints on the Faint End of the UV Luminosity Function at z ˜ 7-8 Using the Gravitational Lensing of the Hubble Frontier Fields Cluster A2744. , 800:18, February 2015.

[11] Hakim Atek, Johan Richard, Jean-Paul Kneib, and Daniel Schaerer. The extreme faint end of the UV luminosity function at z $\sim$ 6 through gravitational telescopes: a comprehensive assessment of strong lensing uncertainties. , 479(4):5184–5195, October 2018.

[12] I. Balestra, A. Mercurio, B. Sartoris, M. Girardi, C. Grillo, M. Nonino, P. Rosati, A. Biviano, S. Ettori, W. Forman, C. Jones, A. Koekemoer, E. Medezinski, J. Merten, G. A. Ogrean, P. Tozzi, K. Umetsu, E. Vanzella, R. J. van Weeren, A. Zitrin,

M. Annunziatella, G. B. Caminha, T. Broadhurst, D. Coe, M. Donahue, A. Fritz, B. Frye, D. Kelson, M. Lombardi, C. Maier, M. Meneghetti, A. Monna, M. Postman, M. Scodeggio, S. Seitz, and B. Ziegler. CLASH-VLT: Dissecting the Frontier Fields Galaxy Cluster MACS J0416.1-2403 with 800 Spectra of Member Galaxies. , 224(2):33, June 2016.

[13] J. M. Bardeen, J. R. Bond, N. Kaiser, and A. S. Szalay. The Statistics of Peaks of Gaussian Random Fields. , 304:15, May 1986.

[14] M. Barden, B. Häußler, C. Y. Peng, D. H. McIntosh, and Y. Guo. GALAPAGOS: from pixels to parameters. , 422:449–468, May 2012.

[15] R. Barkana and A. Loeb. In the beginning: the first sources of light and the reionization of the universe. , 349(2):125–238, July 2001.

[16] M. Bartelmann and P. Schneider. Weak gravitational lensing. , 340(4-5):291–472, January 2001.

[17] Róbert Beck, Conor McPartland, Andrew Repp, David Sanders, and István Szapudi. Hawaii Two-0: high-redshift galaxy clustering and bias. , 493(2):2318–2328, April 2020.

[18] S. V. W. Beckwith, M. Stiavelli, A. M. Koekemoer, J. A. R. Caldwell, H. C. Ferguson, R. Hook, R. A. Lucas, L. E. Bergeron, M. Corbin, S. Jogee, N. Panagia, M. Robberto, P. Royle, R. S. Somerville, and M. Sosey. The Hubble Ultra Deep Field. , 132:1729–1755, November 2006.

[19] P. S. Behroozi, R. H. Wechsler, and C. Conroy. The Average Star Formation Histories of Galaxies in Dark Matter Halos from z = 0-8. , 770:57, June 2013.

[20] E. Bertin and S. Arnouts. SExtractor: Software for source extraction. , 117:393–404, June 1996.

[21] E. Bertin and S. Arnouts. SExtractor: Software for source extraction. *Astronomy and Astrophysics Supplement Series*, 117(2):393–404, Jun 1996.

[22] Roger Blandford and Ramesh Narayan. Fermat's Principle, Caustics, and the Classification of Gravitational Lens Images. , 310:568, November 1986.

[23] M. Bradač, P. Schneider, M. Lombardi, and T. Erben. Strong and weak lensing united. I. The combined strong and weak lensing cluster mass reconstruction method. , 437(1):39–48, July 2005.

[24] Maruša Bradač, Kuang-Han Huang, Adriano Fontana, Marco Castellano, Emiliano Merlin, Ricardo Amorín, Austin Hoag, Victoria Strait, Paola Santini, Russell E. Ryan, Stefano Casertano, Brian C. Lemaux, Lori M. Lubin, Kasper B. Schmidt, Tim Schrabback, Tommaso Treu, Anja von der Linden, Charlotte A. Mason, and Xin Wang. Hubble Frontier Field photometric catalogues of Abell 370 and RXC J2248.7-4431: multiwavelength photometry, photometric redshifts, and stellar properties. , 489(1):99–107, October 2019.

[25] Larry Bradley, Brigitta Sipőcz, Thomas Robitaille, Erik Tollerud, Zé Vinícius, Christoph Deil, Kyle Barbary, Tom J Wilson, Ivo Busko, Hans Moritz Günther, Mihai Cara, Simon Conseil, Michael Droettboom, Azalee Bostroem, E. M. Bray, Lars Andersen Bratholm, P. L. Lim, Matt Craig, Geert Barentsen, Sergio Pascual, Axel Donath, Johnny Greco, Gabriel Perren, Wolfgang Kerzendorf, Miguel de Val-Borro, Nadia Dencheva, Leonardo de Albernaz Ferreira, Harrison Souchereau, Francesco D'Eugenio, and Benjamin Alan Weaver. astropy/photutils: v0.7.2, December 2019.

[26] Gabriel B. Brammer, Danilo Marchesini, Ivo Labbé, Lee Spitler, Daniel Lange-Vagle, Elizbeth A. Barker, Masayuki Tanaka, Adriano Fontana, Audrey Galametz, Anna Ferré-Mateu, Tadayuki Kodama, Britt Lundgren, Nicholas Martis, Adam Muzzin, Mauro Stefanon, Sune Toft, Arjen van der Wel, Benedetta Vulcani, and Katherine E. Whitaker. Ultra-deep K $_S$-band Imaging of the Hubble Frontier Fields. *The Astrophysical Journal Supplement Series*, 226(1):6, Sep 2016.

[27] Gabriel B. Brammer, Danilo Marchesini, Ivo Labbé, Lee Spitler, Daniel Lange-Vagle, Elizbeth A. Barker, Masayuki Tanaka, Adriano Fontana, Audrey Galametz, Anna Ferré-Mateu, Tadayuki Kodama, Britt Lundgren, Nicholas Martis, Adam Muzzin, Mauro Stefanon, Sune Toft, Arjen van der Wel, Benedetta Vulcani, and Katherine E. Whitaker. Ultra-deep K $_S$-band Imaging of the Hubble Frontier Fields. , 226(1):6, Sep 2016.

[28] Gabriel B. Brammer, Pieter G. van Dokkum, and Paolo Coppi. EAZY: A Fast, Public Photometric Redshift Code. , 686(2):1503–1513, October 2008.

[29] G. Bruzual and S. Charlot. Stellar population synthesis at the resolution of 2003. , 344:1000–1028, October 2003.

[30] John A. R. Caldwell, Daniel H. McIntosh, Hans-Walter Rix, Marco Barden, Steven V. W. Beckwith, Eric F. Bell, Andrea Borch, Catherine Heymans, Boris Häußler, Knud Jahnke, Shardha Jogee, Klaus Meisenheimer, Chien Y. Peng, Sebastian F. Sánchez, Rachel S. Somerville, Lutz Wisotzki, and Christian Wolf. GEMS Survey Data and Catalog. , 174(1):136–144, January 2008.

[31] Daniela Calzetti, Lee Armus, Ralph C Bohlin, Anne L Kinney, Jan Koornneef, and Thaisa Storchi-Bergmann. The Dust Content and Opacity of Actively Star-forming Galaxies. , 533:682, 2000.

[32] G. B. Caminha, C. Grillo, P. Rosati, I. Balestra, A. Mercurio, E. Vanzella, A. Biviano, K. I. Caputi, C. Delgado-Correal, W. Karman, M. Lombardi, M. Meneghetti, B. Sartoris, and P. Tozzi. A refined mass distribution of the cluster MACS J0416.1-2403 from a new large set of spectroscopic multiply lensed sources. , 600:A90, April 2017.

[33] M. Castellano, R. Amorín, E. Merlin, A. Fontana, R. J. McLure, E. Mármol-Queraltó, A. Mortlock, S. Parsa, J. S. Dunlop, D. Elbaz, I. Balestra, A. Boucaud, N. Bourne, K. Boutsia, G. Brammer, V. A. Bruce, F. Buitrago, P. Capak, N. Cappelluti, L. Ciesla, A. Comastri, F. Cullen, S. Derriere, S. M. Faber, E. Giallongo, A. Grazian, C. Grillo,

A. Mercurio, M. J. Michałowski, M. Nonino, D. Paris, L. Pentericci, S. Pilo, P. Rosati, P. Santini, C. Schreiber, X. Shu, and T. Wang. The ASTRODEEP Frontier Fields catalogues. II. Photometric redshifts and rest frame properties in Abell-2744 and MACS-J0416. , 590:A31, May 2016.

[34] Dan Coe, Keiichi Umetsu, Adi Zitrin, Megan Donahue, Elinor Medezinski, Marc Postman, Mauricio Carrasco, Timo Anguita, Margaret J. Geller, Kenneth J. Rines, Antonaldo Diaferio, Michael J. Kurtz, Larry Bradley, Anton Koekemoer, Wei Zheng, Mario Nonino, Alberto Molino, Andisheh Mahdavi, Doron Lemze, Leopoldo Infante, Sara Ogaz, Peter Melchior, Ole Host, Holland Ford, Claudio Grillo, Piero Rosati, Yolanda Jiménez-Teja, John Moustakas, Tom Broadhurst, Begoña Ascaso, Ofer Lahav, Matthias Bartelmann, Narciso Benítez, Rychard Bouwens, Or Graur, Genevieve Graves, Saurabh Jha, Stephanie Jouvel, Daniel Kelson, Leonidas Moustakas, Dan Maoz, Massimo Meneghetti, Julian Merten, Adam Riess, Steve Rodney, and Stella Seitz. CLASH: Precise New Constraints on the Mass Profile of the Galaxy Cluster A2261. , 757(1):22, September 2012.

[35] Dark Energy Survey Collaboration, T. Abbott, F. B. Abdalla, J. Aleksić, S. Allam, A. Amara, D. Bacon, E. Balbinot, M. Banerji, K. Bechtol, A. Benoit-Lévy, G. M. Bernstein, E. Bertin, J. Blazek, C. Bonnett, S. Bridle, D. Brooks, R. J. Brunner, E. Buckley-Geer, D. L. Burke, G. B. Caminha, D. Capozzi, J. Carlsen, A. Carnero-Rosell, M. Carollo, M. Carrasco-Kind, J. Carretero, F. J. Castander, L. Clerkin, T. Collett, C. Conselice, M. Crocce, C. E. Cunha, C. B. D'Andrea, L. N. da Costa, T. M. Davis, S. Desai, H. T. Diehl, J. P. Dietrich, S. Dodelson, P. Doel, A. Drlica-Wagner, J. Estrada, J. Etherington, A. E. Evrard, J. Fabbri, D. A. Finley, B. Flaugher, R. J. Foley, P. Fosalba, J. Frieman, J. García-Bellido, E. Gaztanaga, D. W. Gerdes, T. Giannantonio, D. A. Goldstein, D. Gruen, R. A. Gruendl, P. Guarnieri, G. Gutierrez, W. Hartley, K. Honscheid, B. Jain, D. J. James, T. Jeltema, S. Jouvel, R. Kessler, A. King, D. Kirk, R. Kron, K. Kuehn, N. Kuropatkin, O. Lahav, T. S. Li, M. Lima, H. Lin, M. A. G. Maia, M. Makler, M. Manera, C. Maraston, J. L. Marshall, P. Martini, R. G. McMahon, P. Melchior, A. Merson, C. J. Miller, R. Miquel, J. J. Mohr, X. Morice-Atkinson, K. Naidoo, E. Neilsen, R. C. Nichol, B. Nord, R. Ogando, F. Ostrovski, A. Palmese, A. Papadopoulos, H. V. Peiris, J. Peoples, W. J. Percival, A. A. Plazas, S. L. Reed, A. Refregier, A. K. Romer, A. Roodman, A. Ross, E. Rozo, E. S. Rykoff, I. Sadeh, M. Sako, C. Sánchez, E. Sanchez, B. Santiago, V. Scarpine, M. Schubnell, I. Sevilla-Noarbe, E. Sheldon, M. Smith, R. C. Smith, M. Soares-Santos, F. Sobreira, M. Soumagnac, E. Suchyta, M. Sullivan, M. Swanson, G. Tarle, J. Thaler, D. Thomas, R. C. Thomas, D. Tucker, J. D. Vieira, V. Vikram, A. R. Walker, R. H. Wechsler, J. Weller, W. Wester, L. Whiteway, H. Wilcox, B. Yanny, Y. Zhang, and J. Zuntz. The Dark Energy Survey: more than dark energy - an overview. , 460(2):1270–1299, August 2016.

[36] I. Davidzon, O. Ilbert, C. Laigle, J. Coupon, H. J. McCracken, I. Delvecchio, D. Masters, P. Capak, B. C. Hsieh, O. Le Fèvre, L. Tresse, M. Bethermin, Y.-Y. Chang, A. L. Faisst, E. Le Floc'h, C. Steinhardt, S. Toft, H. Aussel, C. Dubois, G. Hasinger, M. Salvato, D. B. Sanders, N. Scoville, and J. D. Silverman. The COSMOS2015

galaxy stellar mass function . Thirteen billion years of stellar mass assembly in ten snapshots. , 605:A70, September 2017.

[37] C. De Santis, A. Grazian, A. Fontana, and P. Santini. ConvPhot: A profile-matching algorithm for precision photometry. , 12:271–288, February 2007.

[38] DESI Collaboration, Amir Aghamousa, Jessica Aguilar, Steve Ahlen, Shadab Alam, Lori E. Allen, Carlos Allende Prieto, James Annis, Stephen Bailey, Christophe Balland, Otger Ballester, Charles Baltay, Lucas Beaufore, Chris Bebek, Timothy C. Beers, Eric F. Bell, José Luis Bernal, Robert Besuner, Florian Beutler, Chris Blake, Hannes Bleuler, Michael Blomqvist, Robert Blum, Adam S. Bolton, Cesar Briceno, David Brooks, Joel R. Brownstein, Elizabeth Buckley-Geer, Angela Burden, Etienne Burtin, Nicolas G. Busca, Robert N. Cahn, Yan-Chuan Cai, Laia Cardiel-Sas, Raymond G. Carlberg, Pierre-Henri Carton, Ricard Casas, Francisco J. Castander, Jorge L. Cervantes-Cota, Todd M. Claybaugh, Madeline Close, Carl T. Coker, Shaun Cole, Johan Comparat, Andrew P. Cooper, M. C. Cousinou, Martin Crocce, Jean-Gabriel Cuby, Daniel P. Cunningham, Tamara M. Davis, Kyle S. Dawson, Axel de la Macorra, Juan De Vicente, Timothée Delubac, Mark Derwent, Arjun Dey, Govinda Dhungana, Zhejie Ding, Peter Doel, Yutong T. Duan, Anne Ealet, Jerry Edelstein, Sarah Eftekharzadeh, Daniel J. Eisenstein, Ann Elliott, Stéphanie Escoffier, Matthew Evatt, Parker Fagrelius, Xiaohui Fan, Kevin Fanning, Arya Farahi, Jay Farihi, Ginevra Favole, Yu Feng, Enrique Fernandez, Joseph R. Findlay, Douglas P. Finkbeiner, Michael J. Fitzpatrick, Brenna Flaugher, Samuel Flender, Andreu Font-Ribera, Jaime E. Forero-Romero, Pablo Fosalba, Carlos S. Frenk, Michele Fumagalli, Boris T. Gaensicke, Giuseppe Gallo, Juan Garcia-Bellido, Enrique Gaztanaga, Nicola Pietro Gentile Fusillo, Terry Gerard, Irena Gershkovich, Tommaso Giannantonio, Denis Gillet, Guillermo Gonzalez-de-Rivera, Violeta Gonzalez-Perez, Shelby Gott, Or Graur, Gaston Gutierrez, Julien Guy, Salman Habib, Henry Heetderks, Ian Heetderks, Katrin Heitmann, Wojciech A. Hellwing, David A. Herrera, Shirley Ho, Stephen Holland, Klaus Honscheid, Eric Huff, Timothy A. Hutchinson, Dragan Huterer, Ho Seong Hwang, Joseph Maria Illa Laguna, Yuzo Ishikawa, Dianna Jacobs, Niall Jeffrey, Patrick Jelinsky, Elise Jennings, Linhua Jiang, Jorge Jimenez, Jennifer Johnson, Richard Joyce, Eric Jullo, Stéphanie Juneau, Sami Kama, Armin Karcher, Sonia Karkar, Robert Kehoe, Noble Kennamer, Stephen Kent, Martin Kilbinger, Alex G. Kim, David Kirkby, Theodore Kisner, Ellie Kitanidis, Jean-Paul Kneib, Sergey Koposov, Eve Kovacs, Kazuya Koyama, Anthony Kremin, Richard Kron, Luzius Kronig, Andrea Kueter-Young, Cedric G. Lacey, Robin Lafever, Ofer Lahav, Andrew Lambert, Michael Lampton, Martin Landriau, Dustin Lang, Tod R. Lauer, Jean-Marc Le Goff, Laurent Le Guillou, Auguste Le Van Suu, Jae Hyeon Lee, Su-Jeong Lee, Daniela Leitner, Michael Lesser, Michael E. Levi, Benjamin L'Huillier, Baojiu Li, Ming Liang, Huan Lin, Eric Linder, Sarah R. Loebman, Zarija Lukić, Jun Ma, Niall MacCrann, Christophe Magneville, Laleh Makarem, Marc Manera, Christopher J. Manser, Robert Marshall, Paul Martini, Richard Massey, Thomas Matheson, Jeremy McCauley, Patrick McDonald, Ian D. McGreer, Aaron Meisner, Nigel Metcalfe, Timothy N. Miller, Ramon Miquel, John Moustakas, Adam Myers, Milind Naik, Jeffrey A.

Newman, Robert C. Nichol, Andrina Nicola, Luiz Nicolati da Costa, Jundan Nie, Gustavo Niz, Peder Norberg, Brian Nord, Dara Norman, Peter Nugent, Thomas O'Brien, Minji Oh, Knut A. G. Olsen, Cristobal Padilla, Hamsa Padmanabhan, Nikhil Padmanabhan, Nathalie Palanque-Delabrouille, Antonella Palmese, Daniel Pappalardo, Isabelle Pâris, Changbom Park, Anna Patej, John A. Peacock, Hiranya V. Peiris, Xiyan Peng, Will J. Percival, Sandrine Perruchot, Matthew M. Pieri, Richard Pogge, Jennifer E. Pollack, Claire Poppett, Francisco Prada, Abhishek Prakash, Ronald G. Probst, David Rabinowitz, Anand Raichoor, Chang Hee Ree, Alexandre Refregier, Xavier Regal, Beth Reid, Kevin Reil, Mehdi Rezaie, Constance M. Rockosi, Natalie Roe, Samuel Ronayette, Aaron Roodman, Ashley J. Ross, Nicholas P. Ross, Graziano Rossi, Eduardo Rozo, Vanina Ruhlmann-Kleider, Eli S. Rykoff, Cristiano Sabiu, Lado Samushia, Eusebio Sanchez, Javier Sanchez, David J. Schlegel, Michael Schneider, Michael Schubnell, Aurélia Secroun, Uros Seljak, Hee-Jong Seo, Santiago Serrano, Arman Shafieloo, Huanyuan Shan, Ray Sharples, Michael J. Sholl, William V. Shourt, Joseph H. Silber, David R. Silva, Martin M. Sirk, Anze Slosar, Alex Smith, George F. Smoot, Debopam Som, Yong-Seon Song, David Sprayberry, Ryan Staten, Andy Stefanik, Gregory Tarle, Suk Sien Tie, Jeremy L. Tinker, Rita Tojeiro, Francisco Valdes, Octavio Valenzuela, Monica Valluri, Mariana Vargas-Magana, Licia Verde, Alistair R. Walker, Jiali Wang, Yuting Wang, Benjamin A. Weaver, Curtis Weaverdyck, Risa H. Wechsler, David H. Weinberg, Martin White, Qian Yang, Christophe Yeche, Tianmeng Zhang, Gong-Bo Zhao, Yi Zheng, Xu Zhou, Zhimin Zhou, Yaling Zhu, Hu Zou, and Ying Zu. The DESI Experiment Part I: Science,Targeting, and Survey Design. *arXiv e-prints*, page arXiv:1611.00036, October 2016.

[39] Vincent Desjacques, Donghui Jeong, and Fabian Schmidt. Large-scale galaxy bias. , 733:1–193, February 2018.

[40] M. Di Criscienzo, E. Merlin, M. Castellano, P. Santini, A. Fontana, R. Amorin, K. Boutsia, S. Derriere, J. S. Dunlop, D. Elbaz, A. Grazian, R. J. McLure, E. Mármol-Queraltó, M. J. Michalowski, S. Mortlock, S. Parsa, and L. Pentericci. The ASTRODEEP Frontier Fields catalogues. III. Multiwavelength photometry and rest-frame properties of MACS-J0717 and MACS-J1149. , 607:A30, October 2017.

[41] J. M. Diego, M. Tegmark, P. Protopapas, and H. B. Sandvik. Combined reconstruction of weak and strong lensing data with WSLAP. , 375(3):958–970, March 2007.

[42] Jose M. Diego, T. Broadhurst, N. Benitez, K. Umetsu, D. Coe, I. Sendra, M. Sereno, L. Izzo, and G. Covone. A free-form lensing grid solution for A1689 with new multiple images. , 446(1):683–704, January 2015.

[43] E. Diolaiti, O. Bendinelli, D. Bonaccini, L. M. Close, D. G. Currie, and G. Parmeggiani. StarFinder: an IDL GUI-based code to analyze crowded fields with isoplanatic correcting PSF fitting. In P. L. Wizinowich, editor, *Adaptive Optical Systems Technology*, volume 4007 of , pages 879–888, July 2000.

[44] A. Durkalec, O. Le Fèvre, A. Pollo, S. de la Torre, P. Cassata, B. Garilli, V. Le Brun, B. C. Lemaux, D. Maccagni, L. Pentericci, L. A. M. Tasca, R. Thomas,

E. Vanzella, G. Zamorani, E. Zucca, R. Amorín, S. Bardelli, L. P. Cassarà, M. Castellano, A. Cimatti, O. Cucciati, A. Fontana, M. Giavalisco, A. Grazian, N. P. Hathi, O. Ilbert, S. Paltani, B. Ribeiro, D. Schaerer, M. Scodeggio, V. Sommariva, M. Talia, L. Tresse, D. Vergani, P. Capak, S. Charlot, T. Contini, J. G. Cuby, J. Dunlop, S. Fotopoulou, A. Koekemoer, C. López-Sanjuan, Y. Mellier, J. Pforr, M. Salvato, N. Scoville, Y. Taniguchi, and P. W. Wang. Evolution of clustering length, large-scale bias, and host halo mass at 2 ¡ z ¡ 5 in the VIMOS Ultra Deep Survey (VUDS)⋆. , 583:A128, November 2015.

[45] Harald Ebeling, Cheng-Jiun Ma, and Elizabeth Barrett. Spectroscopic Redshifts of Galaxies within the Frontier Fields. , 211(2):21, April 2014.

[46] G. G. Fazio, J. L. Hora, L. E. Allen, M. L. N. Ashby, P. Barmby, L. K. Deutsch, J. S. Huang, S. Kleiner, M. Marengo, S. T. Megeath, G. J. Melnick, M. A. Pahre, B. M. Patten, J. Polizotti, H. A. Smith, R. S. Taylor, Z. Wang, S. P. Willner, W. F. Hoffmann, J. L. Pipher, W. J. Forrest, C. W. McMurty, C. R. McCreight, M. E. McKelvey, R. E. McMurray, D. G. Koch, S. H. Moseley, R. G. Arendt, J. E. Mentzell, C. T. Marx, P. Losch, P. Mayman, W. Eichhorn, D. Krebs, M. Jhabvala, D. Y. Gezari, D. J. Fixsen, J. Flores, K. Shakoorzadeh, R. Jungo, C. Hakun, L. Workman, G. Karpati, R. Kichak, R. Whitley, S. Mann, E. V. Tollestrup, P. Eisenhardt, D. Stern, V. Gorjian, B. Bhattacharya, S. Carey, B. O. Nelson, W. J. Glaccum, M. Lacy, P. J. Lowrance, S. Laine, W. T. Reach, J. A. Stauffer, J. A. Surace, G. Wilson, E. L. Wright, A. Hoffman, G. Domingo, and M. Cohen. The Infrared Array Camera (IRAC) for the Spitzer Space Telescope. , 154(1):10–17, September 2004.

[47] Steven L. Finkelstein, Jr. Ryan, Russell E., Casey Papovich, Mark Dickinson, Mimi Song, Rachel S. Somerville, Henry C. Ferguson, Brett Salmon, Mauro Giavalisco, Anton M. Koekemoer, Matthew L. N. Ashby, Peter Behroozi, Marco Castellano, James S. Dunlop, Sandy M. Faber, Giovanni G. Fazio, Adriano Fontana, Norman A. Grogin, Nimish Hathi, Jason Jaacks, Dale D. Kocevski, Rachael Livermore, Ross J. McLure, Emiliano Merlin, Bahram Mobasher, Jeffrey A. Newman, Marc Rafelski, Vithal Tilvi, and S. P. Willner. The Evolution of the Galaxy Rest-frame Ultraviolet Luminosity Function over the First Two Billion Years. , 810(1):71, September 2015.

[48] B. Flaugher, H. T. Diehl, K. Honscheid, T. M. C. Abbott, O. Alvarez, R. Angstadt, J. T. Annis, M. Antonik, O. Ballester, L. Beaufore, G. M. Bernstein, R. A. Bernstein, B. Bigelow, M. Bonati, D. Boprie, D. Brooks, E. J. Buckley-Geer, J. Campa, L. Cardiel-Sas, F. J. Castander, J. Castilla, H. Cease, J. M. Cela-Ruiz, S. Chappa, E. Chi, C. Cooper, L. N. da Costa, E. Dede, G. Derylo, D. L. DePoy, J. de Vicente, P. Doel, A. Drlica-Wagner, J. Eiting, A. E. Elliott, J. Emes, J. Estrada, A. Fausti Neto, D. A. Finley, R. Flores, J. Frieman, D. Gerdes, M. D. Gladders, B. Gregory, G. R. Gutierrez, J. Hao, S. E. Holland, S. Holm, D. Huffman, C. Jackson, D. J. James, M. Jonas, A. Karcher, I. Karliner, S. Kent, R. Kessler, M. Kozlovsky, R. G. Kron, D. Kubik, K. Kuehn, S. Kuhlmann, K. Kuk, O. Lahav, A. Lathrop, J. Lee, M. E. Levi, P. Lewis, T. S. Li, I. Mandrichenko, J. L. Marshall, G. Martinez, K. W. Merritt, R. Miquel, F. Muñoz, E. H. Neilsen, R. C. Nichol, B. Nord, R. Ogando, J. Olsen,

N. Palaio, K. Patton, J. Peoples, A. A. Plazas, J. Rauch, K. Reil, J. P. Rheault, N. A. Roe, H. Rogers, A. Roodman, E. Sanchez, V. Scarpine, R. H. Schindler, R. Schmidt, R. Schmitt, M. Schubnell, K. Schultz, P. Schurter, L. Scott, S. Serrano, T. M. Shaw, R. C. Smith, M. Soares-Santos, A. Stefanik, W. Stuermer, E. Suchyta, A. Sypniewski, G. Tarle, J. Thaler, R. Tighe, C. Tran, D. Tucker, A. R. Walker, G. Wang, M. Watson, C. Weaverdyck, W. Wester, R. Woods, B. Yanny, and DES Collaboration. The Dark Energy Camera. , 150(5):150, November 2015.

[49] Daniel Foreman-Mackey, David W. Hogg, Dustin Lang, and Jonathan Goodman. emcee: The MCMC Hammer. , 125(925):306, March 2013.

[50] Lukas J. Furtak, Hakim Atek, Matthew D. Lehnert, Jacopo Chevallard, and Stéphane Charlot. How robustly can we constrain the low-mass end of the z $\sim$ 6-7 stellar mass function? The limits of lensing models and stellar population assumptions in the Hubble Frontier Fields. , 501(2):1568–1590, February 2021.

[51] Lukas J. Furtak, Hakim Atek, Matthew D. Lehnert, Jacopo Chevallard, and Stéphane Charlot. How robustly can we constrain the low-mass end of the z $\sim$ 6-7 stellar mass function? The limits of lensing models and stellar population assumptions in the Hubble Frontier Fields. , 501(2):1568–1590, February 2021.

[52] A. Galametz, A. Grazian, A. Fontana, H. C. Ferguson, M. L. N. Ashby, G. Barro, M. Castellano, T. Dahlen, J. L. Donley, S. M. Faber, N. Grogin, Y. Guo, K.-H. Huang, D. D. Kocevski, A. M. Koekemoer, K.-S. Lee, E. J. McGrath, M. Peth, S. P. Willner, O. Almaini, M. Cooper, A. Cooray, C. J. Conselice, M. Dickinson, J. S. Dunlop, G. G. Fazio, S. Foucaud, J. P. Gardner, M. Giavalisco, N. P. Hathi, W. G. Hartley, D. C. Koo, K. Lai, D. F. de Mello, R. J. McLure, R. A. Lucas, D. Paris, L. Pentericci, P. Santini, C. Simpson, V. Sommariva, T. Targett, B. J. Weiner, S. Wuyts, and the CANDELS Team. CANDELS Multiwavelength Catalogs: Source Identification and Photometry in the CANDELS UKIDSS Ultra-deep Survey Field. , 206:10, June 2013.

[53] M. Galametz, S. C. Madden, F. Galliano, S. Hony, G. J. Bendo, and M. Sauvage. Probing the dust properties of galaxies up to submillimetre wavelengths. II. Dust-to-gas mass ratio trends with metallicity and the submm excess in dwarf galaxies. , 532:A56, August 2011.

[54] M. Garcia-Fernandez, E. Sanchez, I. Sevilla-Noarbe, E. Suchyta, E. M. Huff, E. Gaztanaga, Aleksić, J. , R. Ponce, F. J. Castander, B. Hoyle, T. M. C. Abbott, F. B. Abdalla, S. Allam, J. Annis, A. Benoit-Lévy, G. M. Bernstein, E. Bertin, D. Brooks, E. Buckley-Geer, D. L. Burke, A. Carnero Rosell, M. Carrasco Kind, J. Carretero, M. Crocce, C. E. Cunha, C. B. D'Andrea, L. N. da Costa, D. L. DePoy, S. Desai, H. T. Diehl, T. F. Eifler, A. E. Evrard, E. Fernandez, B. Flaugher, P. Fosalba, J. Frieman, J. García-Bellido, D. W. Gerdes, T. Giannantonio, D. Gruen, R. A. Gruendl, J. Gschwend, G. Gutierrez, D. J. James, M. Jarvis, D. Kirk, E. Krause, K. Kuehn, N. Kuropatkin, O. Lahav, M. Lima, N. MacCrann, M. A. G. Maia, M. March, J. L. Marshall, P. Melchior, R. Miquel, J. J. Mohr, A. A. Plazas, A. K. Romer, A. Roodman, E. S. Rykoff, V. Scarpine, M. Schubnell, R. C. Smith, M. Soares-Santos, F. Sobreira,

G. Tarle, D. Thomas, A. R. Walker, W. Wester, and DES Collaboration. Weak lensing magnification in the Dark Energy Survey Science Verification data. , 476(1):1071–1085, May 2018.

[55] Eric Gawiser, Harold Francke, Kamson Lai, Kevin Schawinski, Caryl Gronwall, Robin Ciardullo, Ryan Quadri, Alvaro Orsi, L. Felipe Barrientos, Guillermo A. Blanc, Giovanni Fazio, John J. Feldmeier, Jia-sheng Huang, Leopoldo Infante, Paulina Lira, Nelson Padilla, Edward N. Taylor, Ezequiel Treister, C. Megan Urry, Pieter G. van Dokkum, and Shanil N. Virani. Lyα-Emitting Galaxies at z = 3.1: L* Progenitors Experiencing Rapid Star Formation. , 671(1):278–284, December 2007.

[56] S. Gonzaga and et al. *The DrizzlePac Handbook*. 2012.

[57] Meghan E. Gray, Christian Wolf, Marco Barden, Chien Y. Peng, Boris Häußler, Eric F. Bell, Daniel H. McIntosh, Yicheng Guo, John A. R. Caldwell, David Bacon, Michael Balogh, Fabio D. Barazza, Asmus Böhm, Catherine Heymans, Knud Jahnke, Shardha Jogee, Eelco Van Kampen, Kyle Lane, Klaus Meisenheimer, Sebastian F. Sánchez, Andy Taylor, Lutz Wisotzki, Xianzhong Zheng, David A. Green, R. J. Beswick, D. J. Saikia, Rachel Gilmour, Benjamin D. Johnson, and Casey Papovich. STAGES: the Space Telescope A901/2 Galaxy Evolution Survey. *Monthly Notices of the Royal Astronomical Society*, 393(4):1275–1301, 02 2009.

[58] E. Gross. Practical Statistics for High Energy Physics. *CERN Yellow Rep. School Proc.*, 3:199–221, 2018.

[59] E. J. Groth and P. J. E. Peebles. Statistical analysis of catalogs of extragalactic objects. VII. Two- and three-point correlation functions for the high-resolution Shane-Wirtanen catalog of galaxies. , 217:385–405, October 1977.

[60] B. Häußler, S. P. Bamford, M. Vika, A. L. Rojas, M. Barden, L. S. Kelvin, M. Alpaslan, A. S. G. Robotham, S. P. Driver, I. K. Baldry, S. Brough, A. M. Hopkins, J. Liske, R. C. Nichol, C. C. Popescu, and R. J. Tuffs. MegaMorph - multiwavelength measurement of galaxy structure: complete Sérsic profile information from modern surveys. , 430:330–369, March 2013.

[61] Catherine Heymans, Tilman Tröster, Marika Asgari, Chris Blake, Hendrik Hildebrandt, Benjamin Joachimi, Konrad Kuijken, Chieh-An Lin, Ariel G. Sánchez, Jan Luca van den Busch, Angus H. Wright, Alexandra Amon, Maciej Bilicki, Jelte de Jong, Martin Crocce, Andrej Dvornik, Thomas Erben, Maria Cristina Fortuna, Fedor Getman, Benjamin Giblin, Karl Glazebrook, Henk Hoekstra, Shahab Joudaki, Arun Kannawadi, Fabian Köhlinger, Chris Lidman, Lance Miller, Nicola R. Napolitano, David Parkinson, Peter Schneider, HuanYuan Shan, Edwin A. Valentijn, Gijs Verdoes Kleijn, and Christian Wolf. KiDS-1000 Cosmology: Multi-probe weak gravitational lensing and spectroscopic galaxy clustering constraints. , 646:A140, February 2021.

[62] Chiaki Hikage, Masamune Oguri, Takashi Hamana, Surhud More, Rachel Mandelbaum, Masahiro Takada, Fabian Köhlinger, Hironao Miyatake, Atsushi J. Nishizawa,

Hiroaki Aihara, Robert Armstrong, James Bosch, Jean Coupon, Anne Ducout, Paul Ho, Bau-Ching Hsieh, Yutaka Komiyama, François Lanusse, Alexie Leauthaud, Robert H. Lupton, Elinor Medezinski, Sogo Mineo, Shoken Miyama, Satoshi Miyazaki, Ryoma Murata, Hitoshi Murayama, Masato Shirasaki, Cristóbal Sifón, Melanie Simet, Joshua Speagle, David N. Spergel, Michael A. Strauss, Naoshi Sugiyama, Masayuki Tanaka, Yousuke Utsumi, Shiang-Yu Wang, and Yoshihiko Yamada. Cosmology from cosmic shear power spectra with Subaru Hyper Suprime-Cam first-year data. , 71(2):43, April 2019.

[63] A. Hoag, K. H. Huang, T. Treu, M. Bradač, K. B. Schmidt, X. Wang, G. B. Brammer, A. Broussard, R. Amorin, M. Castellano, A. Fontana, E. Merlin, T. Schrabback, M. Trenti, and B. Vulcani. The Grism Lens-Amplified Survey from Space (GLASS). VI. Comparing the Mass and Light in MACS J0416.1-2403 Using Frontier Field Imaging and GLASS Spectroscopy. , 831(2):182, November 2016.

[64] D. C. Hoaglin, F. Mosteller, and J. W. Tukey. *Understanding robust and exploratory data anlysis*. 1983.

[65] Carlos Hoyos, Alfonso Aragón-Salamanca, Meghan E. Gray, David T. Maltby, Eric F. Bell, Fabio D. Barazza, Asmus Böhm, Boris Häußler, Knud Jahnke, Shardha Jogee, Kyle P. Lane, Daniel H. McIntosh, and Christian Wolf. A new automatic method to identify galaxy mergers - I. Description and application to the Space Telescope A901/902 Galaxy Evolution Survey. , 419(3):2703–2724, Jan 2012.

[66] O Ilbert, S Arnouts, H J McCracken, M Bolzonella, E Bertin, O Le Fèvre, Y Mellier, G Zamorani, R Pellò, A Iovino, L Tresse, V Le Brun, D Bottini, B Garilli, D Maccagni, J P Picat, R Scaramella, M Scodeggio, G Vettolani, A Zanichelli, C Adami, S Bardelli, A Cappi, S Charlot, P Ciliegi, T Contini, O Cucciati, S Foucaud, P Franzetti, I Gavignaud, L Guzzo, B Marano, C Marinoni, A Mazure, B Meneux, R Merighi, S Paltani, A Pollo, L Pozzetti, M Radovich, E Zucca, M Bondi, A Bongiorno, G Busarello, S de la Torre, L Gregorini, F Lamareille, G Mathez, P Merluzzi, V Ripepi, D Rizzo, and D Vergani. Accurate photometric redshifts for the CFHT legacy survey calibrated using the VIMOS VLT deep survey. , 457(3):841–856, 2006.

[67] O. Ilbert, S. Arnouts, H. J. McCracken, M. Bolzonella, E. Bertin, O. Le Fèvre, Y. Mellier, G. Zamorani, R. Pellò, A. Iovino, L. Tresse, V. Le Brun, D. Bottini, B. Garilli, D. Maccagni, J. P. Picat, R. Scaramella, M. Scodeggio, G. Vettolani, A. Zanichelli, C. Adami, S. Bardelli, A. Cappi, S. Charlot, P. Ciliegi, T. Contini, O. Cucciati, S. Foucaud, P. Franzetti, I. Gavignaud, L. Guzzo, B. Marano, C. Marinoni, A. Mazure, B. Meneux, R. Merighi, S. Paltani, A. Pollo, L. Pozzetti, M. Radovich, E. Zucca, M. Bondi, A. Bongiorno, G. Busarello, S. de La Torre, L. Gregorini, F. Lamareille, G. Mathez, P. Merluzzi, V. Ripepi, D. Rizzo, and D. Vergani. Accurate photometric redshifts for the CFHT legacy survey calibrated using the VIMOS VLT deep survey. , 457(3):841–856, October 2006.

[68] O Ilbert, P Capak, M Salvato, H Aussel, H J McCracken, D B Sanders, N Scoville, J Kartaltepe, S Arnouts, E Le Floc'h, B Mobasher, Y Taniguchi, F Lamareille,

A Leauthaud, S Sasaki, D Thompson, M Zamojski, G Zamorani, S Bardelli, M Bolzonella, A Bongiorno, M Brusa, K I Caputi, C M Carollo, T Contini, R Cook, G Coppa, O Cucciati, S de la Torre, L De Ravel, P Franzetti, B Garilli, G Hasinger, A Iovino, P Kampczyk, J-P Kneib, C Knobel, K Kovac, J F Le Borgne, V Le Brun, O Le Fèvre, S Lilly, D Looper, C Maier, V Mainieri, Y Mellier, M Mignoli, T Murayama, R Pellò, Y Peng, E Perez-Montero, A Renzini, E Ricciardelli, D Schiminovich, M Scodeggio, Y Shioya, J Silverman, J Surace, M Tanaka, L Tasca, L Tresse, D Vergani, and E Zucca. Cosmos Photometric Redshifts with 30-Bands for 2-deg2. , 690(2):1236–1249, 2009.

[69] Ž. Ivezić, A.J. Connolly, J.T. Vanderplas, and A. Gray. *Statistics, Data Mining and Machine Learning in Astronomy.* Princeton University Press, 2014.

[70] Željko Ivezić, Steven M. Kahn, J. Anthony Tyson, Bob Abel, Emily Acosta, Robyn Allsman, David Alonso, Yusra AlSayyad, Scott F. Anderson, John Andrew, James Roger P. Angel, George Z. Angeli, Reza Ansari, Pierre Antilogus, Constanza Araujo, Robert Armstrong, Kirk T. Arndt, Pierre Astier, Éric Aubourg, Nicole Auza, Tim S. Axelrod, Deborah J. Bard, Jeff D. Barr, Aurelian Barrau, James G. Bartlett, Amanda E. Bauer, Brian J. Bauman, Sylvain Baumont, Ellen Bechtol, Keith Bechtol, Andrew C. Becker, Jacek Becla, Cristina Beldica, Steve Bellavia, Federica B. Bianco, Rahul Biswas, Guillaume Blanc, Jonathan Blazek, Roger D. Blandford, Josh S. Bloom, Joanne Bogart, Tim W. Bond, Michael T. Booth, Anders W. Borgland, Kirk Borne, James F. Bosch, Dominique Boutigny, Craig A. Brackett, Andrew Bradshaw, William Nielsen Brandt, Michael E. Brown, James S. Bullock, Patricia Burchat, David L. Burke, Gianpietro Cagnoli, Daniel Calabrese, Shawn Callahan, Alice L. Callen, Jeffrey L. Carlin, Erin L. Carlson, Srinivasan Chandrasekharan, Glenaver Charles-Emerson, Steve Chesley, Elliott C. Cheu, Hsin-Fang Chiang, James Chiang, Carol Chirino, Derek Chow, David R. Ciardi, Charles F. Claver, Johann Cohen-Tanugi, Joseph J. Cockrum, Rebecca Coles, Andrew J. Connolly, Kem H. Cook, Asantha Cooray, Kevin R. Covey, Chris Cribbs, Wei Cui, Roc Cutri, Philip N. Daly, Scott F. Daniel, Felipe Daruich, Guillaume Daubard, Greg Daues, William Dawson, Francisco Delgado, Alfred Dellapenna, Robert de Peyster, Miguel de Val-Borro, Seth W. Digel, Peter Doherty, Richard Dubois, Gregory P. Dubois-Felsmann, Josef Durech, Frossie Economou, Tim Eifler, Michael Eracleous, Benjamin L. Emmons, Angelo Fausti Neto, Henry Ferguson, Enrique Figueroa, Merlin Fisher-Levine, Warren Focke, Michael D. Foss, James Frank, Michael D. Freemon, Emmanuel Gangler, Eric Gawiser, John C. Geary, Perry Gee, Marla Geha, Charles J. B. Gessner, Robert R. Gibson, D. Kirk Gilmore, Thomas Glanzman, William Glick, Tatiana Goldina, Daniel A. Goldstein, Iain Goodenow, Melissa L. Graham, William J. Gressler, Philippe Gris, Leanne P. Guy, Augustin Guyonnet, Gunther Haller, Ron Harris, Patrick A. Hascall, Justine Haupt, Fabio Hernandez, Sven Herrmann, Edward Hileman, Joshua Hoblitt, John A. Hodgson, Craig Hogan, James D. Howard, Dajun Huang, Michael E. Huffer, Patrick Ingraham, Walter R. Innes, Suzanne H. Jacoby, Bhuvnesh Jain, Fabrice Jammes, M. James Jee, Tim Jenness, Garrett Jernigan, Darko Jevremović, Kenneth Johns, Anthony S. Johnson, Margaret W. G. Johnson, R. Lynne

Jones, Claire Juramy-Gilles, Mario Jurić, Jason S. Kalirai, Nitya J. Kallivayalil, Bryce Kalmbach, Jeffrey P. Kantor, Pierre Karst, Mansi M. Kasliwal, Heather Kelly, Richard Kessler, Veronica Kinnison, David Kirkby, Lloyd Knox, Ivan V. Kotov, Victor L. Krabbendam, K. Simon Krughoff, Petr Kubánek, John Kuczewski, Shri Kulkarni, John Ku, Nadine R. Kurita, Craig S. Lage, Ron Lambert, Travis Lange, J. Brian Langton, Laurent Le Guillou, Deborah Levine, Ming Liang, Kian-Tat Lim, Chris J. Lintott, Kevin E. Long, Margaux Lopez, Paul J. Lotz, Robert H. Lupton, Nate B. Lust, Lauren A. MacArthur, Ashish Mahabal, Rachel Mandelbaum, Thomas W. Markiewicz, Darren S. Marsh, Philip J. Marshall, Stuart Marshall, Morgan May, Robert McKercher, Michelle McQueen, Joshua Meyers, Myriam Migliore, Michelle Miller, David J. Mills, Connor Miraval, Joachim Moeyens, Fred E. Moolekamp, David G. Monet, Marc Moniez, Serge Monkewitz, Christopher Montgomery, Christopher B. Morrison, Fritz Mueller, Gary P. Muller, Freddy Muñoz Arancibia, Douglas R. Neill, Scott P. Newbry, Jean-Yves Nief, Andrei Nomerotski, Martin Nordby, Paul O'Connor, John Oliver, Scot S. Olivier, Knut Olsen, William O'Mullane, Sandra Ortiz, Shawn Osier, Russell E. Owen, Reynald Pain, Paul E. Palecek, John K. Parejko, James B. Parsons, Nathan M. Pease, J. Matt Peterson, John R. Peterson, Donald L. Petravick, M. E. Libby Petrick, Cathy E. Petry, Francesco Pierfederici, Stephen Pietrowicz, Rob Pike, Philip A. Pinto, Raymond Plante, Stephen Plate, Joel P. Plutchak, Paul A. Price, Michael Prouza, Veljko Radeka, Jayadev Rajagopal, Andrew P. Rasmussen, Nicolas Regnault, Kevin A. Reil, David J. Reiss, Michael A. Reuter, Stephen T. Ridgway, Vincent J. Riot, Steve Ritz, Sean Robinson, William Roby, Aaron Roodman, Wayne Rosing, Cecille Roucelle, Matthew R. Rumore, Stefano Russo, Abhijit Saha, Benoit Sassolas, Terry L. Schalk, Pim Schellart, Rafe H. Schindler, Samuel Schmidt, Donald P. Schneider, Michael D. Schneider, William Schoening, German Schumacher, Megan E. Schwamb, Jacques Sebag, Brian Selvy, Glenn H. Sembroski, Lynn G. Seppala, Andrew Serio, Eduardo Serrano, Richard A. Shaw, Ian Shipsey, Jonathan Sick, Nicole Silvestri, Colin T. Slater, J. Allyn Smith, R. Chris Smith, Shahram Sobhani, Christine Soldahl, Lisa Storrie-Lombardi, Edward Stover, Michael A. Strauss, Rachel A. Street, Christopher W. Stubbs, Ian S. Sullivan, Donald Sweeney, John D. Swinbank, Alexander Szalay, Peter Takacs, Stephen A. Tether, Jon J. Thaler, John Gregg Thayer, Sandrine Thomas, Adam J. Thornton, Vaikunth Thukral, Jeffrey Tice, David E. Trilling, Max Turri, Richard Van Berg, Daniel Vanden Berk, Kurt Vetter, Francoise Virieux, Tomislav Vucina, William Wahl, Lucianne Walkowicz, Brian Walsh, Christopher W. Walter, Daniel L. Wang, Shin-Yawn Wang, Michael Warner, Oliver Wiecha, Beth Willman, Scott E. Winters, David Wittman, Sidney C. Wolff, W. Michael Wood-Vasey, Xiuqin Wu, Bo Xin, Peter Yoachim, and Hu Zhan. LSST: From Science Drivers to Reference Design and Anticipated Data Products. , 873(2):111, March 2019.

[71] M. Jarvis, G. Bernstein, and B. Jain. The skewness of the aperture mass statistic. , 352(1):338–352, July 2004.

[72] M. Jauzac, B. Clément, M. Limousin, J. Richard, E. Jullo, H. Ebeling, H. Atek, J. P. Kneib, K. Knowles, P. Natarajan, D. Eckert, E. Egami, R. Massey, and M. Rexroth.

Hubble Frontier Fields: a high-precision strong-lensing analysis of galaxy cluster MACSJ0416.1-2403 using ∼200 multiple images. , 443(2):1549–1554, September 2014.

[73] M. Jauzac, B. Clément, M. Limousin, J. Richard, E. Jullo, H. Ebeling, H. Atek, J. P. Kneib, K. Knowles, P. Natarajan, D. Eckert, E. Egami, R. Massey, and M. Rexroth. Hubble Frontier Fields: a high-precision strong-lensing analysis of galaxy cluster MACSJ0416.1-2403 using ∼200 multiple images. , 443(2):1549–1554, September 2014.

[74] Traci L. Johnson, Keren Sharon, Matthew B. Bayliss, Michael D. Gladders, Dan Coe, and Harald Ebeling. Lens Models and Magnification Maps of the Six Hubble Frontier Fields Clusters. , 797(1):48, December 2014.

[75] E. Jullo, J. P. Kneib, M. Limousin, Á. Elíasdóttir, P. J. Marshall, and T. Verdugo. A Bayesian approach to strong lensing modelling of galaxy clusters. *New Journal of Physics*, 9(12):447, December 2007.

[76] N. Kaiser. On the spatial correlations of Abell clusters. , 284:L9–L12, September 1984.

[77] GM Kaufman. Report no. 6710, center for operations research and econometrics. 1967.

[78] Ryota Kawamata, Masafumi Ishigaki, Kazuhiro Shimasaku, Masamune Oguri, Masami Ouchi, and Shingo Tanigawa. Size-Luminosity Relations and UV Luminosity Functions at z = 6-9 Simultaneously Derived from the Complete Hubble Frontier Fields Data. , 855(1):4, March 2018.

[79] Ryota Kawamata, Masafumi Ishigaki, Kazuhiro Shimasaku, Masamune Oguri, Masami Ouchi, and Shingo Tanigawa. Size-Luminosity Relations and UV Luminosity Functions at z = 6-9 Simultaneously Derived from the Complete Hubble Frontier Fields Data. , 855(1):4, March 2018.

[80] A. A. Khostovan, D. Sobral, B. Mobasher, J. Matthee, R. K. Cochrane, N. Chartab, M. Jafariyazani, A. Paulino-Afonso, S. Santos, and J. Calhau. The clustering of typical Ly α emitters from z $\sim$ 2.5-6: host halo masses depend on Ly α and UV luminosities. , 489(1):555–573, October 2019.

[81] M. Kissler-Patig, J. F. Pirard, M. Casali, A. Moorwood, N. Ageorges, C. Alves de Oliveira, P. Baksai, L. R. Bedin, E. Bendek, P. Biereichel, B. Delabre, R. Dorn, R. Esteves, G. Finger, D. Gojak, G. Huster, Y. Jung, M. Kiekebush, B. Klein, F. Koch, J. L. Lizon, L. Mehrgan, M. Petr-Gotzens, J. Pritchard, F. Selman, and J. Stegmeier. HAWK-I: the high-acuity wide-field K-band imager for the ESO Very Large Telescope. , 491(3):941–950, December 2008.

[82] Jean-Paul Kneib and Priyamvada Natarajan. Cluster lenses. , 19:47, November 2011.

[83] Anton M Koekemoer, S M Faber, Henry C Ferguson, Norman A Grogin, Dale D Kocevski, David C Koo, Kamson Lai, Jennifer M Lotz, Ray A Lucas, Elizabeth J

McGrath, Sara Ogaz, Abhijith Rajan, Adam G Riess, Steve A Rodney, Louis Strolger, Stefano Casertano, Marco Castellano, Tomas Dahlen, Mark Dickinson, Timothy Dolch, Adriano Fontana, Mauro Giavalisco, Andrea Grazian, Yicheng Guo, Nimish P Hathi, Kuang-Han Huang, Arjen van der Wel, Hao-Jing Yan, Viviana Acquaviva, David M Alexander, Omar Almaini, Matthew L N Ashby, Marco Barden, Eric F Bell, Frédéric Bournaud, Thomas M Brown, Karina I Caputi, Paolo Cassata, Peter J Challis, Ranga-Ram Chary, Edmond Cheung, Michele Cirasuolo, Christopher J Conselice, Asantha Roshan Cooray, Darren J Croton, Emanuele Daddi, Romeel Davé, Duilia F De Mello, Loic de Ravel, Avishai Dekel, Jennifer L Donley, James S Dunlop, Aaron A Dutton, David Elbaz, Giovanni G Fazio, Alexei V Filippenko, Steven L Finkelstein, Chris Frazer, Jonathan P Gardner, Peter M Garnavich, Eric Gawiser, Ruth Gruetzbauch, Will G Hartley, Boris Häussler, Jessica Herrington, Philip F Hopkins, Jia-Sheng Huang, Saurabh W Jha, Andrew Johnson, Jeyhan S Kartaltepe, Ali A Khostovan, Robert P Kirshner, Caterina Lani, Kyoung-Soo Lee, Weidong Li, Piero Madau, Patrick J McCarthy, Daniel H McIntosh, Ross J Mclure, Conor Mcpartland, Bahram Mobasher, Heidi Moreira, Alice Mortlock, Leonidas A Moustakas, Mark Mozena, Kirpal Nandra, Jeffrey A Newman, Jennifer L Nielsen, Sami Niemi, Kai G Noeske, Casey J Papovich, Laura Pentericci, Alexandra Pope, Joel R Primack, Swara Ravindranath, Naveen A Reddy, Alvio Renzini, Hans-Walter Rix, Aday R Robaina, David J Rosario, Piero Rosati, Sara Salimbeni, Claudia Scarlata, Brian Siana, Luc Simard, Joseph Smidt, Diana Snyder, Rachel S Somerville, Hyron Spinrad, Amber N Straughn, Olivia Telford, Harry I Teplitz, Jonathan R Trump, Carlos Vargas, Carolin Villforth, Cory R Wagner, Pat Wandro, Risa H Wechsler, Benjamin J Weiner, Tommy Wiklind, Vivienne Wild, Grant Wilson, Stijn Wuyts, and Min S Yun. CANDELS: THE COSMIC ASSEMBLY NEAR-INFRARED DEEP EXTRAGALACTIC LEGACY SURVEY—THE HUBBLE SPACE TELESCOPEOBSERVATIONS, IMAGING DATA PRODUCTS, AND MOSAICS. , 197(2):36, 2011.

[84] Anton M. Koekemoer, S. M. Faber, Henry C. Ferguson, Norman A. Grogin, Dale D. Kocevski, David C. Koo, Kamson Lai, Jennifer M. Lotz, Ray A. Lucas, Elizabeth J. McGrath, Sara Ogaz, Abhijith Rajan, Adam G. Riess, Steve A. Rodney, Louis Strolger, Stefano Casertano, Marco Castellano, Tomas Dahlen, Mark Dickinson, Timothy Dolch, Adriano Fontana, Mauro Giavalisco, Andrea Grazian, Yicheng Guo, Nimish P. Hathi, Kuang-Han Huang, Arjen van der Wel, Hao-Jing Yan, Viviana Acquaviva, David M. Alexander, Omar Almaini, Matthew L. N. Ashby, Marco Barden, Eric F. Bell, Frédéric Bournaud, Thomas M. Brown, Karina I. Caputi, Paolo Cassata, Peter J. Challis, Ranga-Ram Chary, Edmond Cheung, Michele Cirasuolo, Christopher J. Conselice, Asantha Roshan Cooray, Darren J. Croton, Emanuele Daddi, Romeel Davé, Duilia F. de Mello, Loic de Ravel, Avishai Dekel, Jennifer L. Donley, James S. Dunlop, Aaron A. Dutton, David Elbaz, Giovanni G. Fazio, Alexei V. Filippenko, Steven L. Finkelstein, Chris Frazer, Jonathan P. Gardner, Peter M. Garnavich, Eric Gawiser, Ruth Gruetzbauch, Will G. Hartley, Boris Häussler, Jessica Herrington, Philip F. Hopkins, Jia-Sheng Huang, Saurabh W. Jha, Andrew Johnson, Jeyhan S. Kartaltepe, Ali A. Khostovan, Robert P. Kirshner, Caterina Lani, Kyoung-Soo Lee, Weidong Li, Piero Madau, Patrick J. McCarthy, Daniel H. McIntosh, Ross J. McLure, Conor

McPartland, Bahram Mobasher, Heidi Moreira, Alice Mortlock, Leonidas A. Moustakas, Mark Mozena, Kirpal Nandra, Jeffrey A. Newman, Jennifer L. Nielsen, Sami Niemi, Kai G. Noeske, Casey J. Papovich, Laura Pentericci, Alexandra Pope, Joel R. Primack, Swara Ravindranath, Naveen A. Reddy, Alvio Renzini, Hans-Walter Rix, Aday R. Robaina, David J. Rosario, Piero Rosati, Sara Salimbeni, Claudia Scarlata, Brian Siana, Luc Simard, Joseph Smidt, Diana Snyder, Rachel S. Somerville, Hyron Spinrad, Amber N. Straughn, Olivia Telford, Harry I. Teplitz, Jonathan R. Trump, Carlos Vargas, Carolin Villforth, Cory R. Wagner, Pat Wandro, Risa H. Wechsler, Benjamin J. Weiner, Tommy Wiklind, Vivienne Wild, Grant Wilson, Stijn Wuyts, and Min S. Yun. CANDELS: The Cosmic Assembly Near-infrared Deep Extragalactic Legacy Survey—The Hubble Space Telescope Observations, Imaging Data Products, and Mosaics. , 197(2):36, December 2011.

[85] R. G. Kron. Photometry of a complete sample of faint galaxies. , 43:305–325, June 1980.

[86] Konrad Kuijken, Catherine Heymans, Hendrik Hildebrandt, Reiko Nakajima, Thomas Erben, Jelte T. A. de Jong, Massimo Viola, Ami Choi, Henk Hoekstra, Lance Miller, Edo van Uitert, Alexandra Amon, Chris Blake, Margot Brouwer, Axel Buddendiek, Ian Fenech Conti, Martin Eriksen, Aniello Grado, Joachim Harnois-Déraps, Ewout Helmich, Ricardo Herbonnet, Nancy Irisarri, Thomas Kitching, Dominik Klaes, Francesco La Barbera, Nicola Napolitano, Mario Radovich, Peter Schneider, Cristóbal Sifón, Gert Sikkema, Patrick Simon, Alexandru Tudorica, Edwin Valentijn, Gijs Verdoes Kleijn, and Ludovic van Waerbeke. Gravitational lensing analysis of the Kilo-Degree Survey. , 454(4):3500–3532, December 2015.

[87] David J. Lagattuta, Johan Richard, Franz E. Bauer, Benjamin Clément, Guillaume Mahler, Geneviève Soucail, David Carton, Jean-Paul Kneib, Nicolas Laporte, Johany Martinez, Vera Patrício, Anna V. Payne, Roser Pelló, Kasper B. Schmidt, and Geoffroy de la Vieuville. Probing 3D structure with a large MUSE mosaic: extending the mass model of Frontier Field Abell 370. , 485(3):3738–3760, May 2019.

[88] David J. Lagattuta, Johan Richard, Benjamin Clément, Guillaume Mahler, Vera Patrício, Roser Pelló, Geneviève Soucail, Kasper B. Schmidt, Lutz Wisotzki, Johany Martinez, and David Bina. Lens modelling Abell 370: crowning the final frontier field with MUSE. , 469(4):3946–3964, August 2017.

[89] C. Laigle, H. J. McCracken, O. Ilbert, B. C. Hsieh, I. Davidzon, P. Capak, G. Hasinger, J. D. Silverman, C. Pichon, J. Coupon, H. Aussel, D. Le Borgne, K. Caputi, P. Cassata, Y.-Y. Chang, F. Civano, J. Dunlop, J. Fynbo, J. S. Kartaltepe, A. Koekemoer, O. Le Fèvre, E. Le Floc'h, A. Leauthaud, S. Lilly, L. Lin, S. Marchesi, B. Milvang-Jensen, M. Salvato, D. B. Sanders, N. Scoville, V. Smolcic, M. Stockmann, Y. Taniguchi, L. Tasca, S. Toft, M. Vaccari, and J. Zabl. The COSMOS2015 Catalog: Exploring the 1 z 6 Universe with Half a Million Galaxies. , 224:24, June 2016.

[90] C. Laigle, H. J. McCracken, O. Ilbert, B. C. Hsieh, I. Davidzon, P. Capak, G. Hasinger, J. D. Silverman, C. Pichon, J. Coupon, H. Aussel, D. Le Borgne, K. Caputi, P. Cassata, Y. Y. Chang, F. Civano, J. Dunlop, J. Fynbo, J. S. Kartaltepe, A. Koekemoer, O. Le Fèvre, E. Le Floc'h, A. Leauthaud, S. Lilly, L. Lin, S. Marchesi, B. Milvang-Jensen, M. Salvato, D. B. Sanders, N. Scoville, V. Smolcic, M. Stockmann, Y. Taniguchi, L. Tasca, S. Toft, Mattia Vaccari, and J. Zabl. The COSMOS2015 Catalog: Exploring the 1 < z < 6 Universe with Half a Million Galaxies. , 224(2):24, June 2016.

[91] Stephen D. Landy and Alexander S. Szalay. Bias and Variance of Angular Correlation Functions. , 412:64, July 1993.

[92] O. Le Fèvre, G. Vettolani, S. Paltani, L. Tresse, G. Zamorani, V. Le Brun, C. Moreau, D. Bottini, D. Maccagni, J. P. Picat, R. Scaramella, M. Scodeggio, A. Zanichelli, C. Adami, S. Arnouts, S. Bardelli, M. Bolzonella, A. Cappi, S. Charlot, T. Contini, S. Foucaud, P. Franzetti, B. Garilli, I. Gavignaud, L. Guzzo, O. Ilbert, A. Iovino, H. J. McCracken, D. Mancini, B. Marano, C. Marinoni, G. Mathez, A. Mazure, B. Meneux, R. Merighi, R. Pellò, A. Pollo, L. Pozzetti, M. Radovich, E. Zucca, M. Arnaboldi, M. Bondi, A. Bongiorno, G. Busarello, P. Ciliegi, L. Gregorini, Y. Mellier, P. Merluzzi, V. Ripepi, and D. Rizzo. The VIMOS VLT Deep Survey. Public release of 1599 redshifts to $I_{AB} \leq 24$ across the Chandra Deep Field South. , 428:1043–1049, December 2004.

[93] Alexie Leauthaud, Richard Massey, Jean-Paul Kneib, Jason Rhodes, David E Johnston, Peter Capak, Catherine Heymans, Richard S Ellis, Anton M Koekemoer, Oliver Le Fèvre, Yannick Mellier, Alexandre Refregier, Annie C Robin, Nick Scoville, Lidia Tasca, James E Taylor, and Ludovic Van Waerbeke. Weak Gravitational Lensing with COSMOS: Galaxy Selection and Shape Measurements. , 172(1):219–238, 2007.

[94] J. Liesenborgs, S. De Rijcke, and H. Dejonghe. A genetic algorithm for the non-parametric inversion of strong lensing systems. , 367(3):1209–1216, April 2006.

[95] J. M. Lotz, A. Koekemoer, D. Coe, N. Grogin, P. Capak, J. Mack, J. Anderson, R. Avila, E. A. Barker, D. Borncamp, G. Brammer, M. Durbin, H. Gunning, B. Hilbert, H. Jenkner, H. Khandrika, Z. Levay, R. A. Lucas, J. MacKenty, S. Ogaz, B. Porterfield, N. Reid, M. Robberto, P. Royle, L. J. Smith, L. J. Storrie-Lombardi, B. Sunnquist, J. Surace, D. C. Taylor, R. Williams, J. Bullock, M. Dickinson, S. Finkelstein, P. Natarajan, J. Richard, B. Robertson, J. Tumlinson, A. Zitrin, K. Flanagan, K. Sembach, B. T. Soifer, and M. Mountain. The Frontier Fields: Survey Design and Initial Results. *ApJ*, 837:97, March 2017.

[96] P. Madau. Radiative transfer in a clumpy universe: The colors of high-redshift galaxies. , 441:18–27, March 1995.

[97] G. Mahler, J. Richard, B. Clément, D. Lagattuta, K. Schmidt, V. Patrício, G. Soucail, R. Bacon, R. Pello, R. Bouwens, M. Maseda, J. Martinez, M. Carollo, H. Inami, F. Leclercq, and L. Wisotzki. Strong-lensing analysis of A2744 with MUSE and Hubble Frontier Fields images. , 473(1):663–692, January 2018.

[98] Rachel Mandelbaum, Barnaby Rowe, Robert Armstrong, Deborah Bard, Emmanuel Bertin, James Bosch, Dominique Boutigny, Frederic Courbin, William A. Dawson, Annamaria Donnarumma, Ian Fenech Conti, Raphaël Gavazzi, Marc Gentile, Mandeep S. S. Gill, David W. Hogg, Eric M. Huff, M. James Jee, Tomasz Kacprzak, Martin Kilbinger, Thibault Kuntzer, Dustin Lang, Wentao Luo, Marisa C. March, Philip J. Marshall, Joshua E. Meyers, Lance Miller, Hironao Miyatake, Reiko Nakajima, Fred Maurice Ngolé Mboula, Guldariya Nurbaeva, Yuki Okura, Stéphane Paulin-Henriksson, Jason Rhodes, Michael D. Schneider, Huanyuan Shan, Erin S. Sheldon, Melanie Simet, Jean-Luc Starck, Florent Sureau, Malte Tewes, Kristian Zarb Adami, Jun Zhang, and Joe Zuntz. GREAT3 results - I. Systematic errors in shear estimation and the impact of real galaxy morphology. , 450(3):2963–3007, July 2015.

[99] Rachel Mandelbaum, Barnaby Rowe, James Bosch, Chihway Chang, Frederic Courbin, Mandeep Gill, Mike Jarvis, Arun Kannawadi, Tomasz Kacprzak, Claire Lackner, Alexie Leauthaud, Hironao Miyatake, Reiko Nakajima, Jason Rhodes, Melanie Simet, Joe Zuntz, Bob Armstrong, Sarah Bridle, Jean Coupon, Jörg P. Dietrich, Marc Gentile, Catherine Heymans, Alden S. Jurling, Stephen M. Kent, David Kirkby, Daniel Margala, Richard Massey, Peter Melchior, John Peterson, Aaron Roodman, and Tim Schrabback. The Third Gravitational Lensing Accuracy Testing (GREAT3) Challenge Handbook. , 212(1):5, May 2014.

[100] Daniel C. Masters, Daniel K. Stern, Judith G. Cohen, Peter L. Capak, Jason D. Rhodes, Francisco J. Castander, and Stéphane Paltani. The Complete Calibration of the Color-Redshift Relation (C3R2) Survey: Survey Overview and Data Release 1. , 841(2):111, June 2017.

[101] Curtis McCully, Charles R. Keeton, Kenneth C. Wong, and Ann I. Zabludoff. A new hybrid framework to efficiently model lines of sight to gravitational lenses. , 443(4):3631–3642, October 2014.

[102] D. J. McLeod, R. J. McLure, and J. S. Dunlop. The z = 9-10 galaxy population in the Hubble Frontier Fields and CLASH surveys: the z = 9 luminosity function and further evidence for a smooth decline in ultraviolet luminosity density at z$\geq 8., 459 : 3812 - -3824, July 2016$.

[103] Vihang Mehta, Claudia Scarlata, Peter Capak, Iary Davidzon, Andreas Faisst, Bau Ching Hsieh, Olivier Ilbert, Matt Jarvis, Clotilde Laigle, John Phillips, John Silverman, Michael A. Strauss, Masayuki Tanaka, Rebecca Bowler, Jean Coupon, Sébastien Foucaud, Shoubaneh Hemmati, Daniel Masters, Henry Joy McCracken, Bahram Mobasher, Masami Ouchi, Takatoshi Shibuya, and Wei-Hao Wang. SPLASH-SXDF Multi-wavelength Photometric Catalog. , 235(2):36, April 2018.

[104] B. Ménard, T. Hamana, M. Bartelmann, and N. Yoshida. Improving the accuracy of cosmic magnification statistics. , 403:817–828, June 2003.

[105] E. Merlin, R. Amorín, M. Castellano, A. Fontana, F. Buitrago, J. S. Dunlop, D. Elbaz, A. Boucaud, N. Bourne, K. Boutsia, G. Brammer, V. A. Bruce, P. Capak, N. Cappelluti, L. Ciesla, A. Comastri, F. Cullen, S. Derriere, S. M. Faber, H. C. Ferguson, E. Giallongo, A. Grazian, J. Lotz, M. J. Michałowski, D. Paris, L. Pentericci, S. Pilo, P. Santini, C. Schreiber, X. Shu, and T. Wang. The ASTRODEEP Frontier Fields catalogues. I. Multiwavelength photometry of Abell-2744 and MACS-J0416. , 590:A30, May 2016.

[106] E. Merlin, N. Bourne, M. Castellano, H. C. Ferguson, T. Wang, S. Derriere, J. S. Dunlop, D. Elbaz, and A. Fontana. T-PHOT version 2.0: Improved algorithms for background subtraction, local convolution, kernel registration, and new options. , 595:A97, Nov 2016.

[107] J. Merten, M. Cacciato, M. Meneghetti, C. Mignone, and M. Bartelmann. Combining weak and strong cluster lensing: applications to simulations and MS 2137. , 500(2):681–691, June 2009.

[108] J. Merten, D. Coe, R. Dupke, R. Massey, A. Zitrin, E. S. Cypriano, N. Okabe, B. Frye, F. G. Braglia, Y. Jiménez-Teja, N. Benítez, T. Broadhurst, J. Rhodes, M. Meneghetti, L. A. Moustakas, Jr. Sodré, L., J. Krick, and J. N. Bregman. Creation of cosmic structure in the complex galaxy cluster merger Abell 2744. , 417(1):333–347, October 2011.

[109] Jordi Miralda-Escudé. The Dark Age of the Universe. *Science*, 300(5627):1904–1909, June 2003.

[110] H. Miyatake, R. Mandelbaum, and B. Rowe. The GREAT3 challenge. *Journal of Instrumentation*, 9(4):C04031, Apr 2014.

[111] Mireia Montes. The faint light in groups and clusters of galaxies. *Nature Astronomy*, 6:308–316, March 2022.

[112] Mireia Montes and Ignacio Trujillo. Intracluster light: a luminous tracer for dark matter in clusters of galaxies. , 482(2):2838–2851, January 2019.

[113] Takahiro Morishita, Louis E. Abramson, Tommaso Treu, Kasper B. Schmidt, Benedetta Vulcani, and Xin Wang. Characterizing Intracluster Light in the Hubble Frontier Fields. , 846(2):139, Sep 2017.

[114] Matt S. Owers, Scott W. Randall, Paul E. J. Nulsen, Warrick J. Couch, Laurence P. David, and Joshua C. Kempner. The Dissection of Abell 2744: A Rich Cluster Growing Through Major and Minor Mergers. , 728(1):27, February 2011.

[115] A. Pagul, F. J. Sánchez, I. Davidzon, and Bahram Mobasher. Hubble Frontier Field Clusters and Their Parallel Fields: Photometric and Photometric Redshift Catalogs. , 256(2):27, October 2021.

[116] P. J. E. Peebles. Statistical Analysis of Catalogs of Extragalactic Objects. I. Theory. , 185:413–440, October 1973.

[117] P. J. E. Peebles. *The large-scale structure of the universe*. 1980.

[118] C. Y. Peng, L. C. Ho, C. D. Impey, and H.-W. Rix. Detailed Decomposition of Galaxy Images. II. Beyond Axisymmetric Models. , 139:2097–2129, June 2010.

[119] Planck Collaboration, N. Aghanim, Y. Akrami, M. Ashdown, J. Aumont, C. Baccigalupi, M. Ballardini, A. J. Banday, R. B. Barreiro, N. Bartolo, S. Basak, R. Battye, K. Benabed, J. P. Bernard, M. Bersanelli, P. Bielewicz, J. J. Bock, J. R. Bond, J. Borrill, F. R. Bouchet, F. Boulanger, M. Bucher, C. Burigana, R. C. Butler, E. Calabrese, J. F. Cardoso, J. Carron, A. Challinor, H. C. Chiang, J. Chluba, L. P. L. Colombo, C. Combet, D. Contreras, B. P. Crill, F. Cuttaia, P. de Bernardis, G. de Zotti, J. Delabrouille, J. M. Delouis, E. Di Valentino, J. M. Diego, O. Doré, M. Douspis, A. Ducout, X. Dupac, S. Dusini, G. Efstathiou, F. Elsner, T. A. Enßlin, H. K. Eriksen, Y. Fantaye, M. Farhang, J. Fergusson, R. Fernandez-Cobos, F. Finelli, F. Forastieri, M. Frailis, A. A. Fraisse, E. Franceschi, A. Frolov, S. Galeotta, S. Galli, K. Ganga, R. T. Génova-Santos, M. Gerbino, T. Ghosh, J. González-Nuevo, K. M. Górski, S. Gratton, A. Gruppuso, J. E. Gudmundsson, J. Hamann, W. Handley, F. K. Hansen, D. Herranz, S. R. Hildebrandt, E. Hivon, Z. Huang, A. H. Jaffe, W. C. Jones, A. Karakci, E. Keihänen, R. Keskitalo, K. Kiiveri, J. Kim, T. S. Kisner, L. Knox, N. Krachmalnicoff, M. Kunz, H. Kurki-Suonio, G. Lagache, J. M. Lamarre, A. Lasenby, M. Lattanzi, C. R. Lawrence, M. Le Jeune, P. Lemos, J. Lesgourgues, F. Levrier, A. Lewis, M. Liguori, P. B. Lilje, M. Lilley, V. Lindholm, M. López-Caniego, P. M. Lubin, Y. Z. Ma, J. F. Macías-Pérez, G. Maggio, D. Maino, N. Mandolesi, A. Mangilli, A. Marcos-Caballero, M. Maris, P. G. Martin, M. Martinelli, E. Martínez-González, S. Matarrese, N. Mauri, J. D. McEwen, P. R. Meinhold, A. Melchiorri, A. Mennella, M. Migliaccio, M. Millea, S. Mitra, M. A. Miville-Deschênes, D. Molinari, L. Montier, G. Morgante, A. Moss, P. Natoli, H. U. Nørgaard-Nielsen, L. Pagano, D. Paoletti, B. Partridge, G. Patanchon, H. V. Peiris, F. Perrotta, V. Pettorino, F. Piacentini, L. Polastri, G. Polenta, J. L. Puget, J. P. Rachen, M. Reinecke, M. Remazeilles, A. Renzi, G. Rocha, C. Rosset, G. Roudier, J. A. Rubiño-Martín, B. Ruiz-Granados, L. Salvati, M. Sandri, M. Savelainen, D. Scott, E. P. S. Shellard, C. Sirignano, G. Sirri, L. D. Spencer, R. Sunyaev, A. S. Suur-Uski, J. A. Tauber, D. Tavagnacco, M. Tenti, L. Toffolatti, M. Tomasi, T. Trombetti, L. Valenziano, J. Valiviita, B. Van Tent, L. Vibert, P. Vielva, F. Villa, N. Vittorio, B. D. Wandelt, I. K. Wehus, M. White, S. D. M. White, A. Zacchei, and A. Zonca. Planck 2018 results. VI. Cosmological parameters. , 641:A6, September 2020.

[120] M Polletta, M Tajer, L Maraschi, G Trinchieri, C J Lonsdale, L Chiappetti, S Andreon, M Pierre, O Le Fèvre, G Zamorani, D Maccagni, O Garcet, J Surdej, A Franceschini, D Alloin, D L Shupe, J A Surace, F Fang, M Rowan-Robinson, H E Smith, and L Tresse. Spectral Energy Distributions of Hard X-Ray Selected Active Galactic Nuclei in the XMM-Newton Medium Deep Survey. , 663:81, 2007.

[121] Marc Postman, Dan Coe, Narciso Benítez, Larry Bradley, Tom Broadhurst, Megan Donahue, Holland Ford, Or Graur, Genevieve Graves, Stephanie Jouvel, Anton Koekemoer, Doron Lemze, Elinor Medezinski, Alberto Molino, Leonidas Moustakas, Sara

Ogaz, Adam Riess, Steve Rodney, Piero Rosati, Keiichi Umetsu, Wei Zheng, Adi Zitrin, Matthias Bartelmann, Rychard Bouwens, Nicole Czakon, Sunil Golwala, Ole Host, Leopoldo Infante, Saurabh Jha, Yolanda Jimenez-Teja, Daniel Kelson, Ofer Lahav, Ruth Lazkoz, Dani Maoz, Curtis McCully, Peter Melchior, Massimo Meneghetti, Julian Merten, John Moustakas, Mario Nonino, Brandon Patel, Enikö Regös, Jack Sayers, Stella Seitz, and Arjen Van der Wel. The Cluster Lensing and Supernova Survey with Hubble: An Overview. , 199(2):25, April 2012.

[122] M L Prevot, J Lequeux, L Prevot, E Maurice, and B Rocca-Volmerange. The typical interstellar extinction in the Small Magellanic Cloud. *Astronomy and Astrophysics (ISSN 0004-6361)*, 132:389, 1984.

[123] Ryan Quadri, Pieter van Dokkum, Eric Gawiser, Marijn Franx, Danilo Marchesini, Paulina Lira, Gregory Rudnick, David Herrera, Jose Maza, Mariska Kriek, Ivo Labbé, and Harold Francke. Clustering of K-selected Galaxies at 2 ¡ z ¡ 3.5: Evidence for a Color-Density Relation. , 654(1):138–152, January 2007.

[124] Johan Richard, Mathilde Jauzac, Marceau Limousin, Eric Jullo, Benjamin Clément, Harald Ebeling, Jean-Paul Kneib, Hakim Atek, Priya Natarajan, Eiichi Egami, Rachael Livermore, and Richard Bower. Mass and magnification maps for the Hubble Space Telescope Frontier Fields clusters: implications for high-redshift studies. , 444(1):268–289, October 2014.

[125] Hans-Walter Rix, Marco Barden, Steven V. W. Beckwith, Eric F. Bell, Andrea Borch, John A. R. Caldwell, Boris Häussler, Knud Jahnke, Shardha Jogee, Daniel H. McIntosh, Klaus Meisenheimer, Chien Y. Peng, Sebastian F. Sanchez, Rachel S. Somerville, Lutz Wisotzki, and Christian Wolf. GEMS: Galaxy Evolution from Morphologies and SEDs. , 152(2):163–173, June 2004.

[126] B. T. P. Rowe, M. Jarvis, R. Mandelbaum, G. M. Bernstein, J. Bosch, M. Simet, J. E. Meyers, T. Kacprzak, R. Nakajima, J. Zuntz, H. Miyatake, J. P. Dietrich, R. Armstrong, P. Melchior, and M. S. S. Gill. GALSIM: The modular galaxy image simulation toolkit. *Astronomy and Computing*, 10:121–150, Apr 2015.

[127] Shun Saito, Sylvain de la Torre, Olivier Ilbert, Cédric Dubois, Kiyoto Yabe, and Jean Coupon. The synthetic Emission Line COSMOS catalogue: Hα and [O II] galaxy luminosity functions and counts at 0.3 < z < 2.5. , 494(1):199–217, March 2020.

[128] H. Sampaio-Santos, Y. Zhang, R. L. C. Ogando, T. Shin, Jesse B. Golden-Marx, B. Yanny, K. Herner, M. Hilton, A. Choi, M. Gatti, D. Gruen, B. Hoyle, M. M. Rau, J. De Vicente, J. Zuntz, T. M. C. Abbott, M. Aguena, S. Allam, J. Annis, S. Avila, E. Bertin, D. Brooks, D. L. Burke, M. Carrasco Kind, J. Carretero, C. Chang, M. Costanzi, L. N. da Costa, H. T. Diehl, P. Doel, S. Everett, A. E. Evrard, B. Flaugher, P. Fosalba, J. Frieman, J. Garcia-Bellido, E. Gaztanaga, D. W. Gerdes, R. A. Gruendl, J. Gschwend, G. Gutierrez, S. R. Hinton, D. L. Hollowood, K. Honscheid, D. J. James, M. Jarvis, T. Jeltema, K. Kuehn, N. Kuropatkin, O. Lahav, M. A. G. Maia, M. March, J. L. Marshall, R. Miquel, A. Palmese,

F. Paz-Chinchon, A. A. Plazas, E. Sanchez, B. Santiago, V. Scarpine, M. Schubnell, M. Smith, E. Suchyta, G. Tarle, D. L. Tucker, T. N. Varga, and R. H. Wechsler. Is diffuse intracluster light a good tracer of the galaxy cluster matter distribution? *arXiv e-prints*, page arXiv:2005.12275, May 2020.

[129] H. Sampaio-Santos, Y. Zhang, R. L. C. Ogando, T. Shin, Jesse B. Golden-Marx, B. Yanny, K. Herner, M. Hilton, A. Choi, M. Gatti, D. Gruen, B. Hoyle, M. M. Rau, J. De Vicente, J. Zuntz, T. M. C. Abbott, M. Aguena, S. Allam, J. Annis, S. Avila, E. Bertin, D. Brooks, D. L. Burke, M. Carrasco Kind, J. Carretero, C. Chang, M. Costanzi, L. N. da Costa, H. T. Diehl, P. Doel, S. Everett, A. E. Evrard, B. Flaugher, P. Fosalba, J. Frieman, J. García-Bellido, E. Gaztanaga, D. W. Gerdes, R. A. Gruendl, J. Gschwend, G. Gutierrez, S. R. Hinton, D. L. Hollowood, K. Honscheid, D. J. James, M. Jarvis, T. Jeltema, K. Kuehn, N. Kuropatkin, O. Lahav, M. A. G. Maia, M. March, J. L. Marshall, R. Miquel, A. Palmese, F. Paz-Chinchón, A. A. Plazas, E. Sanchez, B. Santiago, V. Scarpine, M. Schubnell, M. Smith, E. Suchyta, G. Tarle, D. L. Tucker, T. N. Varga, and R. H. Wechsler. Is diffuse intracluster light a good tracer of the galaxy cluster matter distribution? , 501(1):1300–1315, February 2021.

[130] Edward F. Schlafly and Douglas P. Finkbeiner. Measuring Reddening with Sloan Digital Sky Survey Stellar Spectra and Recalibrating SFD. , 737(2):103, August 2011.

[131] K. B. Schmidt, T. Treu, G. B. Brammer, M. Bradač, X. Wang, M. Dijkstra, A. Dressler, A. Fontana, R. Gavazzi, A. L. Henry, A. Hoag, T. A. Jones, P. L. Kelly, M. A. Malkan, C. Mason, L. Pentericci, B. Poggianti, M. Stiavelli, M. Trenti, A. von der Linden, and B. Vulcani. Through the Looking GLASS: HST Spectroscopy of Faint Galaxies Lensed by the Frontier Fields Cluster MACSJ0717.5+3745. , 782(2):L36, February 2014.

[132] P. Schneider. The amplification caused by gravitational bending of light. , 140(1):119–124, November 1984.

[133] N Scoville, H Aussel, M Brusa, P Capak, C M Carollo, M Elvis, M Giavalisco, L Guzzo, G Hasinger, C Impey, J-P Kneib, O Lefevre, S J Lilly, B Mobasher, A Renzini, R M Rich, D B Sanders, E Schinnerer, D Schminovich, P Shopbell, Y Taniguchi, and N D Tyson. The Cosmic Evolution Survey (COSMOS): Overview. , 172(1):1–8, 2007.

[134] M. Seldner and P. J. E. Peebles. Statistical analysis of catalogs of extragalactic objects. XI. Evidence of correlation of QSOs and Lick galaxy counts. , 227:30–36, January 1979.

[135] Heath V. Shipley, Daniel Lange-Vagle, Danilo Marchesini, Gabriel B. Brammer, Laura Ferrarese, Mauro Stefanon, Erin Kado-Fong, Katherine E. Whitaker, Pascal A. Oesch, Adina D. Feinstein, Ivo Labbé, Britt Lundgren, Nicholas Martis, Adam Muzzin, Kalina Nedkova, Rosalind Skelton, and Arjen van der Wel. HFF-DeepSpace Photometric Catalogs of the 12 Hubble Frontier Fields, Clusters, and Parallels: Photometry, Photometric Redshifts, and Stellar Masses. , 235(1):14, March 2018.

[136] C. Steinhardt, M. Jauzac, P. Capak, A. Koekemoer, P. Oesch, J. Richard, K. q. Sharon, and BUFFALO. The BUFFALO HST Survey. In *American Astronomical Society Meeting Abstracts #231*, volume 231 of *American Astronomical Society Meeting Abstracts*, page 332.04, January 2018.

[137] Charles L. Steinhardt, Mathilde Jauzac, Ana Acebron, Hakim Atek, Peter Capak, Iary Davidzon, Dominique Eckert, David Harvey, Anton M. Koekemoer, Claudia D. P. Lagos, Guillaume Mahler, Mireia Montes, Anna Niemiec, Mario Nonino, P. A. Oesch, Johan Richard, Steven A. Rodney, Matthieu Schaller, Keren Sharon, Louis-Gregory Strolger, Joseph Allingham, Adam Amara, Yannick Bahé, Céline Bœhm, Sownak Bose, Rychard J. Bouwens, Larry D. Bradley, Gabriel Brammer, Tom Broadhurst, Rodrigo Cañas, Renyue Cen, Benjamin Clément, Douglas Clowe, Dan Coe, Thomas Connor, Behnam Darvish, Jose M. Diego, Harald Ebeling, A. C. Edge, Eiichi Egami, Stefano Ettori, Andreas L. Faisst, Brenda Frye, Lukas J. Furtak, C. Gómez-Guijarro, J. D. Remolina González, Anthony Gonzalez, Or Graur, Daniel Gruen, David Harvey, Hagan Hensley, Beryl Hovis-Afflerbach, Pascale Jablonka, Saurabh W. Jha, Eric Jullo, Jean-Paul Kneib, Vasily Kokorev, David J. Lagattuta, Marceau Limousin, Anja von der Linden, Nora B. Linzer, Adrian Lopez, Georgios E. Magdis, Richard Massey, Daniel C. Masters, Matteo Maturi, Curtis McCully, Sean L. McGee, Massimo Meneghetti, Bahram Mobasher, Leonidas A. Moustakas, Eric J. Murphy, Priyamvada Natarajan, Mark Neyrinck, Kyle O'Connor, Masamune Oguri, Amanda Pagul, Jason Rhodes, R. Michael Rich, Andrew Robertson, Mauro Sereno, Huanyuan Shan, Graham P. Smith, Albert Sneppen, Gordon K. Squires, Sut-Ieng Tam, Céline Tchernin, Sune Toft, Keiichi Umetsu, John R. Weaver, R. J. van Weeren, Liliya L. R. Williams, Tom J. Wilson, Lin Yan, and Adi Zitrin. The BUFFALO HST Survey. , 247(2):64, April 2020.

[138] Charles L. Steinhardt, Mathilde Jauzac, Ana Acebron, Hakim Atek, Peter Capak, Iary Davidzon, Dominique Eckert, David Harvey, Anton M. Koekemoer, Claudia D. P. Lagos, Guillaume Mahler, Mireia Montes, Anna Niemiec, Mario Nonino, P. A. Oesch, Johan Richard, Steven A. Rodney, Matthieu Schaller, Keren Sharon, Louis-Gregory Strolger, Joseph Allingham, Adam Amara, Yannick Bahé, Céline Bœhm, Sownak Bose, Rychard J. Bouwens, Larry D. Bradley, Gabriel Brammer, Tom Broadhurst, Rodrigo Cañas, Renyue Cen, Benjamin Clément, Douglas Clowe, Dan Coe, Thomas Connor, Behnam Darvish, Jose M. Diego, Harald Ebeling, A. C. Edge, Eiichi Egami, Stefano Ettori, Andreas L. Faisst, Brenda Frye, Lukas J. Furtak, C. Gómez-Guijarro, J. D. Remolina González, Anthony Gonzalez, Or Graur, Daniel Gruen, David Harvey, Hagan Hensley, Beryl Hovis-Afflerbach, Pascale Jablonka, Saurabh W. Jha, Eric Jullo, Jean-Paul Kneib, Vasily Kokorev, David J. Lagattuta, Marceau Limousin, Anja von der Linden, Nora B. Linzer, Adrian Lopez, Georgios E. Magdis, Richard Massey, Daniel C. Masters, Matteo Maturi, Curtis McCully, Sean L. McGee, Massimo Meneghetti, Bahram Mobasher, Leonidas A. Moustakas, Eric J. Murphy, Priyamvada Natarajan, Mark Neyrinck, Kyle O'Connor, Masamune Oguri, Amanda Pagul, Jason Rhodes, R. Michael Rich, Andrew Robertson, Mauro Sereno, Huanyuan Shan, Graham P. Smith, Albert Sneppen, Gordon K. Squires, Sut-Ieng Tam, Céline Tchernin,

Sune Toft, Keiichi Umetsu, John R. Weaver, R. J. van Weeren, Liliya L. R. Williams, Tom J. Wilson, Lin Yan, and Adi Zitrin. The BUFFALO HST Survey. , 247(2):64, April 2020.

[139] Austin B. Tomaney and Arlin P. S. Crotts. Expanding the Realm of Microlensing Surveys with Difference Image Photometry. , 112:2872, Dec 1996.

[140] T. Treu, K. B. Schmidt, G. B. Brammer, B. Vulcani, X. Wang, M. Bradač, M. Dijkstra, A. Dressler, A. Fontana, R. Gavazzi, A. L. Henry, A. Hoag, K. H. Huang, T. A. Jones, P. L. Kelly, M. A. Malkan, C. Mason, L. Pentericci, B. Poggianti, M. Stiavelli, M. Trenti, and A. von der Linden. The Grism Lens-Amplified Survey from Space (GLASS). I. Survey Overview and First Data Release. , 812(2):114, October 2015.

[141] T. Wang, C. Schreiber, D. Elbaz, Y. Yoshimura, K. Kohno, X. Shu, Y. Yamaguchi, M. Pannella, M. Franco, J. Huang, C. F. Lim, and W. H. Wang. A dominant population of optically invisible massive galaxies in the early Universe. , 572(7768):211–214, August 2019.

[142] Robert Williams. The Hubble Deep Field. HST Proposal, July 1995.

[143] Y. Zhang, B. Yanny, A. Palmese, D. Gruen, C. To, E. S. Rykoff, Y. Leung, C. Collins, M. Hilton, T. M. C. Abbott, J. Annis, S. Avila, E. Bertin, D. Brooks, D. L. Burke, A. Carnero Rosell, M. Carrasco Kind, J. Carretero, C. E. Cunha, C. B. D'Andrea, L. N. da Costa, J. De Vicente, S. Desai, H. T. Diehl, J. P. Dietrich, P. Doel, A. Drlica-Wagner, T. F. Eifler, A. E. Evrard, B. Flaugher, P. Fosalba, J. Frieman, J. García-Bellido, E. Gaztanaga, D. W. Gerdes, R. A. Gruendl, J. Gschwend, G. Gutierrez, W. G. Hartley, D. L. Hollowood, K. Honscheid, B. Hoyle, D. J. James, T. Jeltema, K. Kuehn, N. Kuropatkin, T. S. Li, M. Lima, M. A. G. Maia, M. March, J. L. Marshall, P. Melchior, F. Menanteau, C. J. Miller, R. Miquel, J. J. Mohr, R. L. C. Ogando, A. A. Plazas, A. K. Romer, E. Sanchez, V. Scarpine, M. Schubnell, S. Serrano, I. Sevilla-Noarbe, M. Smith, M. Soares-Santos, F. Sobreira, E. Suchyta, M. E. C. Swanson, G. Tarle, D. Thomas, W. Wester, and DES Collaboration. Dark Energy Survey Year 1 Results: Detection of Intracluster Light at Redshift ~ 0.25. , 874(2):165, April 2019.